Effect of snow grain shape and impurities on snow albedo and its parameterization: China, North America, and the Arctic

Cheng Dang

A dissertation

submitted in partial fulfillment of the

requirements for the degree of

Doctor of Philosophy

University of Washington

2017

Reading Committee:

Stephen G. Warren, Chair

Qiang Fu, Chair

Sarah J. Doherty

Program Authorized to Offer Degree:

Atmospheric Sciences

University of Washington

Abstract

Effect of snow grain shape and impurities on snow albedo and its parameterization: China, North America, and the Arctic

Cheng Dang

Chair of the Supervisory Committee:

Professor Emeritus Stephen G. Warren,
Department of Atmospheric Sciences

Professor Qiang Fu
Department of Atmospheric Sciences

Snow cover is important for Earth's surface energy budget, primarily because the surface reflectance (albedo) is greatly increased if covered by a layer of snow. A correct estimation of snow albedo is therefore crucial for studying climate and snow hydrology. Snow albedo is influenced by many factors including snow depth, snow grain size, solar zenith angle, cloud cover, and light-absorbing particles (LAPs, black carbon, organic carbon, and mineral dust) in snow, and snow albedo is usually obtained from radiative transfer calculations. Therefore,

an error in those factors and assumptions used in radiative transfer calculations could introduce errors in the computed snow albedo. This dissertation presents three separate works related to snow albedo, aiming towards a better understanding and quantification on the impact of different factors on snow albedo.

First, a new parameterization method for narrowband and broadband albedo of pure snow and snow containing black carbon and mineral dust is introduced. Spectral albedo of snowpacks with different grain radii (5 – 2500 μm), containing a wide range of black carbon or mineral dust amounts (mixing ratio of 0 to 1) were calculated using radiative transfer models (DISORT). For each case, three broadband albedos (visible, near-IR, and all-wave) and twelve narrowband albedos (RRTM bands 2-13) are calculated and parameterized as functions of snow grain radius and LAP concentrations. This method can be incorporated into climate models to calculate snow albedo or study the impact of LAPs on snow albedo.

Second, the effect of snow grain shape on snow albedo is studied. Radiative transfer calculations on snow albedo have usually assumed a spherical shape for snow grains, using Mie theory to calculate the single-scattering properties of ice spheres. The scattering by more realistic non-spherical grains is less in the forward direction and more to the sides. Incident sunlight scattered in the forward direction travels a longer path in the snowpack before reemerging from the snowpacks, and is therefore more likely to be absorbed. For snowpacks with the same area-to-mass ratio, albedo of snowpacks consisting of non-spherical grains is higher than the albedo of snowpacks consisting of spherical grains; the albedo reduction caused by the same amount of black carbon is smaller for snow consisting of non-spherical grains.

Third, the albedo reduction by LAPs in snow over large areas is calculated using field observations and radiative-transfer modeling. Black carbon, mineral dust, and organic carbon may deposit on snowpacks and reduce the very high albedo of snow. As a large fraction of LAPs (especially black carbon) is emitted from anthropogenic sources, the direct albedo reduction induced by LAPs exerts a positive radiative forcing on snow-covered regions. This direct forcing may trigger a series of feedback processes that lead to an amplified radiative forcing, and is therefore crucial for climate and snow hydrology studies. Large-area surveys of LAPs in snow have been carried out by our group and collaborators in the Arctic, China, and North America, and based on these datasets, the albedo reduction caused by black carbon and other LAPs are calculated, and the impact of different factors on derived albedo reductions are also estimated.

TABLE OF CONTENTS

LIST OF FIGURES

LIST OF TABLES

ACKNOWLEDGEMENTS

First, I would like to express my sincere gratitude to Stephen Warren and Qiang Fu. I have been incredibly lucky to have both of them as my Ph.D. advisers. Steve and Qiang have been kind, supportive, thoughtful, and cheerful throughout my graduate studies. They have also shared their wisdom and life experiences with me, which has helped me in forging my own professional and personal path. Being my primary adviser, Steve has generously invested his time to help me become a better scientist and writer. I have acquired precious and fascinating knowledge from him about ice, snow, atmospheric radiation, geology, and geography, which I have applied to my research and beyond. From Steve and Qiang, I have also learned the importance of curiosity and persistence. They are the best advisers I could have asked for in graduate school, and I will always be grateful to them for incorporating me into their research groups and giving me the opportunity to come to UW.

I am also grateful to Sarah Doherty and Thomas Ackerman. Since my first project at UW, Sarah has been a fantastic mentor who has frequently provided insightful suggestions and comments on my research regarding light-absorbing particles in snow. She is thoughtful, adventurous, and an inspiring example of a female scientist. In my second quarter at UW, Tom taught my first course in atmospheric radiation, and I thoroughly enjoyed his lectures. He is also very encouraging and thoughtful, and has gradually become a valued mentor whenever I had questions about science and career choices. I would like to thank Seelye Martin for serving as graduate school representative and for his valuable comments on my dissertation.

Besides my advisers and Ph. D. committee, I am also grateful to Richard Brandt and Tyler Thorsen for teaching me how to use radiative transfer models. I would like to thank Dean Hegg and Thomas Grenfell. Dean guided me through my first project and opened my eyes to the power of chemical analysis. Both Dean and Tom were willing to share their expertise with me, and their research laid the foundation for much of the work in this dissertation. I am grateful to Yun Qian, Chun Zhao and Hailong Wang at PNNL for teaching me how to run the WRF-Chem atmospheric model. I would like to thank Dennis Hartmann for leading me through my first teaching assistant position and for being a fantastic role model. I would also like to thank Jianping Huang and Yuhong Yi for their support and trust since undergraduate school.

I am very grateful to the friendship of many students in the Department of Atmospheric Sciences at UW. In particular, I would like to thank Pu Lin, Maria Zatko, Steve Po-Chedley, Xiaoming Shi, Daniel McCoy, Isabel McCoy, Erika Navarro, Elizabeth Maroon, Jennifer DeHart, Tsubasa Kohyama, Viral Shah, and Chris Terai. I would like to thank Grads 2011 for their companionship since my first day at UW, specifically Xiaojuan Liu, Natalia Hryniw, Crystal McClure, Maximo Menchaca, Pao Baylon, and Karl Lapo. Besides friends in the department, I would also like to thank many other friends in Seattle, particularly Belinda Qian He for her support and friendship.

Most importantly, I would like to thank my mom and dad for their endless love; none of this work would have been done without their unconditional encouragement and support.

DEDICATIONS

To my parents

党晓民 and 张桂萍

Chapter 1

INTRODUCTION

Snow cover is important for the surface energy budget, primarily because the surface reflectance (albedo) is greatly increased if covered by a layer of snow. Fresh non-melting snow can reflect 80-90 percent of sunlight (*Wiscombe and Warren, 1980*). By contrast, soil, forest, or grassland can only reflect 10-30 percent of sunlight; the presence of snow cover therefore increases the surface albedo of these regions by at least 3 fold. As a result, surface albedo in middle and high latitudes shifts rapidly with weather and with the seasonal progression due to the change of snow cover extent. A perturbation to snow extent triggers a positive feedback process called "snow albedo feedback", which is included in all climate models: a reduction of snow-covered area due to warmer air leads to a lower surface albedo, higher solar energy absorbed by the surface, and eventually a warmer atmosphere above the surface. These properties of snow demand accurate simulations of snow cover and snow albedo for climate and snow-hydrology studies. The researches present in this dissertation focus on one of these two aspects - snow albedo.

Pure snow is a mixture of ice and air, the albedo of snow is hence controlled by the optical properties of ice. The absorption coefficient of ice varies with wavelength λ by seven

orders of magnitude; the resulting snow albedo also varies greatly with wavelength (*Wiscombe and Warren, 1980*). For pure fresh snow, the albedo is above 90% in the near-ultraviolet (UV) and visible bands (0.3 - 0.7 μm), then drops rapidly between 0.8 – 1.5 μm and remoains as low as 0-15% from 1.5 to 4 μm. The fundamental property that determines the snow spectral albedo is "specific surface area" – total surface area of snow grains per unit mass of snow. The specific surface area (β) is reciprocally related to a radiative effective grain radius using the following equation:

$$\beta = 3 / (r \rho_{ice})$$

where ρ_{ice} is the density of pure ice, 917 kg m^{-3}. As snow ages, the snow grain size increases and the snow albedo decreases with greatest difference at λ = 1 μm. For example, at λ = 1 μm, the albedo of new snow (r = 100 μm) is larger than the albedo of old-melting snow (r = 1000 μm) by 0.5. What causes such difference is the mean distance that incident photons travel in the snowpack and the amount of ice encountered by the photons before they reemerged from the snowpacks. For a snowpack consisting of coarse grains, light penetrates deeper and encounters more ice, and therefore is more likely to be absorbed. Similarly, for snowpacks with the same grain radius, the spectral albedo of snow increases as the solar zenith angle increases, again because the light penetrates shallower for a larger incident angle. Besides the seasonal and daily variation of solar zenith angle, cloud cover can also alter the solar zenith angle by converting direct light into diffuse light. Depending on the solar zenith angle, the presence of cloud can either increase or decrease the spectral albedo of snowpacks (*Wiscombe and Warren, 1980*). For shallow snow, the snow depth and ground albedo are also important. If the snow is optically thin enough that light can penetrate

through the snowpack, the ground will absorb some of the light and therefore influence the albedo of snow-covered surfaces.

For climate studies, instead of the spectral distribution of snow albedo, the total energy reflected/absorbed by snowpacks is considered of greater importance. This is determined by the broadband albedo of snowpacks. The broadband albedo α of snow is the integrated-average spectral albedo α_λ weighted by solar irradiance S (λ). The band albedo of snow is therefore directly determined by solar spectrum, which varies mainly with solar zenith angle, cloud cover and cloud optical depth (there are also minor effects caused by variations in absorbing gases and particles in the atmosphere). Clouds absorb more light in the near-IR band; solar irradiance reaching the snowpack under a cloudy sky is therefore richer in the visible band, which yields a higher snow albedo.

Besides the above-mentioned factors, more recent studies on snow albedo focus on the impact of light-absorbing particles (LAPs). LAPs are atmospheric particles that absorb sunlight. The major LAPs are black carbon (BC), organic carbon (OC), and mineral dust (MD). These LAPs can be removed from the atmosphere by dry deposition (*Davidson et al., 1985*) and/or during snowfall or rainfall events, i.e. wet deposition (*Baumgardner et al., 2008*). The presence of LAPs in a snowpack can reduce the snow albedo significantly, especially at near-UV and visible wavelengths where ice itself is almost non-absorptive.

Interest in understanding and quantifying the influence of LAPs on snow albedo is partly motivated by the desire for a better snow albedo simulation but more importantly due to the fact that a large fraction of LAPs is emitted from anthropogenic sources. BC ("soot", "elemental carbon") is emitted from incomplete combustion of biofuel and fossil fuel. Primary OC ("brown carbon") is emitted from similar sources, as BC then becomes

secondary OC in the atmosphere; some OC are generated from soil, plants, and other natural non-combustion sources. Most MD originates from deserts, and some from traffic and agriculture. LAPs emitted from human-related activities (e.g. fossil fuel burning or land-use change) can reduce the snow albedo; they are therefore recognized as an important climate forcer. In addition to their different origins, the optical properties of LAPs are also different. BC is the strongest absorber (mass absorption coefficient of 7.5 ± 1.2 m^2/g at λ = 550 nm, *Bond and Bergstrom, 2006*) and its absorption optical depth is almost constant across the visible band (*Bond 2001*). The absorption of OC and MD is wavelength-dependent: stronger in the UV and blue region, then decreases rapidly as wavelength increases towards the red. Their mass absorption coefficients vary depending mostly on the sources but in general are much smaller than the absorption by BC, for example, the mass absorption coefficients for Asian dust and some OC is 0.009 m^2/g and 1 m^2/g respectively at λ = 550 nm (*Bond et al., 2013*). By virtue of its high absorption coefficient, BC dominates the LAP-in-snow absorption globally, and is also recognized the second strongest contributor to the global climate change behind carbon dioxide.

Although the way that LAPs can affect snow albedo is well understood, estimating the concentration of LAPs in snow by numerical models is not an easy task. Compared to field observations, model-simulated BC concentrations are biased low or high by a factor of 10, and few model validations consider MD or OC (*Qian et al., 2015*). Such bias or uncertainty in model-simulated LAPs may yield a large uncertainty in the simulated direct radiative forcing; we therefore aim to constrain them using field observations and radiative transfer calculations.

This dissertation consists three major chapters, with each chapter focusing on a different part related of snow albedo. Each separate chapter is a paper that has been published or is in preparation for publication.

Chapter 2 introduces a new parameterization method for snow albedo, which can be used alone or incorporated into climate models to calculate the albedo of pure snow and snow containing BC or MD. In this work, using radiative transfer models (discrete ordinate method, DISORT), we calculated the spectral albedo of snowpacks for snow grain radii of 5 – 2500 μm, and for snow containing a large range of BC and MD. Band albedo of snow is then calculated for the visible band, near-IR band, and all-wave band. These band albedos and albedo reductions by BC/MD are then parameterized as set of functions of snow grain radius and BC/MD concentrations.

Chapter 3 studies the impact of snow grain shape on snow albedo. As introduced previously, the calculation of snow albedo usually has assumed spherical ice crystals (snow grains), which enables one to calculate their single-scattering optical properties (single-scattering albedo, extinction coefficient, and asymmetry factor) using Mie theory (Wiscombe, 1980). Such assumption may yield an error in the obtained asymmetry factor, and therefore an error in snow albedo. The results and implication for snow albedo calculation are discussed in this chapter.

Chapter 4 presents the snow albedo, albedo reduction by LAPs in snow, and estimated forcing across the large areas in the Northern Hemisphere. This work is motivated by a unique field observation dataset obtained from multiple large-area surveys on LAPs in snow conduced by our group and collaborators in the Arctic, China, and North America. I participated in the North America fieldwork. The results of this work can be used to

constrain model simulations on the LAP-in-snow albedo reduction and also provide insights on future field observations and model validations regarding LAP in snow.

Chapter 2

Parameterizations for Narrowband and Broadband albedo of Pure Snow, and Snow Containing Mineral Dust and Black Carbon

Cheng Dang[1], Richard E. Brandt[2] and Stephen G. Warren[1]

[1]Department of Atmospheric Sciences, University of Washington, Seattle, WA 98195-1640, USA

[2]Atmospheric Sciences Research Center, University at Albany - State University of New York, Whiteface Mountain Field Station, Wilmington, NY 12997, USA

Published in Journal of Geophysical Research: Atmospheres, 2015

doi:10.1002/2014JD022646.

2.0. Abstract.

The reduction of snow spectral albedo by black carbon (BC) and mineral dust, both alone and in combination, is computed using radiative-transfer modeling. Broadband albedo is

shown for mass fractions covering the full range from pure snow to pure BC and pure dust, and for snow grain radii from 5 μm to 2500 μm, to cover the range of possible grain sizes on planetary surfaces. Parameterizations are developed for opaque homogeneous snowpacks for three broad bands used in GCMs, and several narrower bands. They are functions of snow grain radius and the mass fraction of BC and/or dust, and are valid up to BC content of 10 ppm, needed for highly polluted snow. A change of solar zenith angle can be mimicked by changing grain radius. A given mass fraction of BC causes greater albedo reduction in coarse-grained snow; BC and grain radius can be combined into a single variable to compute the reduction of albedo relative to pure snow.

The albedo reduction by BC is less if the snow contains dust, a common situation on mountain glaciers and in agricultural and grazing lands. Measured absorption spectra of mineral dust are critically reviewed as a basis for specifying dust properties for modeling. The effect of dust on snow albedo at visible wavelengths can be represented by an "equivalent BC" amount, scaled down by a factor of about 200. Dust has little effect on the near-IR albedo because the near-IR albedo of pure dust is similar to that of pure snow.

2.1. Introduction

The albedo α of snow varies greatly with wavelength λ (*Wiscombe and Warren*, 1980; *Grenfell et al.*, 1994), because the absorption coefficient of ice varies by seven orders of magnitude across the solar spectrum (*Warren and Brandt*, 2008). The most important snowpack variable influencing the albedo is the ratio of the surface area of snow grains to the mass of snow, the "specific surface area" (e.g. *Matzl and Schneebeli,* 2006, 2010). The specific surface area (β)

can be converted to a radiatively effective snow-grain radius r, the same as the "effective radius" that *Hansen and Travis* (1974) defined for a size distribution of spheres:

$$\beta = 3 / (r \varrho_{ice}), \tag{E2.1}$$

where ρ_{ice} is the density of pure ice, 917 kg m^{-3}. The snow grain size normally increases as the snow ages (*LaChapelle*, 1969). Coarse-grained snow (smaller specific surface area) has lower albedo than fine-grained snow, and the differences are greatest in the near-infrared region around $\lambda \approx 1$ μm, where $\alpha \approx 0.5$ (*Wiscombe and Warren*, 1980).

Integrated over the solar spectrum, the broadband albedo of pure deep snow is in the range 0.7-0.9, higher than that of any other natural surface. This is because at visible wavelengths, where the solar energy spectrum peaks, ice is almost non-absorptive, so incident photons survive refraction through many snow grains to re-emerge at the surface. Because ice absorption is so weak at visible wavelengths, in this spectral region the absorption of sunlight in natural snow is mostly due to absorptive impurities that are incorporated during droplet nucleation in clouds, scavenging by falling snow crystals below the cloud, and dry deposition of aerosol to the snowpack surface. In many geographical regions the most important light-absorbing impurity (LAI) in snow is black carbon (BC); in others brown carbon (organic carbon, OC) or mineral dust may dominate (*Painter et al.*, 2007; *Doherty et al.*, 2010, 2014; *Wang et al.*, 2013).

The importance of BC for snow albedo was noted by *Warren and Wiscombe* (1980, 1985), and a first survey of BC in Arctic snow was carried out by *Clarke and Noone* (1985). Recently, there has been a renaissance of research into radiative forcing by LAI in snow, following the assessment by *Hansen and Nazarenko* (2004) that radiative forcing by anthropogenic BC via reduction of snow albedo has the highest "efficacy" of any forcing

agent, and speculation that it could be responsible for a significant part of Arctic climate change. Related work now includes modeling, field work, and laboratory studies (e.g. *Jacobson*, 2004; *Flanner et al.*, 2007, 2009; *Koch et al.*, 2009; *Doherty et al.*, 2010, 2013, 2014; *Ye et al.*, 2012; *Forsström et al.*, 2009; *Hagler et al.*, 2007; *McConnell et al.*, 2007; *Ming et al.*, 2009; *Brandt et al.*, 2011; *Hadley and Kirchstetter*, 2012; *Hegg et al.*, 2010; *Warren*, 2013). The results of many of these studies were reviewed by *Bond et al.* (2013).

Several climate-modeling efforts are underway to assess the climatic effects of LAI in northern-hemisphere snow. For snow albedo, those models incorporate parameterizations of varying complexity and accuracy, depending on the application, for each of the spectral bands of a general circulation model (GCM). Many GCMs break the solar spectrum into just two bands, 0.2-0.7 μm and 0.7-4.0 μm, and therefore require simple functions to compute band-average albedo. Snow albedo depends on grain size, depth, cloud cover and cloud optical thickness, solar zenith angle, and impurities. If the snowpack is thin, the surface albedo is also affected by the albedo of the underlying surface and by vegetation protruding through the snowpack. In this work we avoid this complexity by developing parameterizations only for snowpacks that are thick enough to hide the underlying surface. Furthermore, we compute broadband albedos for only two atmospheric conditions with their accompanying solar spectra: under clear sky with solar zenith angle $\theta_o = 49.5°$ (with cosine $\mu_o = 0.65$), and under overcast cloud with visible optical depth $\tau = 11$. The angle 49.5° is the effective zenith angle for diffuse radiation under cloud (*Marshall and Warren*, 1987). The value $\mu_o = 0.65$ is also very close to the insolation-weighted average μ for the sunlit hemisphere of Earth, which is a cosine-weighed mean cosine, $\mu = 2/3$, corresponding to $\theta = 48.2°$. This choice will turn out to be useful below where we parameterize the zenith-

angle dependence of snow albedo.

The solar spectra we use are for Arctic summer. The only impurities we consider are BC and mineral dust, each with only one size distribution, but the albedo reduction by organic carbon may be mimicked by mineral dust, because they have similar absorption spectra (stronger absorption at UV and blue wavelengths, weaker absorption at red wavelengths) (*Doherty et al.*, 2010).

Our aim is to produce the simplest possible parameterizations that can represent the most important controlling variables, snow grain size and impurities, with a requirement that they cover the full range of impurity concentrations to be found in snow. Other more complex parameterizations are available, which may be preferable for some purposes. The parameterization of *Marshall and Warren* (1987) and *Marshall* (1989) parameterizes albedo in two bands as functions of snow grain size, solar zenith angle, cloud transmittance, snow depth, underlying surface albedo, and BC content. It was used in a GCM by *Marshall and Oglesby* (1994). *Gardner and Sharp* (2010) developed a parameterization for the total broadband solar albedo, but not for separate visible and near-infrared bands. They reviewed some other parameterizations and showed good agreement of their own work with the parameterization of *Marshall and Warren* (1987). The zenith-angle parameterization developed by *Marshall and Warren* (1987) is incorporated below in our work. Teruo Aoki and his coworkers (*Aoki et al.*, 2011; *Niwano et al.*, 2012; *Yasunari et al.*, 2011, 2014), recognizing the primary influence of snow grain size on albedo, have developed parameterizations of grain growth as a function of snow age and temperature history.

Some GCMs may actually have no need for a snow-albedo parameterization. The SNICAR model of *Flanner et al.* (2007) computes the entire albedo spectrum at fine

wavelength-resolution and then integrates it over whatever band is desired. The SNICAR model has been incorporated as a subroutine in the standard implementation of NCAR's Community Earth System Model (CESM) (*Lawrence et al.,* 2011, 2012*; Holland et al.,* 2012). SNICAR can also be run conveniently from a website, http://snow.engin.umich.edu/.

The parameterization presented here is distinguished from previous work by the following.

(1) We plot albedo for the full range of impurity content, from pure snow to pure dust and pure BC, and develop parameterizations valid up to 10 ppm of BC.

(2) We show how to combine dust and BC as a "BC-equivalent" mass-mixing ratio, for their combined effect on albedo reduction.

(3) We develop parameterizations for multiple spectral bands in GCMs that use more than two bands.

(4) We carry out a review of optical properties of different mineral dusts, with guidance for how to change our parameterization if a different type of dust is desired to replace our choice.

(5) We provide a single metric that quantitatively displays how grain size interacts with impurity content to determine the albedo reduction.

The essence of our work is an update and expansion of Figures 1 and 2 of *Warren and Wiscombe* (1985), which have found use in climate modeling (e.g. *Koch et al.*, 2009).

We consider only particulate impurities; the effects of soluble impurities are probably insignificant by comparison in most locations. As summarized by *Dang and Hegg* (2014): Soluble impurities in snow ('chromophores') were studied by *Beine et al.* (2011) at Barrow, Alaska. The soluble impurities absorb significantly at ultraviolet wavelengths (200-300 nm)

but much less at the longer wavelengths where solar energy peaks. Figure 1 of *Beine et al.* (2011) shows the absorption coefficient (on base-10) versus wavelength for a typical sample of meltwater. The absorption by soluble impurities at 400 nm is equivalent to that of 0.14 ng/g BC; at the mid-visible wavelength 550 nm the absorption is equivalent to 0.07 ng/g BC. The BC mixing ratio at Barrow before onset of melt is 10-30 ng/g (*Doherty et al.*, 2013), similar to the values found elsewhere in North America (*Doherty et al.*, 2014), and particulate non-BC is responsible for comparable absorption. We conclude that absorption by the soluble organics is negligible in comparison.

2.2. Solar spectra used for the spectral integrations

The broadband albedo *a* is an irradiance-weighted average of the spectral albedo α_λ:

$$\alpha = \frac{\int \alpha_\lambda S(\lambda) d\lambda}{\int S(\lambda) d\lambda}, \qquad \text{(E2.2)}$$

where $S(\lambda)$ is the incident solar spectrum and the limits of integration are those of the band under consideration. We use two solar spectra characteristic of high-latitude climate during the sunlit seasons, one clear and one cloudy. They were measured at the surface of the Arctic Ocean during summer by *Grenfell and Perovich* (2008). The measurements covered the wavelength range 0.3-2.5 μm; they are extended to 4.0 μm by use of the atmospheric model SBDART (*Ricchiazzi et al.,* 1998) for the subarctic summer standard atmosphere (*McClatchey et al.*, 1972). The Grenfell-Perovich cloudy case can be matched by specifying a cloud of visible optical depth τ = 11 in SBDART, which is typical for Arctic summer stratus clouds (*Tsay and Jayaweera,* 1984). The principal results of this paper, namely the reduction of

snow albedo caused by BC and dust, turn out to be quite insensitive to the difference between the measured and modeled incident solar spectra. The spectra we use are shown in Figure 2.1.

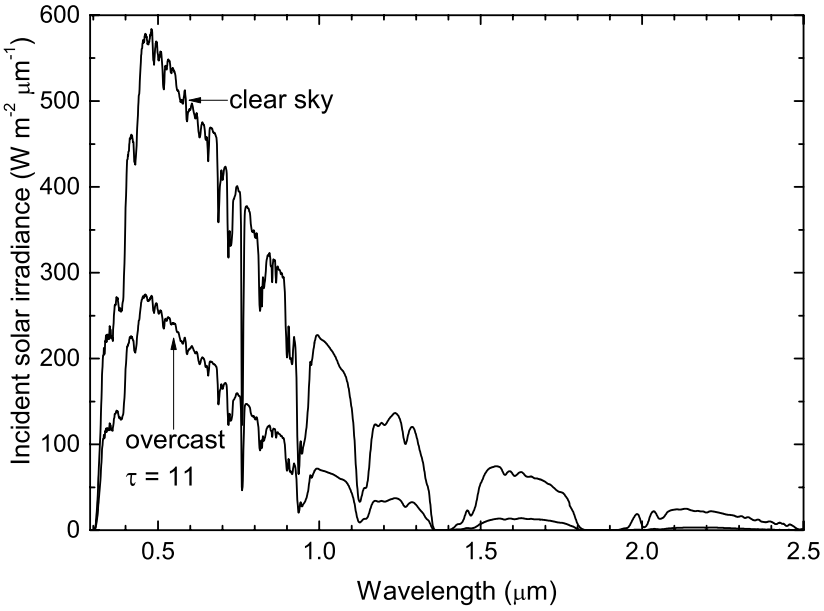

Figure 2.1. Incident solar spectra used for spectral integrations to get broadband albedos (Eq. 2.2). These spectra were measured at the sea surface in the Arctic Ocean during summer under clear sky and under overcast cloud, by Grenfell and Perovich (2008).

2.3. Albedo of pure snow

We use spectral optical constants of ice from the revised compilation of *Warren and Brandt* (2008). We use Mie theory (*Wiscombe*, 1980) to compute extinction efficiency Q_{ext}, single-scattering albedo ϖ, and asymmetry parameter g for ice spheres of radii 5-2500 μm. A nonspherical ice crystal can be represented by a collection of spheres with the same volume-to-area ratio; the accuracy of this representation was evaluated by *Grenfell and Warren* (1999), *Neshyba et al.* (2003), and *Grenfell et al.* (2005), who showed good accuracy for Q_{ext}

and ϖ but discrepancies for g. A size distribution of snow grains is represented by the area-weighted mean radius, called the "effective radius". Scattering and absorption calculated using effective radii have been shown to accurately reproduce scattering and absorption calculated with full particle size distributions (*Hansen and Travis,* 1974). The range of sizes considered here spans the effective radii of surface snow on Earth, which are rarely smaller than 30 μm or larger than 1000 μm (*LaChapelle*, 1969), and allows for application to other planetary surfaces that may have smaller or larger grains. The plots of single-scattering quantities Q_{ext}, 1 - ϖ, and g are similar to those published by *Wiscombe and Warren* (1980); they are shown in the supplementary materials (Appendix A-2).

The spectral albedo of pure deep snow is then computed using the discrete ordinates method (DISORT; *Stamnes et al.* (1988)), and is shown in several of the figures below as the reference plot from which reductions due to LAI are determined. The results for pure snow deviate slightly from those of *Wiscombe and Warren* (1980), but the deviations are mainly due to the use of the new compilation of ice absorption coefficient (*Warren and Brandt*, 2008); the use of DISORT rather than the delta-Eddington method for the radiative transfer had little effect.

Band albedos are shown in Figure 2.2. They are parameterized as quadratic functions of snow grain radius:

$$\alpha(r) = b_0 + b_1 r_n + b_2 r_n^2 , \qquad \text{(E2.3)}$$

where

$$r_n \equiv \log_{10}(r / r_0), \qquad \text{(E2.4)}$$

representing the relative deviation from a reference baseline grain radius r_0 = 100 μm. The coefficients are given in Table 2.1.

The albedos are slightly higher than in our earlier work, because the absorption

coefficient of ice in the wavelength-region 300-600 nm is smaller in the revised compilation (*Warren and Brandt*, 2008) than in the compilation used earlier (*Warren*, 1984).

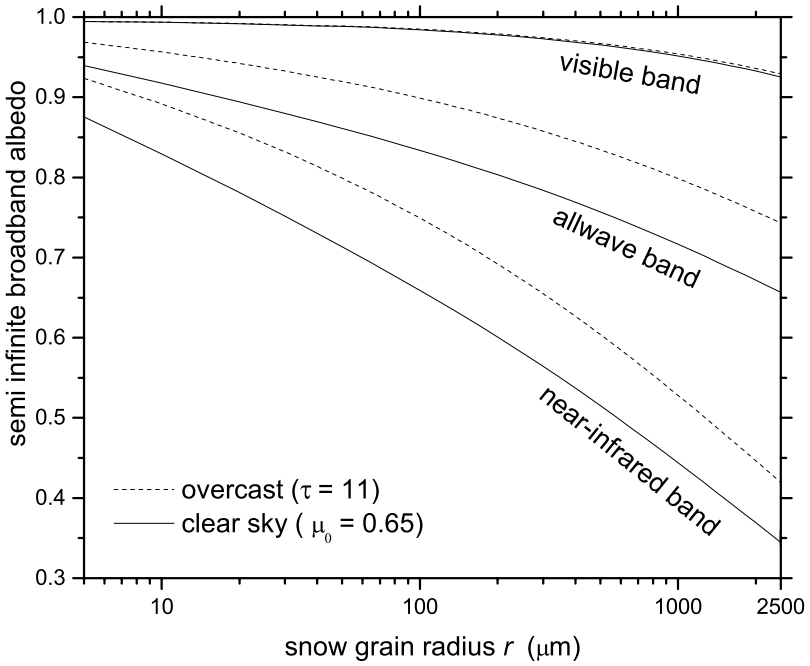

Figure 2.2. Broadband albedo of pure deep snow as a function of optically-effective snow grain radius, for three bands: visible (0.3-0.7 μm), NIR (0.7-4.0 μm), and allwave (0.3-4.0 μm), each for both clear sky and overcast sky.

2.3.1. Effect of zenith angle

Marshall and Warren (1987) and *Marshall* (1989) showed that the spectral signature of changing solar zenith angle resembles that of changing snow grain size, so that the two variables can be combined into a single predictor for snow albedo. *Marshall* (1989) did this by defining a standard zenith cosine, $\mu_D = 0.65$ (zenith angle θ=49.5°), which is the effective zenith angle for diffuse radiation (meaning that snow albedo for diffuse incidence is the same as the albedo for a direct beam at μ=0.65). For a direct beam at angle μ incident on a snowpack with grain radius r, the snow albedo is the same as that for Sun at μ_D and an

altered grain radius r' (Eq. 2.4 of *Marshall* (1989)):

$$r' = r(1 + a\,\Delta\mu)^2, \qquad \text{(E2.5)}$$

where $\Delta\mu \equiv \mu - \mu_D$; values of a are 0.781 (visible), 0.791 (near-IR), and 0.786 (allwave). The reference value $\mu_D = 0.65$ is also close to the insolation-weighted solar zenith cosine for the sunlit hemisphere of a planet, $\mu = 2/3$. All our plots for clear-sky albedo are for $\mu = \mu_D = 0.65$; values for other zenith angles under clear sky can be obtained by altering the snow grain radius using Eq. 2.5.

2.4. Single-scattering by black-carbon particles

The spectral scattering and absorption properties of BC particles ("intrinsic optical properties", IOPs) depend on the density of the BC composing a particle, the complex refractive index, and the size distribution (*Bond and Bergstrom*, 2006). When BC particles are embedded in a snowpack, their IOPs additionally depend on their microlocation, whether inside snow grains ("internally mixed"), or in interstitial spaces between snow grains ("externally mixed"), or on the surfaces of snow grains (*Ackerman and Toon*, 1981; *Fuller et al.*, 1999; *Flanner et al.*, 2012). Our modeling uses Mie theory assuming external mixtures; an internal mixture has greater absorption, by a factor of 1.8-2.1 (*Flanner et al.,* 2012); this scale factor can be applied to our results if an internal mixture is to be modeled. Figure 2.3 shows computed IOPs for four different size distributions of BC, described by their mass-mean diameters (D_{mm}) and effective radii (r_{eff}). All size distributions in these calculations are lognormal, with geometric width $\gamma_g = 1.3$ (*Clarke et al.,* 1987).

For our computations with BC we use complex refractive index $m = 1.95\text{-}0.79i$,

independent of wavelength, and density ρ = 1.8 g cm^{-3}, as recommended by *Bond and Bergstrom* (2006). They reviewed measurements of $m(\lambda)$ and concluded that, within experimental error, there was no evidence for a wavelength-dependence of m (*Bond and Bergstrom,* 2006, Section 7.6). The extinction efficiency Q_{ext} (Figure 2.3a) decreases with wavelength; for $\lambda \gg D_{mm}$ the particles are in the Rayleigh limit and Q_{ext} is proportional to λ^{-4}. The single-scattering albedo ϖ (Figure 2.3b) also decreases with λ as the BC particles become pure absorbers in the Rayleigh limit. The asymmetry parameter g (Figure 2.3c) also decreases with wavelength, as the Rayleigh-scattering phase function is forward-backward symmetric. The quantities Q_{ext} and ϖ, in combination with r_{eff} and the particle density ρ, determine the mass-absorption cross-section (sometimes called "mass absorption efficiency") B_a, with units m^2/g, shown in Figures 3d and 3e:

$$B_a = \frac{Q_{ext}\pi r_{eff}^{\ 2}(1-\varpi)}{\frac{4}{3}\pi r_{eff}^{\ 3}\rho} = \frac{3Q_{ext}(1-\varpi)}{4r_{eff}\rho}. \qquad \text{(E6)}$$

A size distribution with D_{mm} = 0.13 mm was chosen to represent ambient atmospheric soot (*Clarke et al.*, 1987); all subsequent results in this paper use this distribution. Together with our choices for ρ and m, this size distribution has B_a = 6.73 m^2/g at λ = 550 nm, which is toward the low end of the range recommended by *Bond and Bergstrom* (2006) for atmospheric BC, B_a = 7.5±1.2 m^2/g. As Figure 2.3d shows, B_a at 550 nm (as a function of D_{mm}) peaks at $D_{mm} \approx$ 130 nm, so higher values of B_a can be obtained only by altering ρ or m away from the ranges recommended by Bond and Bergstrom. *Flanner et al.* (2009) did adjust the BC density to obtain B_a = 7.5 m^2/g at λ = 550 nm, but we have not done so. We think that the lower value we obtain for B_a is probably more appropriate for BC in snow because BC particles aggregate in snow to larger sizes (*Schwartz et al.,* 2013), which would have smaller B_a (Figure

2.3d).

Figure 2.3e shows that B_a for BC decreases with wavelength, paralleling the decrease of Q_{ext} in the Rayleigh regime. The B_a for dust parallels that for BC, but dust particles are larger and not in the Rayleigh limit, so the spectral behavior for dust has a different explanation, namely that the absorption coefficient of pure dust decreases with wavelength, as will be shown below in Section 2.6.

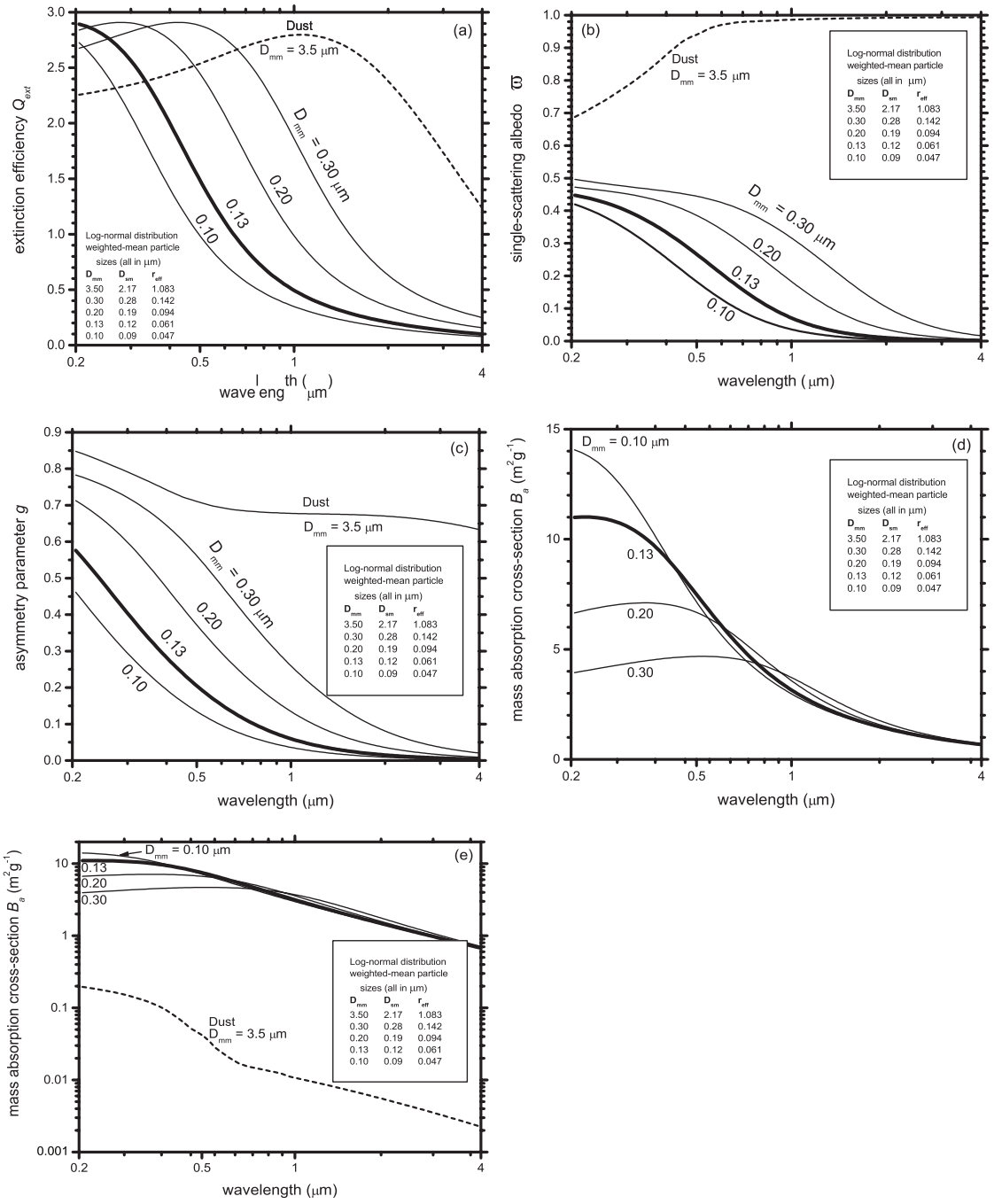

Figure 2.3. Single-scattering quantities for BC and mineral dust: (a) Extinction efficiency Q_{ext}; (b) single-scattering albedo ϖ; (c) asymmetry parameter g; (d) mass-absorption cross-section B_a; (e) mass-absorption cross-section B_a on a logarithmic scale so as to display both dust and BC together. Results are plotted for four different size distributions of BC, labeled by their mass-mean diameters (D_{mm}). The corresponding surface-mean diameters D_{sm} and effective radii (r_{eff}) are given in the legend. The plots for D_{mm} = 0.13 mm are shown in bold; they are used in the multiple-scattering calculations for mixtures of BC and snow.

2.5. Albedo of snow containing black carbon

The single-scattering quantities, computed separately for ice particles and black-carbon particles (both represented by spheres), must be combined according to their specified mass fractions. The procedure for doing this is given in the Appendix A-1.

2.5.1. Spectral albedo

Figure 2.4 shows the albedo for pure snow and for snow with added BC in three mixing ratios. For $\lambda < 1$ μm, BC causes a reduction of albedo; at longer wavelengths ice itself is strongly absorptive, so small amounts of absorptive impurities have little effect. For a given BC mixing ratio, the reduction of albedo is greater in coarse-grained snow (Figure 2.4b) than in fine-grained snow (Figure 2.4a), as was first shown by *Warren and Wiscombe* (1980). For small BC mixing ratios, albedo is nearly flat across the visible and near-ultraviolet (near-UV). For very large BC mixing ratios

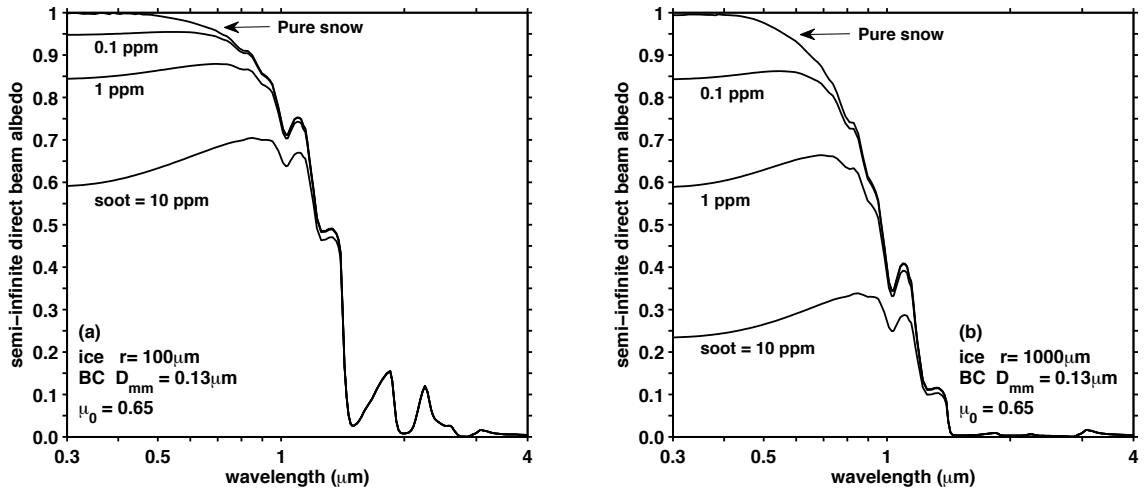

Figure 2.4. Spectral albedo (for a direct solar beam) of pure snow, and of snow containing BC in three mixing ratios. (a) Snow grain radius r = 100 μm. (b) r = 1000 μm.

the albedo shows a reddening because of the greater absorption by BC at shorter wavelengths (Figure 2.3d). Figure 2.4 resembles Figure 7 of *Warren and Wiscombe* (1980); the differences are due to the use of new optical constants for ice and different physical and optical properties of BC.

2.5.2. Broadband albedo

The reduction of broadband snow albedo caused by BC is plotted in Figure 2.5 for three wavelength-bands, using the clear-sky solar spectrum. These values, as well as those for snow under cloud, are fitted to cubic or quadratic functions of the BC mixing ratio C relative to a reference value $C_o=10^{-6}$; the coefficients in turn are quadratic functions of snow grain radius.

In choosing a parameterization for albedo reduction $\Delta\alpha$, we are guided by measurements showing the range of BC mixing ratios to be expected, usually expressed as ng/g, equivalent to ppb by mass. Typical BC mixing ratios are 0.1-0.7 ng/g on Antarctica (*Warren and Clarke*, 1990), 2-4 ng/g on the Greenland Ice Sheet, 10-30 ng/g in low-elevation Arctic regions (*Doherty et al.*, 2010), and 20-100 ng/g in midlatitude North America (*Doherty et al.*, 2014). However, mixing ratios as high as 2000 ng/g are found in northeast China (*Huang et al.*, 2011; *Wang et al.,* 2013), so we offer parameterizations valid up to 10,000 ng/g (10 ppm). To maintain accuracy without the need for higher-order terms, we have developed separate parameterizations for high and low BC mixing ratios ("Range 1", 100 ppb – 10 ppm; and "Range 2", <300 ppb). The two parameterizations overlap in the range 100-300 ppb, where both are accurate.

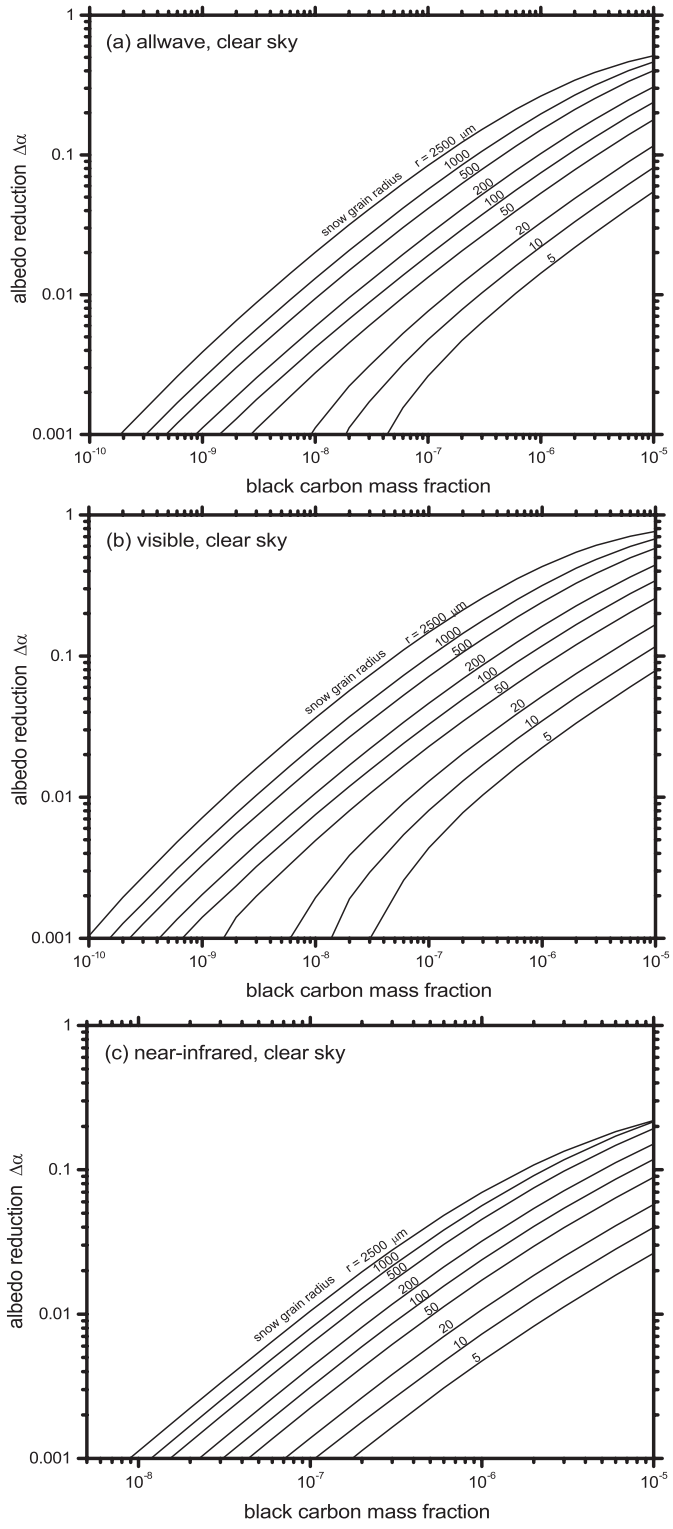

Figure 2.5. Reduction in clear-sky broadband albedo ($\Delta\alpha$) caused by the addition of BC to snow, as a function of the mass fraction of BC, for eight different snow grain radii from 5 μm to 2500 μm. (a) Allwave; (b) visible band; (c) near-infrared band.

The coefficients for the parameterizations are given in Table 2.2. The parameterizations are functions of *log C*, so they cannot be used directly as *C* approaches zero. Therefore, for each spectral interval we determine, as a function of snow grain size, the minimum value of *C* for which the Range-2 parameterization is applicable, then linearly interpolate $\Delta\alpha$ down to $\Delta\alpha$ =0 at *C*=0 ("Range 3" in Table 2.2).

The errors caused by use of the parameterization are plotted in the supplementary material (Appendix A-2). The maximum absolute error is <0.001 for most combinations of *r* and *C*; it slightly exceeds 0.005 for the combination of large *r* and large *C* (*r* > 1000 μm and *C* > 1000 ng/g).

2.5.3. Combination of snow grain size and BC content into a single predictor

A given BC mixing ratio causes a greater albedo reduction in coarse-grained snow than in fine-grained snow. The albedo reduction $\Delta\alpha$ caused by a given BC mixing ratio *C* in snow of grain size *r* could alternatively be caused by a smaller *C* if the snow grain size is larger. In fact, the curves in Figure 2.5 parallel each other, suggesting that snow grain size and BC mixing ratio might be combined into a single predictor for the BC-induced albedo reduction, for quick hand-calculations. (Note that here we are predicting not the albedo but rather the BC-induced albedo reduction.) Indeed, this can be done, with only slight loss of accuracy. To do so, we define a single parameter *H*, which accounts for changes in both BC mixing ratio and snow grain size:

$$H \equiv \left(\frac{C}{C_0}\right)\left(\frac{r}{r_0}\right)^s . \qquad \text{(E2.7)}$$

We vary *s* until the curves in Figure 2.5 merge to a single curve, obtaining *s*=0.73 for

allwave and visible, and s=0.43 for near-IR (Figure 2.6). This means that for allwave albedo or visible albedo, a twofold increase of C causes the same change in BC-induced albedo reduction as multiplying r by 2.6. The near-IR albedo is less sensitive to C; for the near-IR a twofold increase in C can be mimicked by a fivefold increase in r.

Plots of albedo reduction versus H (Figure 2.6) for the allwave, visible, and near-IR bands are fitted to quadratic functions of H:

$$\Delta\alpha_n \equiv \log_{10}(\Delta\alpha) = m_1H^2 + m_2H + m_3, \qquad \text{(E2.8)}$$

whose coefficients are given in Table 2.3. This parameterization is valid for $50 < r < 2500$ μm and for ranges of H that are different for the different wavelength-bands, as given in Table 2.3. The use of Equation 2.8 instead of the full parameterization causes only small errors. For $C \leq 10^{-6}$ g/g, the allwave and near-IR albedo errors are < 0.01; the visible errors are < 0.015.

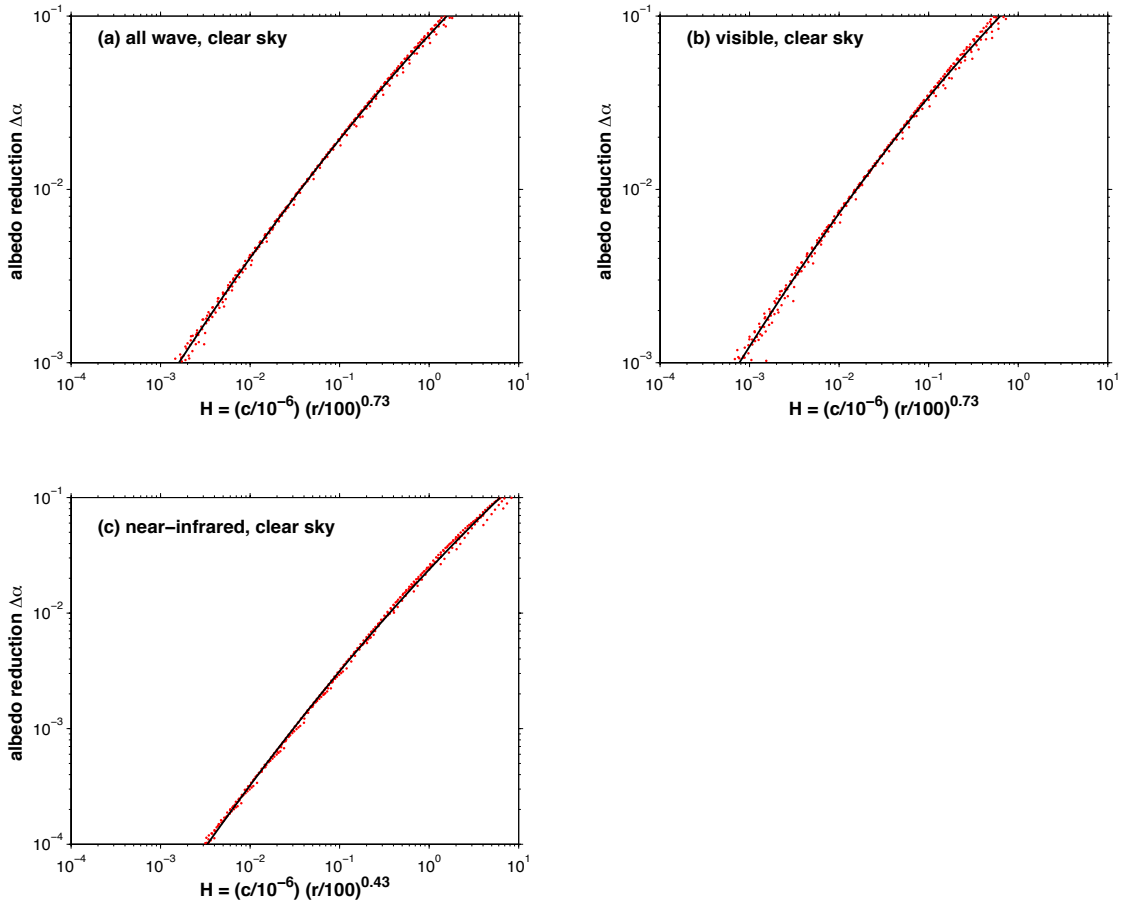

Figure 2.6. Combination of snow grain radius and BC content into a single predictor H for BC-induced albedo-reduction (Eq. 2.7). The points are DISORT results for snow grain sizes $r \geq 50$ μm; the curve is a quadratic fit to the points (Table 2.3).

2.5.4. Parameterizations for narrow bands (RRTM)

Some GCMs subdivide the solar spectrum into several narrower bands. A popular choice is the set of 14 bands used in the Rapid Radiative Transfer Model (RRTM) (*Mlawer and Clough*, 1997). These bands are listed in Table 2.4. We do not consider Band 1 (UV) because no solar energy reaches the surface in this band. We also do not consider Band 14 because the albedo of pure snow in that band is so small that adding BC to snow does not significantly affect the albedo. For Bands 7-13 the effect of r on $\Delta\alpha$ is not monotonic

because for coarse-grained snow the albedo at these wavelengths is so low that it cannot be reduced much by BC; $\Delta\alpha$ therefore maximizes at an intermediate value of $r \approx 100$ μm and cannot be represented by the simple functions used in the parameterizations of Table 2.2. However, $\Delta\alpha$ is very small in these bands for values of C typically found in snow. Furthermore, Bands 7-13 are of minor importance for the surface energy budget; the fraction of incident solar flux at $\lambda > 1.24\ \Delta\alpha$ is only 12% for our clear-sky spectrum and 6% for our cloudy-sky spectrum. We therefore have not parameterized $\Delta\alpha$ for Bands 7-13. For Bands 2-6 we have developed parameterizations similar to those of Table 2.2; their coefficients are given in the supplementary material (Appendix A-2).

2.6. Dust characteristics for modeling

Windblown mineral dust varies in composition depending on the source region. Several reports of its spectral absorption coefficient have been published for the spectral regions where snow albedo is sensitive to impurities (UV and visible). We will review these below, along with other relevant physical and optical properties of dust. Most of the optical properties were measured for Saharan dust, and the values we will choose for our modeling are a modification of one of the Saharan measurements, so we discuss the Saharan measurements in some detail.

2.6.1. Sources of dust

The largest dust source for the global atmosphere is Africa north of the equator, releasing ~800 Mt/year (*Formenti et al.*, 2011). The second-largest source is China-Mongolia (100-460 Mt/yr). Many of the measured properties of dust have come from

studies of North African dust at various distances from the source, with some measurements made downwind across the Atlantic. We discuss these measurements below, and consider whether they are appropriate for modeling dust in snow. *Formenti et al.* (2011) pointed out that dust from the Sahel (10°-20°N, e.g. Niger, Burkina Faso, Mauritania) is redder and more absorptive than dust from the Sahara (20°-30°N), citing *Lazaro et al*. (2008). *McConnell et al*. (2010) say: "The content and speciation of iron oxides vary with source, with Sahelian sources being generally richer in absorbing iron oxides than the Saharan ones", citing *Formenti et al*. (2008) and *Claquin et al*. (1999). Winter is the dry season in the Sahel, so the Sahel is a source of dust for the Atlantic only in winter. In summer the Sahel is wet, so summer dust measured in the Atlantic comes only from the Sahara. Regional differences within Africa therefore result in seasonal differences in absorption and redness of aerosol transported out over the Atlantic.

2.6.2. Dust density

Reported densities for mineral dust are consistent with those of typical crustal minerals. Measured densities for atmospheric dust particles from the Sahara (in kg m^{-3}) are 2500 (*Linke et al.*, 2006) or 2450-2700 (*Haywood et al.*, 2001). Values of 2500 were used by *Zender et al.* (2003) and 2650 by *Haywood et al.* (2003). A smaller value of 2000 was retrieved from mass closure by *Maring et al.* (2003). We adopt 2500 kg m^{-3} for our modeling.

2.6.3. Dust size distribution

Measured size distributions of dust aerosol are commonly fitted to the sum of two or three lognormal modes, as was done for example by *Clarke et al.* (2004) for East Asian dust.

We use a single lognormal size distribution for mineral dust, with geometric mean diameter D_g = 0.65 mm and geometric standard deviation γ_g = 2 (see definitions in *Reist* (1993)). This distribution has mode diameter 0.4 mm and mass-mean diameter D_{mm} = 3.5 mm. This distribution is meant to represent a combination of Modes 1 and 2 of the three-mode description for East Asian dust (Figure 5c of *Clarke et al.* (2004)). Our D_{mm} of 3.5 mm is also in the middle of the range shown for dust undergoing long-range transport in a review of Saharan dust ("Coarse Mode 1" in Figure 4 of *Formenti et al.* (2011)). The coarsest dust is found near sources (*Kok*, 2011; Table 6.8 of *Goudie and Middleton*, 2006). *Maring et al.* (2003) showed how the size distribution evolves with time, for Saharan dust sampled first near the Sahara in the Canary Islands and then later after traveling across the Atlantic to Puerto Rico. Our D_{mm} of 3.5 corresponds to a transport time of 4 days in Figure 5 of *Maring et al.* (2003); after 10 days D_{mm} drops to 3.3. Since our principal results are for broadband albedos, we think a single dust mode is adequate for modeling of snow albedo. The distribution we have chosen (D_g = 0.65; γ_g = 2) has D_{mm} = 3.5, in line with observations of dust undergoing long-range transport, and it is consistent with other recent modeling efforts.

2.6.4. Complex refractive index of dust

There is little disagreement about the real index m_{re}; it is 1.50-1.55 with only slight wavelength dependence (e.g. Figure 4b of *Balkanski et al*. (2007)). The wavelength-dependence of the imaginary index m_{im}, or alternatively the absorption coefficient k_{abs}, is more variable for different dust types. It has been inferred using a range of methods, with the resulting spectral indices shown in Figure 2.7. It varies with the type of dust, in particular with the content of the strongly-absorbing iron oxides hematite and goethite. In our past work on dust in snow (*Warren and Wiscombe*, 1980) we used the spectral imaginary

index reported for Saharan dust by *Patterson, Gillette, and Stockton* (1977; hereinafter PGS), which Warren and Wiscombe called "red dust". The PGS imaginary index is also in use by NCAR's Community Atmosphere Model (CAM4). However, there is recent evidence that much of the atmospheric mineral dust is less absorptive, and perhaps also less red, than PGS reported. The single-scattering albedo of PGS dust at wavelength 550 nm is $\varpi \approx 0.85$, whereas most atmospheric aerosol apparently has $\varpi \approx 0.96$ or even higher at 550 nm. In the ACE-Asia project, *Doherty et al.* (2005, Table 10) found $\varpi = 0.96$ for the size mode $D > 1$ μm at λ=550 nm. *Lafon et al.* (2006) found that Aeronet retrievals imply mid-visible $\varpi \geq 0.95$. In Morocco, *Kandler et al.* (2009) found $\varpi \approx 0.95$ at λ=550 nm. *McConnell et al.* (2010) found values 0.97-0.98 over Mauritania. In Niger, *Osborne et al.* (2008) obtained $\varpi = 0.99$. For Saharan dust, *Haywood et al.* (2003) obtained ϖ between 0.95 and 0.99.

The spectral dependence of absorption can be described by the absorption Ångström exponent $\mathring{A}_{abs}$ such that the mass-absorption cross-section B_a is proportional to $\lambda^{-\mathring{A}abs}$ (e.g. Eq. 8 of *Grenfell et al*. (2011)). The PGS dust has $\mathring{A}_{abs}$ =3.6 for 450-600 nm. The review of *Sokolik et al.* (1993, Figure 1) showed PGS dust to have the steepest wavelength dependence of the reports they cited. Some recent reported values of $\mathring{A}$ are lower, but some are similar to PGS: $\mathring{A}_{abs}$ = 2.34 over the Atlantic (*Reid et al.*, 2003), 2.83 in Tunisia (*Alfaro et al.*, 2004), a median of 3.2 for pure dust in the Moroccan Sahara over the wavelength range 467-660 nm (*Petzold et al.*, 2009), and 2.2-4.5 for Saharan dust (*Müller et al.*, 2011). In our snow-sampling expeditions we have collected samples of the soil below the snow, because it can be a major source for LAI in the snow. Median values of Ångström exponents for soil were 3.66 in China (*Huang et al.,* 2011; *Wang et al.*, 2013) and 3.5-4.7 in Western North America (*Doherty*

et al., 2014). Soil, of course, contains organic material as well as mineral dust. Volcanic ash from the Antarctic Ice Sheet had $\mathring{A}_{abs}$ = 3.13 (*Dadic et al.,* 2013).

Most, but not all, of the recent measurements of m_{im} fall below that of PGS and show weaker wavelength dependence. Three studies that do agree with PGS are *Müller et al.* (2009), *Müller et al.* (2011), and *Wagner et al*. (2012, Figures 10 and 11). The Wagner study was performed on dust generated in the laboratory by dispersing soil samples, including red soil from Burkina Faso.

A number of recent studies have adopted values reported by *Balkanski et al.* (2007), so we explain here in some detail why we think they are not appropriate for our modeling. Some recent uses of those values were to explore the impact of different hematite/goethite mixes on optical properties (*Meland et al.*, 2011), to explain the impact of the optical properties of dust on aerosol retrievals (*Solmon et al.*, 2008), and to show consistency with other model simulations (e.g. *Zhao et al*. (2011)). Balkanski et al. used laboratory-measured absorption spectra of pure minerals and combined them in different ways (using mixing rules) to determine which combination best matched measurements from the Aerosol Robotic Network (AERONET) "over all sites where mineral dust is the dominant aerosol component". Other likely constituents of the aerosol include BC, which could explain their low value of $\mathring{A}_{abs}$, since $\mathring{A}_{abs}$ of BC is ~1.0 (Figure 2.3e). Balkanski et al. used hematite to represent the sum of hematite and goethite; the hump in m_{im} at 450 nm shown in Figure 2.7 is apparently the result of this choice: hematite has such a hump but goethite does not (Figure 5 of *Sherman and Waite* (1985)). Balkanski et al. obtained the best agreement with AERONET measurements when 1.5% hematite was internally mixed with other (mainly non-absorbing) minerals (their Figure 4). They limited their comparison to the summer

season (i.e. to the Sahara, see above) when ϖ = 0.95. They excluded the winter season because then ϖ = 0.86, because they thought this meant there was a significant amount of BC in the aerosol. However, PGS dust has ϖ = 0.86 in mid-visible, so an alternative explanation for the low winter ϖ would be that the source in winter is mostly Sahel, which has more-absorptive dust. In any case, by using only summertime data Balkanski et al. have excluded the half of the year when the Sahel dominates the north-African dust.

Figure 2.7 contains the three curves from Figure 4 of *Balkanski et al.* (2007), for hematite contents 0.9, 1.5, and 2.7%. These spectra have some peculiar characteristics:

(1) They are flat from 300 to 400 nm, then exhibit a hump between 400 and 500 nm.

(2) Their absorption Ångström exponent from 400 to 600 nm is 1.0, the same as BC.

(3) The three curves parallel each other, indicating that the hematite content has no influence on $\mathring{A}_{abs}$. Aerosols with greater hematite content should be redder; i.e., have larger $\mathring{A}_{abs}$, as was the case for dust with 1% and 10% hematite given by *Sokolik and Toon* (1999) (Figure 2.7).

The rationale for our choice of dust imaginary index $m_{im}(\lambda)$ is as follows. To obtain an Ångström exponent corresponding to most desert-dust samples, and also to obtain ϖ =0.96 at λ=550 nm to agree with the consensus of aircraft measurements of dust aerosol (e.g. *Doherty et al.* (2005)), we have taken the lowest curve of *Wagner et al.* (2012) and scaled it down at all wavelengths by a single factor to obtain ϖ=0.96 at λ =550nm. This $m_{im}(\lambda)$, together with our dust size distribution, gives $B_a(\lambda)$ that has $\mathring{A}_{abs}$ = 3.45 from 400 to 600 nm wavelength (Figure 2.3e). This curve (the bold black curve in Figure 2.7) is essentially parallel to that of PGS but lower by a factor of ~3.

2.7. Single-scattering by mineral dust particles

Single-scattering results for dust with the above specifications are shown in Figure 2.3. The single-scattering albedo of dust is much higher than that of BC, but the effect of dust-scattering on snow albedo is negligible except at very large dust mass fractions, because the scattering by snow grains is dominant. It is the absorption properties of dust that are relevant, and Figure 2.3e shows that B_a for dust is two orders of magnitude smaller than B_a for BC. However, in part because of its larger particle size, the mass of dust in snow can also be orders of magnitude larger than the mass of BC, making its contribution to albedo reduction comparable to or greater than that of BC (*Painter et al.*, 2007; *Wang et al.*, 2013; *Doherty et al.*, 2014).

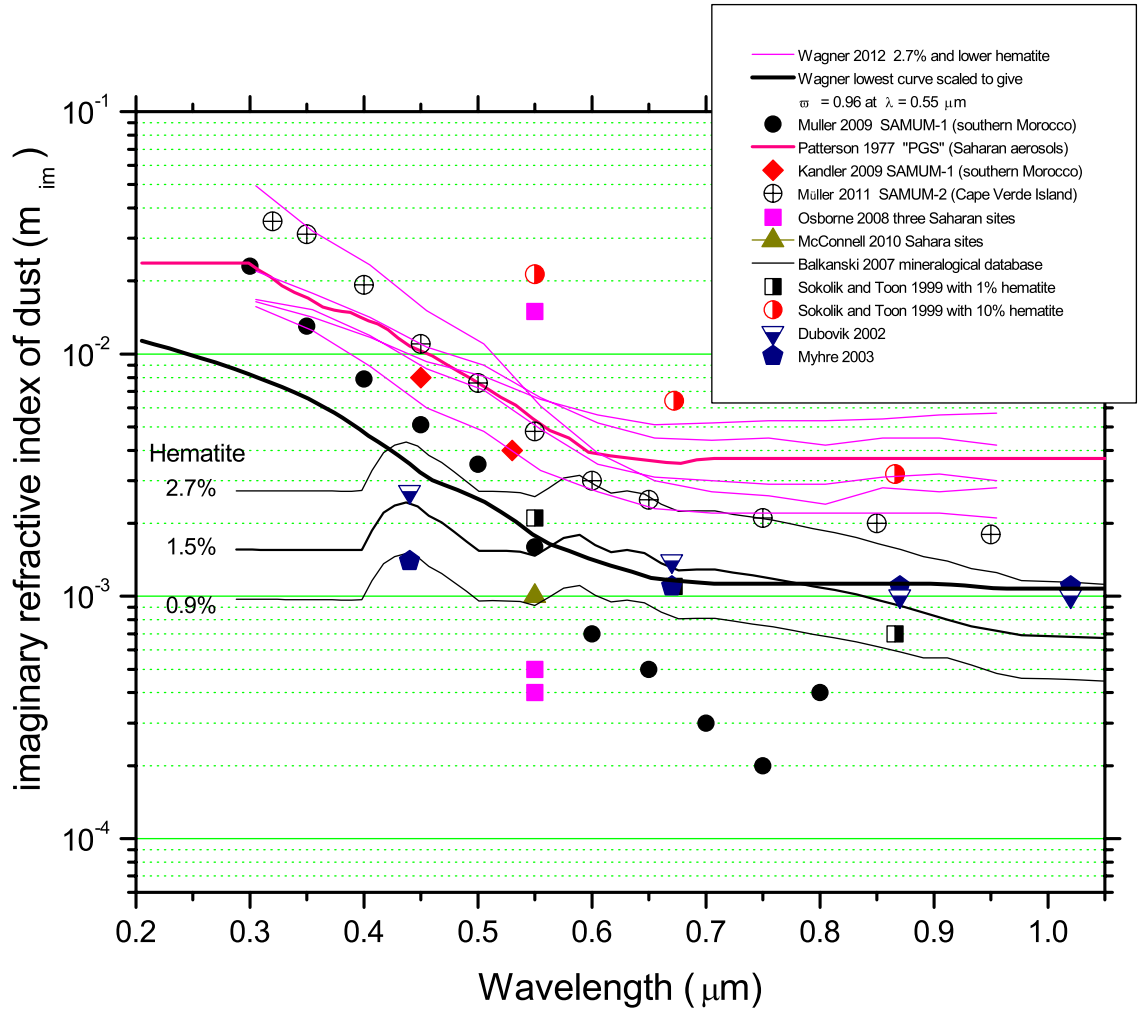

Figure 2.7. Spectral absorption coefficient of mineral dust, expressed as the imaginary part of the complex index of refraction (m_{im}), from field measurements at several locations discussed in the text. The bold blue curve is from Patterson, Gillette, and Stockton (1977) ("PGS"); it was used in our earlier modeling as "red dust" (Warren and Wiscombe, 1980). The "Wagner lowest curve" (Wagner et al., 2012) is also shown scaled down by a constant factor to obtain a single-scattering albedo $\varpi = 0.96$ at $\lambda = 550$ nm, resulting in the bold black curve, used for the computations in this paper. The extrapolation to longer and shorter wavelengths is based on the spectral behavior of hematite and goethite (Sherman and Waite, 1985).

2.8. Albedo reduction by dust in snow

Figure 2.8 shows the effect on spectral albedo of adding dust to snow, in mass fractions from 10^{-6} to 10^{-1}, as well as the end-member spectra for pure snow and pure dust. These plots may be compared to the similar plots for BC in snow shown in Figure 2.4. The spectral albedo of dust is approximately opposite that of snow, in that the albedo for pure dust is low at visible and UV wavelengths, and higher in the near-IR. The curves in Figure 2.8a all cross at λ = 1.2 μm, where the albedo of pure dust equals the albedo of pure snow at a value α_λ = 0.64. The wavelength of this cross-point varies with snow grain size; for r = 1000 μm the curves cross at α_λ = 0.9 mm, α_λ = 0.60 (Figure 2.8b). As was also seen for BC, a given mass fraction of dust causes a greater reduction of albedo in coarse-grained snow than in fine-grained snow (compare Figure 2.8b to Figure 2.8a). In Figure 2.9b, the asymptote for pure dust gives an albedo of 0.5, somewhat higher than that of desert surfaces (*Smith*, 1986; *Otterman and Fraser*, 1976), probably because airborne dust has a smaller particle size than surface soil.

The allwave albedo as a function of the mass fraction of BC or dust is shown in Figures 9a and 9b, respectively. Three of the curves in Figure 2.9b show a weak minimum of albedo for dust mass fractions between 10^{-3} and 10^{-1}, depending on snow grain size. This peculiarity is a consequence of the spectral contrast of ice and dust particles (Figure 2.8); it is not seen with BC (Figure 2.9a). At these dust fractions, dust begins to affect the albedo not only by absorption but also by scattering, and by limiting the penetration depth of radiation into the snowpack.

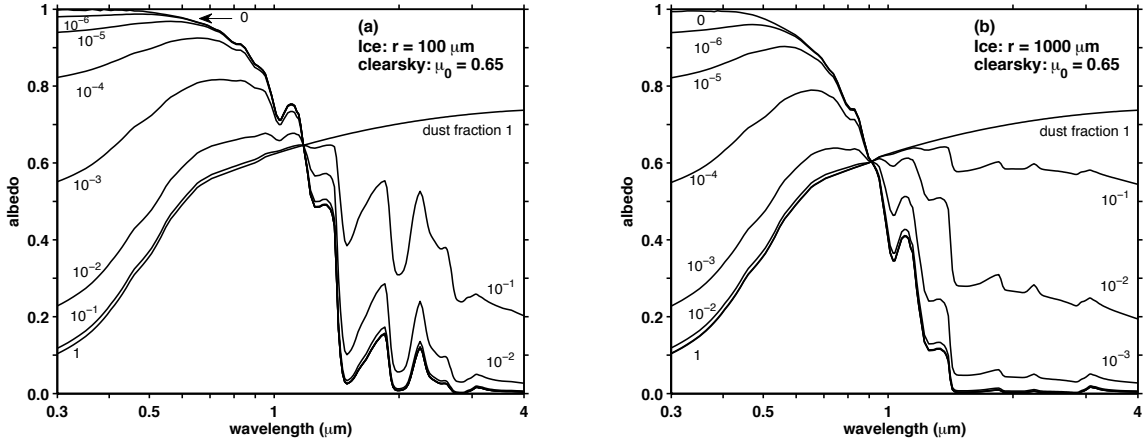

Figure 2.8. Spectral albedo of pure snow, and of snow containing mineral dust at several mass fractions between 0 and 1. These computations use the dust absorption spectrum shown as the bold black curve in Figure 2.7. (a) Snow grain radius r = 100 μm; (b) r = 1000 μm.

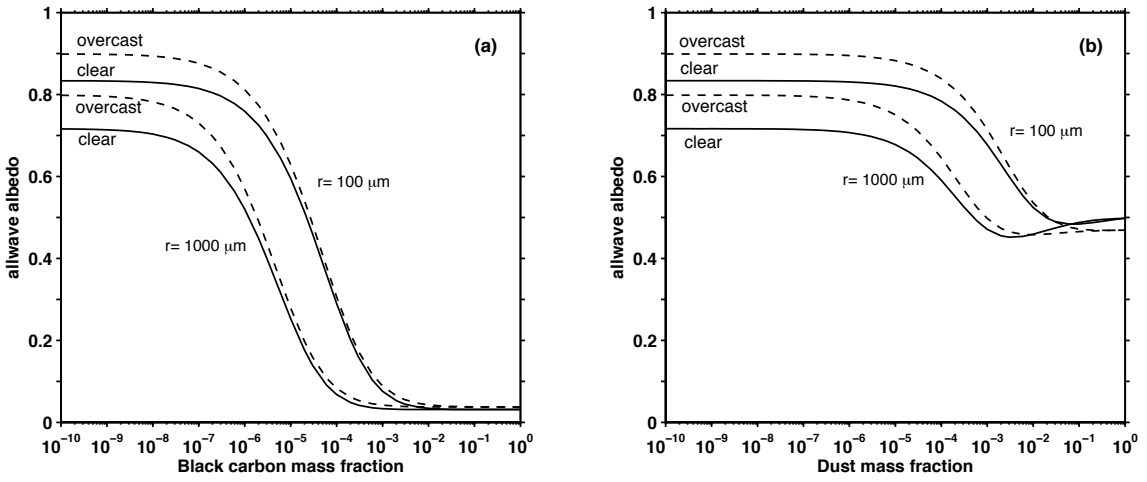

Figure 2.9. Allwave albedo as a function of the mass fraction of (a) BC or (b) dust, for two snow grain sizes (r = 100 and 1000 μm) and two incident solar spectra (clear sky and overcast sky). The plot for BC is an update of Figure 1 of Warren and Wiscombe (1985), using revised optical constants of ice and revised optical properties of BC.

Comparing Figures 9a and 9b, it is apparent that, for dust mass fractions $C_d \leq 10^{-4}$, the dust curves can match the BC curves if the dust curves are shifted to the left by a factor $f \approx 200$. Thus for allwave albedo the effect of dust can be mimicked by BC present at a mass fraction ~0.5% as large. BC and dust mass fractions can therefore be combined into an "equivalent BC" mass fraction. Using the terminology of *Grenfell et al.* (2011), the "BC-equivalent" mass fraction, C_{BC}^{eq}, is given by:

$$C_{BC}^{eq} = C_{BC} + C_d / f \,. \tag{E8}$$

The factor f varies with C_d, so we now investigate how to express this dependence. Figure 2.10 compares $\Delta\alpha$ for BC and dust for mass fractions $<10^{-5}$. We show results only for visible and allwave, because dust in these amounts causes little change to the broadband near-IR albedo. (At a mass fraction of 10^{-5}, the near-IR $\Delta\alpha$ does not exceed 0.002; even at a mass fraction of 10^{-4}, $\Delta\alpha$ does not exceed 0.01.) As mentioned above, this is because the near-IR albedo of pure dust is close to that of pure snow.

We now ask how far to the left a point on the dashed curves (dust) of Figure 2.10 must be moved to reach the solid curves (BC). The result of this exercise is shown in Figure 2.11, a curve about two orders of magnitude below the 1:1 line, but with a slope smaller than 1:1, implying that f increases with C_d. Figure 2.12 plots f as a function of C_d for dust mass fraction $\leq 10^{-4}$. The quadratic fits (solid curves) can be used to calculate the factor f as a function of C_d. Define $x \equiv \log_{10}$ [C_d (ppm)]. Then

$$f = v_0 + v_1 x + v_2 x^2 \,. \tag{E2.9}$$

The coefficients are given in Table 2.5.

For allwave albedo at large C_d (Figure 2.12a), the curve is a poor fit to the data. However, we must remember that our aim is to obtain accuracy not in f but rather in $\Delta\alpha$, and it turns out that $\Delta\alpha$ is not very sensitive to f in this range. The error in calculated albedo reduction caused by representing dust as an "equivalent BC" ranges from 10^{-5} to 3×10^{-2}, depending on the dust mass fraction and snow grain size (Figure 2.13). For $r \leq 1000$ μm the error does not exceed 0.01. More figures related to the estimation and evaluation of the factor f is included in the supplemental material (Appendix A-2).

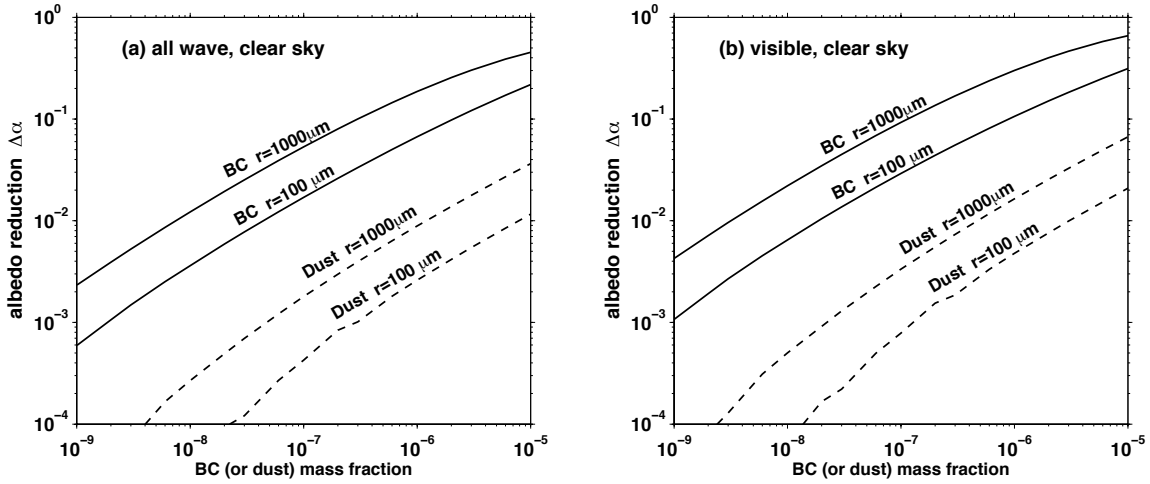

Figure 2.10. Comparison of albedo reduction by BC (as in Figure 2.5) and by dust. (a) allwave; (b) visible. The "BC-equivalent" of dust is determined by shifting the dust curves to the left until they align with the BC curves (Figure 2.11).

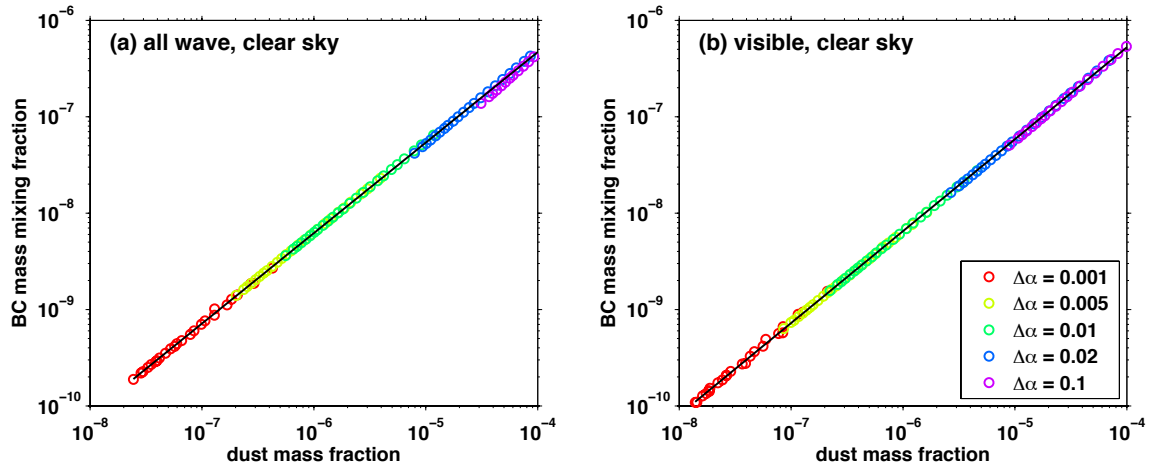

Figure 2.11. Mass fraction of BC needed to obtain the same Δα resulting from a given mass fraction of dust. Each point is for a particular value of Δα. (a) allwave; (b) visible.

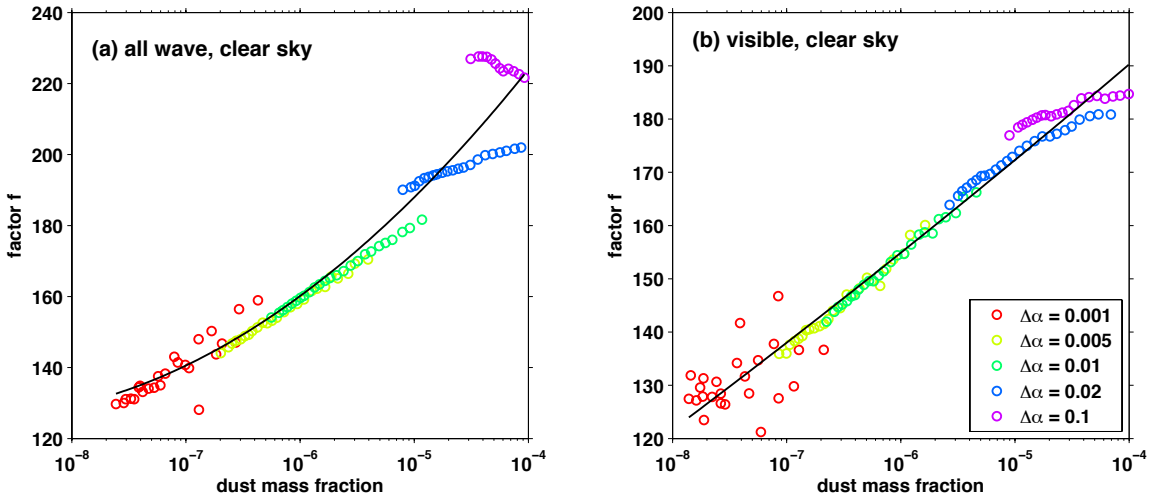

Figure 2.12. Factor f by which the dust mass fraction must be divided to obtain its BC-equivalent, as a function of dust mass fraction, for several values of Δα. The solid curve is used to parameterize f as a function of C_d.

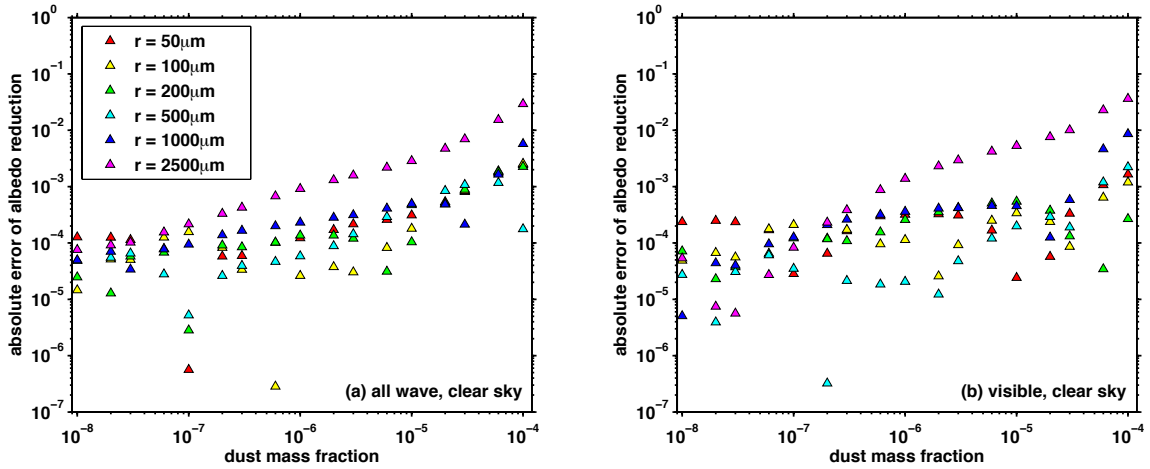

Figure 2.13. Error in $\Delta\alpha$ resulting from approximating C_d as the equivalent mass fraction of C_{BC}, as given by the solid curves from Figure 2.12.

2.9. Combinations of dust and BC

If BC and dust are both present at low mixing ratios, e.g. 10 ng/g, their effects in reducing snow albedo are just additive ($\Delta\alpha \approx \Delta\alpha_{dust} + \Delta\alpha_{BC}$), but for larger mixing ratios $\Delta\alpha < \Delta\alpha_{dust} + \Delta\alpha_{BC}$. Computations of the potential benefits of reducing BC emissions must therefore account for the presence of dust and soil loading in snow. Dust content can be quite high in mountain glaciers. For example, in the Himalaya, *Ming et al.* (2013) reported that the effect of BC was notably muted because of the high dust content.

Figure 2.14 shows the allwave albedo of dust-laden snow as a function of added BC, and Figure 2.15 shows the reduction of allwave albedo by BC for several pre-existing dust contents in the snow. A related figure on this same topic was shown by *Bond et al.* (2013) as their Figure 30.

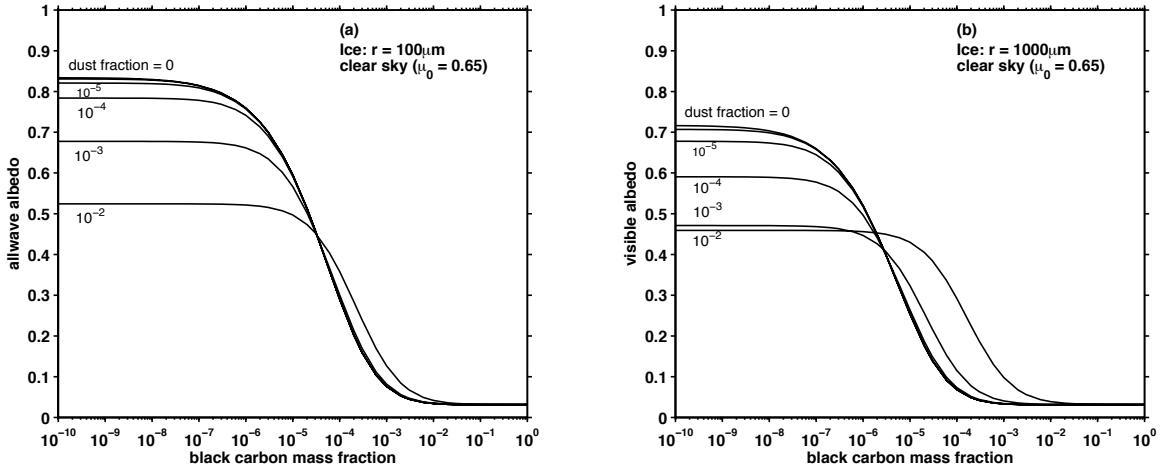

Figure 2.14. The combined effect of dust and BC on allwave albedo, as a function of BC mass fraction, for snow containing dust at several mass fractions. (a) Snow grain radius r = 100 μm; (b) r = 1000 μm.

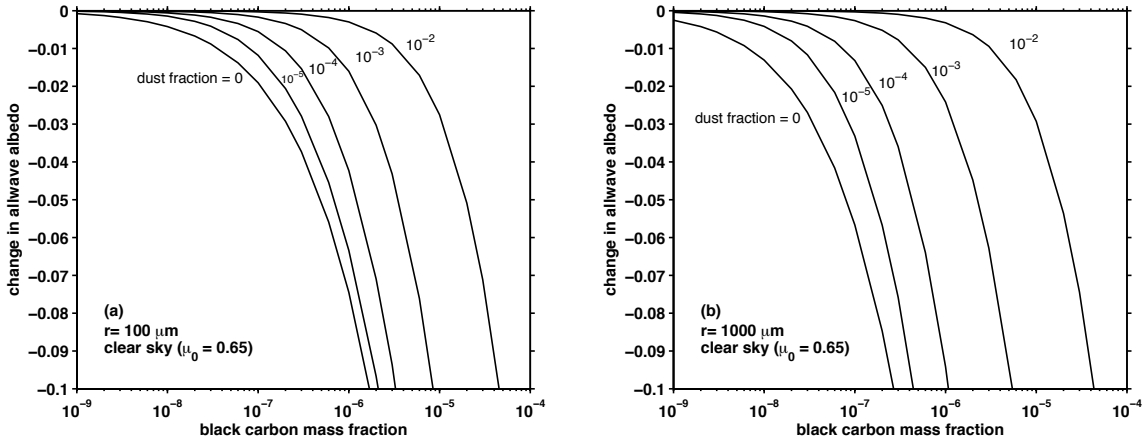

Figure 2.15. Change in allwave albedo due to addition of BC to already-dusty snow, as a function of BC mass fraction. (a) Snow grain radius r = 100 μm; (b) r = 1000 μm.

2.10. Summary

The broadband albedo of pure deep snow can be represented by a simple quadratic function of grain size, but natural snow usually contains sufficient impurities to significantly affect the albedo. Black-carbon mixing ratios in snow, remote from sources of pollution, vary over four orders of magnitude. Here we have parameterized the reduction of broadband snow albedo ($\Delta\alpha$) due to BC in these amounts, using a quadratic or cubic polynomial in BC mixing ratio, whose coefficients are themselves quadratic in snow grain size. We also have combined grain size and BC into a single predictor for a much simpler parameterization of $\Delta\alpha$, but with the allowable grain-radius domain limited to $r \geq 50$ μm. For reduction of visible albedo, we have shown that the effect of mineral dust on snow albedo can be represented, via a divisor, by using an "equivalent" BC mixing ratio. The addition of mineral dust to snow does not significantly change the broadband albedo for the near-IR band (0.7 - 4.0 μm), because the absorption properties of dust grains and snow grains are similar when averaged over this wavelength domain.

The model calculations on which the parameterizations are based required assumptions about the size distributions and complex refractive indices for the particulate impurities. The parameterizations can be used for BC and dust of different sizes and refractive indices by scaling the mass-mixing ratio in the parameterization according to the ratios of their spectral mass-absorption cross-section B_a (Figure 3e).

Acknowledgments

We thank Tom Grenfell for providing digital values of the measured solar spectra and Yves Balkanski for digital values from his published figures. We thank Sarah Doherty, Dean Hegg, Tony Clarke, Dorothy Koch, Qiang Fu, Charlie Zender, Steve Hudson, Tom Ackerman, and Cecilia Bitz for helpful discussion. We thank Sarah Doherty for her review of an early draft of the paper. The research was supported by NSF grant AGS-11-18460.

Table 2.1. Parameterization for broadband albedo a of pure snow as a function of snow grain radius r, relative to r_0= 100 μm.

The albedo α is given as

$$\alpha = m_0 + m_1 r_n + m_2 r_n^2, \text{ where } r_n \equiv \log_{10}(r/r_o).$$

The coefficients are given below. Coefficients are also available for RRTM bands in the supplemental material.

Clear sky			
Band	m_0	m_1	m_2
Allwave 0.3-4.0 μm	0.8344	-0.1007	-0.0177
Visible 0.3-0.7 μm	0.9849	-0.0215	-0.0132
Near-IR 0.7-4.0 μm	0.6596	-0.1927	-0.0229
Overcast cloud			
Band	m_0	m_1	m_2
Allwave 0.3-4.0 μm	0.8994	-0.0793	-0.0221
Visible 0.3-0.7 μm	0.9856	-0.0202	-0.0125
Near-IR 0.7-4.0 μm	0.7493	-0.1820	-0.0388

Table 2.2. Parameterization for broadband albedo reduction due to BC.

(a) Definitions

r = snow grain radius (μm)

r_o = 100 μm

C = black-carbon mass fraction

$C_0 = 10^{-6}$

$r_n = \log_{10}(r/r_0)$

$C_n = \log_{10}(C/C_0)$

$\Delta\alpha$ = reduction from the albedo of pure snow

$\Delta\alpha_n = \log_{10}(\Delta\alpha\ (r/C))$

(b) Domains of broadband albedo parameterizations, defined by illumination wavelength band and mass fraction C of black carbon.

Band boundaries (μm)	Range 1 $1\times10^{-7} < C < 10^{-5}$	Range 2 $C_{low} \le C < 3\times10^{-7}$	Range 3 $0 < C \le C_{low}$
Allwave (0.3-4.0)	Cubic Functions: $\Delta\alpha_n = f(C_n)$ Coefficients are quadratic functions of r_n		Linear function $\Delta\alpha = f(C)$
Visible (0.3-0.7)			
Near –IR (0.7-4.0)	Quadratic Functions: $\Delta\alpha_n = f(C_n)$ Coefficients are quadratic functions of r_n		

(c) Functional forms of parameterizations

For Ranges 1 and 2 the parameterization is

$$\log_{10}\Delta\alpha = q_0 + q_1 C_n + q_2 C_n^2$$

where the q_i are quadratic/cubic functions of *r*:

$$q_2 = p_{4,1} + p_{3,1} r_n + p_{2,1} r_n^2 + p_{1,1} r_n^3$$
$$q_1 = p_{4,2} + p_{3,2} r_n + p_{2,2} r_n^2 + p_{1,2} r_n^3$$
$$q_0 = p_{4,3} + p_{3,3} r_n + p_{2,3} r_n^2 + p_{1,3} r_n^3$$

For the near-IR a quadratic function is sufficient, so $p_{1.i} = 0$.

A minimum value of *C*, called C_{low}, is determined for Range 2, below which a linear function is used (Range 3); C_{low} is a quadratic function of r_n:

$$C_{low} = j_1 + j_2 r_n + j_3 r_n^2.$$

The coefficients j are given below. For BC mixing ratio lower than C_{low}, $\Delta\alpha$ is calculated by linear interpolation between $C = C_{low}$ and $C = 0$:

$$\Delta\alpha = t\, C/C_{low},$$

where the *t* is the albedo reduction produced by C_{low} ; the values of *t* are listed below.

(d) Coefficients for the parameterizations.

Range 1 ($10^{-7} < C < 10^{-5}$)

Clear sky (sza = 49.5°)				Overcast sky			
	$p_{row,1}$	$p_{row,2}$	$p_{row,3}$		$p_{row,1}$	$p_{row,2}$	$p_{row,3}$
Allwave 0.3-4 μm	0.0068	-0.0188	-0.0003	Allwave 0.3-4 μm	0.0080	-0.0190	-0.0002
	-0.0257	-0.0114	-0.0575		-0.0263	-0.0099	-0.0584
	-0.0217	-0.0586	0.4755		-0.0223	-0.0615	0.4747
	-0.0429	0.5501	-1.1265		-0.0437	0.5373	-1.0598
Visible 0.3-0.7 μm	0.0078	-0.0191	0.0006	Visible 0.3-0.7 μm	0.0089	-0.0193	0.0006
	-0.0265	-0.0083	-0.0551		-0.0269	-0.0074	-0.0566
	-0.0229	-0.0595	0.4795		-0.0234	-0.0625	0.4778
	-0.0471	0.5099	-0.9260		-0.0468	0.5045	-0.9192
Near-IR 0.7-4 μm	0	0	0	Near-IR 0.7-4 μm	0	0	0
	-0.0148	-0.0246	-0.0758		-0.0143	-0.0243	-0.0758
	-0.0279	-0.0503	0.4454		-0.0280	-0.0510	0.4452
	-0.0925	0.7936	-1.6215		-0.0960	0.7856	-1.5340

Range 2 ($C_{low} < C < 3\times10^{-7}$)

Clear sky (sza = 49.5°)				Overcast sky			
	$p_{1,row}$	$p_{2,row}$	$p_{3,row}$		$p_{1,row}$	$p_{2,row}$	$p_{3,row}$
Allwave 0.3-4 μm	0.0278	-0.0003	0.0013	Allwave 0.3-4 μm	0.0254	-0.0096	-0.0032
	-0.0762	-0.0761	-0.0756		-0.0801	-0.0767	-0.0760
	0.0465	0.0495	0.5140		0.0575	0.0689	0.5225
	-0.0420	0.5370	-1.1367		-0.0478	0.5119	-1.0763
Visible 0.3-0.7 μm	0.0184	-0.0280	-0.0120	Visible 0.3-0.7 μm	0.0243	-0.0180	-0.0073
	-0.0793	-0.0722	-0.0711		-0.0839	-0.0758	-0.0734
	0.0729	0.1096	0.5468		0.0680	0.0936	0.5379
	-0.0592	0.4719	-0.9470		-0.0575	0.4681	-0.9398
Near-IR 0.7-4 μm 0.0848	0	0	0	Near-IR 0.7-4 μm	0	0	0
	-0.0077	-0.0139	-0.0720		-0.0090	-0.0169	-0.0733
	0.0042	-0.0007	0.4631		0.0062	0.0038	0.4656
	-0.0206	0.9056	-1.5820		-0.0208	0.9038	-1.4919

Range 3 ($0 < C < C_{low}$)

Clear sky (sza = 49.5°)					Overcast sky				
	j_1	j_2	j_3	t		j_1	j_2	j_3	t
Allwave	0.1772	0.8819	-2.8083	0.001	Allwave	0.1997	-0.9173	-2.9212	0.001
Visible	0.2261	-0.9496	-3.1095	0.001	Visible	0.2357	-0.9643	-3.1416	0.001
Near-IR	0.0827	-0.4755	-2.5269	0.0001	Near-IR	0.0848	-0.4773	-2.6194	0.0001

Table 2.3. Simple parameterization for Δα, combining r and C.

The snow grain radius *r* and BC mixing ratio *C* are combined into a single variable *H* (Eq. 2.7) for computation of albedo reduction Δα (Eq. 2.8). The exponent *s* for Eq. 2.7 and the coefficients *m* for Eq. 2.8 are given here. The parameterization is valid for grain radii 50-2500 μm.

	m_1	m_2	m_3	s	Valid range of H
Clear sky					
Allwave	-0.042	0.560	-1.110	0.73	$1.4\times10^{-3} < H < 1.6$
Visible	-0.049	0.525	-0.893	0.73	$6.9\times10^{-4} < H < 0.63$
Near –IR	-0.053	0.827	-1.623	0.43	$3.2\times10^{-3} < H < 6.3$
Overcast cloud					
Allwave	-0.043	0.547	-1.038	0.73	$1.1\times10^{-3} < H < 1.2$
Visible	-0.050	0.514	-0.890	0.73	$6.6\times10^{-4} < H < 0.79$
Near –IR	-0.050	0.832	-1.533	0.43	$2.5\times10^{-3} < H < 5.0$

Table 2.4. Bands for the Rapid Radiative Transfer Model (RRTM) (Mlawer and Clough, 1997)

Band number	wavelength boundaries (μm)	
	low	high
1	0.2000	0.2632
2	0.2632	0.3448
3	0.3448	0.4415
4	0.4415	0.6250
5	0.6250	0.7782
6	0.7782	1.2422
7	1.2422	1.2987
8	1.2987	1.6260
9	1.6260	1.9417
10	1.9417	2.1505
11	2.1505	2.5000
12	2.5000	3.0769
13	3.0769	3.8462
14	3.8462	12.1951

Table 2.5. Parameterization of the factor f as a function of dust mass fraction.

To compute albedo reduction for the allwave and visible bands, the dust mass fraction C_d is converted into BC-equivalent mass fraction by dividing by the factor f, which is a function of C_d. The factor f is obtained from Eq. 2.9 with coefficients listed here.

Clear sky				Overcast sky			
	v_0	v_1	v_2		v_0	v_1	v_2
Allwave	159	23.94	4.30	Allwave	155	20.97	2.41
Visible	155	17.15	0.27	Visible	152	15.92	-0.39

Chapter 3

Effect of Snow Grain Shape on Snow Albedo

Cheng Dang, Qiang Fu and Stephen G. Warren

[1]*Department of Atmospheric Sciences, University of Washington, Seattle, WA 98195-1640, USA*

Published on Journal of the Atmospheric Sciences, 2016

doi: 10.1175/JAS-D-15-0276.1

3.0. Abstract

Radiative transfer models of snow albedo have usually assumed spherical snow grains, using Mie theory to compute single-scattering quantities. The scattering by realistic nonspherical snow grains is less in the forward direction and more to the sides, resulting in a smaller asymmetry factor g (the mean cosine of the scattering angle). Compared to a snowpack of

spherical grains with the same area-to-mass ratio, a snowpack of nonspherical grains will have a higher albedo, thin snowpacks of nonspherical grains will more effectively hide the underlying surface, and light-absorbing impurities in the snowpack will be exposed to less sunlight. These effects are examined here for a variety of snow grain shapes, with aspect ratio from 0.1 to 10. The albedo of an opaque snowpack with equidimensional non-spherical snow grains (aspect ratio 1) is higher than that with spherical snow grains by 0.036 and 0.05, for equivalent grain radius 100 μm and 1000 μm; respectively. For equivalent radius of 100 μm, the albedo reduction caused by 100 ppb black carbon is 0.02 for spherical snow grains, but only 0.01 for equidimensional non-spherical snow grains. The effect on albedo of a smaller g can be mimicked by using a smaller grain radius with a spherical g; this is why radiative-transfer models using spherical grains were able to match measurement of spectral albedo. The scaling factor is different for different aspect ratios, and is about 2.4 for equidimensional snow grains.

3.1. Introduction

The albedo of snow is higher than that of any other natural surface on Earth, but it varies greatly with wavelength, snow condition, and the amount of light-absorbing particles (LAPs) in snow (*Wiscombe and Warren* 1980*; Warren and Wiscombe* 1980*; Warren* 1982; *Aoki et al.,* 2000; *Carmagnola et al.,* 2013). A change of snow albedo directly affects the solar energy absorbed by a snowpack, influencing climate (*Hansen and Nazarenko* 2004; *Flanner et al.,* 2007; *Bond et al.,* 2013), hydrology through determining the melting rate (*Painter et al.*, 2007, 2012; *Qian et al.,* 2009), and snow photochemistry (*Grannas et al.,* 2007*; Zatko et al.,* 2013). Therefore, an accurate calculation of snow albedo is crucial for modeling environmental processes involving snow.

In current climate and hydrology models, snow albedo is calculated using either a coupled radiative transfer model or a parameterization developed based on radiative transfer calculations. Models calculating the spectral albedo of snow were developed in 1980 for pure snow by *Wiscombe and Warren* (1980) and for snow containing black carbon (BC) by *Warren and Wiscombe* (1980). Their work was adapted later by Flanner and his colleagues, who developed a multi-layer radiative transfer model SNICAR (Snow, Ice, and Aerosol Radiative model), that allows one to simulate snow albedo for different snow conditions and different contents of LAPs (*Flanner et al.,* 2007*, Flanner and Zender,* 2006). The SNICAR model has been incorporated as a subroutine in the standard implementation of National Center for Atmospheric Research's (NCAR's) Community Earth System Model (*Lawrence et al.,* 2011). For climate studies with longer time scales, a parameterization of snow albedo for a few bands, instead of a spectral radiative transfer model, is more practical. Various parameterizations have been developed to calculate the broadband and narrowband albedo of snow (e.g. *Marshall and Warren,* 1987; *Gardner and Sharp,* 2010; *Aoki et al.,* 2011; *Dang et al.,* 2015*).* The authors used radiative transfer models to calculate the snow albedo for different snow conditions and LAP contents, and then fitted the snow albedo to analytical functions that can be used in climate models. These models and parameterizations have considered many factors that influence the snow albedo, including snow grain size, snow depth, solar zenith angle, underlying surface albedo, cloud optical thickness, and content of LAPs. However, they share one fundamental assumption, namely that a snowpack can be represented by a collection of ice spheres. That assumption is questionable.

The shapes of snow grains (ice crystals) in nature vary significantly depending on the snow age and meteorological conditions during and after snowfall, and are usually

nonspherical and irregular in shape (*LaChapelle,* 1969). To calculate the snow albedo using a radiative transfer model, one needs to know *a priori* the single-scattering properties of ice crystals: extinction efficiency, single-scattering albedo (ϖ), and asymmetry factor (g). Physically based methods (e.g. Geometric Optics, Ray-Tracing, and Monte Carlo) to calculate these properties are available for various shapes of crystals (*e.g. Yang and Liou* 1995, 1996*; Macke et al.,* 1996*; Sun et al.,* 1999), but computationally efficient and well-established analytical methods are available only for spheres, by use of Mie theory (e.g. *Wiscombe*, 1980). Resorting to Mie theory, it is therefore common practice to represent a nonspherical ice crystal by an effective spherical ice crystal with the same volume or the same surface area, or a collection of effective spherical ice crystals with the same volume-to-area ratio (we adopt this definition when referring to effective snow grain radius in this paper). The effective radius r_e is then defined by the specific surface area β, as

$$r_e \equiv 3/(\rho_i \beta) \tag{E3.1}$$

where ρ_i is the density of pure ice, 917 kg m^{-3} , and β is the area-to-mass ratio of the bulk snowpack, with units m^2 kg^{-1}, for example. The accuracy of ice optical properties obtained by using such effective spheres is critical when performing the snow albedo calculation.

Beginning in the 1990s, a series of papers were published to evaluate the equal-volume-to-area representation for different shapes of ice crystals in clouds and snow, including circular cylinders (*Grenfell and Warren* 1999), hexagonal prisms (*Fu et al.,* 1999*, Neshyba et al.,* 2003), and hollow prisms (*Grenfell et al.,* 2005). These studies show that the equal-volume-to-area prescription works well to compute the extinction efficiency and single-scattering albedo (as had also been shown in Figure 1 of Fu et. al. 1998), but is less accurate for the asymmetry factor. The error in g is largest if the aspect ratio of the nonspherical ice crystal is equal to 1

(equidimensional). For example, at wavelength λ = 0.5 μm, a sphere has g = 0.89 but a solid equidimensional hexagonal prism has g = 0.77 (*Neshyba et al.,* 2003*,* Figure 7). The calculated visible albedo of an ice cloud can therefore be quite inaccurate, despite the accurate extinction efficiency and single-scattering albedo.

Experimental evidence for how nonsphericity causes reduction of the asymmetry factor was shown in measurements on firn (old snow) and glacier ice in East Antarctica. In the case of ice, the scattering is by air bubbles in ice rather than ice grains in air, but the effects of nonsphericity may be similar. From measurements of spectral albedo, *Dadic et al.* (2013) inferred the specific surface area, which in the case of ice is the ratio of the area of bubbles and cracks to the mass of ice. This inference was made with a radiative transfer model using a spectral asymmetry factor g for a spherical air bubble in ice, which is 0.86 at λ = 0.5 μm (*Mullen and Warren,* 1988). But the bubble shapes were not spherical, and direct measurements of β, obtained by X-ray tomography of the firn and ice samples, was ~50% lower than the value inferred from the albedo measurement. *Dadic et al.* pointed out that, if they used the β as obtained from measurement in the modeling, g used in radiative transfer model needs to be reduced by factors ranging from 0.78 to 0.94 to match the measured albedo. For firn the average factor was 0.82, implying g ~ 0.71. In other words, the measured β and inferred β could be brought into agreement if the radiative transfer model uses g ~ 0.71 instead of g = 0.86 at λ = 0.5 μm.

Experimental evidence also comes from measurements of ice crystals in clouds. The asymmetry factors of cirrus clouds derived from observation are 0.7 from *Stephens et al.* (1990), 0.75 from *Garrett et al.* (2001) and 0.8 from *Francis et al.* (1994). In the most recent MODIS retrieval algorithm (http://modis-atmos.gsfc.nasa.gov/products_C006update.html), a single

habit of severely roughened aggregated columns with an asymmetry factor of 0.75 is assumed, which led to much improved agreement with the cloud optical depth retrieval from an independent method IR IOT (*Holz et al.,* 2015). Therefore, both theory and observations, along with the knowledge that snow grains are nonspherical, indicate that the value of g used to compute snow albedo is too large.

Many parameterizations of single-scattering properties of nonspherical ice crystals are available, aiming mainly for the application in retrieving and computing the optical properties of ice clouds (e.g. *Fu* 1996, 2007*; Yang et al.,* 2000; *Key et al.,* 2002; *Baum et al.,* 2011; *Van Diedenhoven et al.* 2014*).* Fewer have been developed for optical properties of nonspherical snow grains. *Libois* and coworkers (2013, 2014) studied the influence of snow grain shape on vertical profiles of solar irradiance, and introduced two parameters (i.e., enhancement parameter and geometry asymmetry factor) to represent the snow grain shape. Very recently, *Räisänen et al.* (2015) developed a parameterization of the single-scattering properties of nonspherical snow grains based on the retrieved snow grain shape. The shape of snow grain they used is a combination of droxtals, plates and Koch fractals, which they selected by matching the measured phase function of blowing snow. The calculated asymmetry factor of nonspherical grains using their parameterization is lower than that of spheres. Despite the complex shapes of snow grains, the asymmetry factor of a nonspherical ice crystal mainly depends on the aspect ratio and distortion of its constituent units, for which hexagonal prisms have been demonstrated to be valid optical proxies (*Fu* 2007*; Yang and Fu,* 2009*; van Diedenhoven et al.,* 2012). Retrievals obtained by applying this assumption to airborne polarimetric measurements of snow have been presented by *Ottaviani et al. (*2015*).*

A hexagonal prism is described by its aspect ratio AR, the ratio of the diameter 2a of the basal plane to the length c ($AR = 2a/c$). Snow crystals in the atmosphere often have very large or very small AR (plates or columns, respectively), but within a day or so after falling to the ground processes of snow metamorphism (mainly by vapor transfer from convex to concave surfaces) cause the crystals to lose their intricate shapes, and become more equidimensional (*AR* approaches 1) (*LaChapelle*, 1969). Equidimensional nonspherical grains may appear similar to spheres, but their asymmetry factors actually show the greatest deviation from that of spherical grains. For a large range of AR ($0.1 < AR < 1$), the g of hexagonal prisms is smaller than g of spheres with the same effective radius.

A smaller g means that a photon is (on average) deflected through a larger angle in each scattering event, so it can re-emerge from the top of the snowpack after fewer scattering events. This will cause the albedo of pure deep snow to be greater, and will allow a thin snowpack to more effectively hide the underlying surface. As a consequence, a photon entering the snowpack is less likely to encounter LAPs (dust and BC) before re-emerging. In this paper, we aim to make a comprehensive survey of the effects of the asymmetry factor on snow albedo calculations under various conditions for both pure snow and snow containing LAPs.

3.2. Method

3. 2.1 Single scattering quantities of ice and black carbon

For spherical ice crystals, we calculated the extinction efficiency, single-scattering albedo, and asymmetry factor using Mie theory (*Wiscombe,* 1980), with spectral optical constants of ice from *Warren and Brandt* (2008), for 29 grain radii (r) from 20 to 2500 μm. For nonspherical ice crystals, we used the extinction efficiency and single-scattering albedo of spheres obtained from

the Mie calculation, and calculated their asymmetry factors using the parameterization developed by Fu (2007), assuming crystals with rough surfaces (light beams passing through the parallel planes of the ice crystals removed).

Fu (2007) parameterized the asymmetry factor of nonspherical ice crystals using the crystal mean aspect ratio and single-scattering albedo, for wavelength (λ) ranging from 0.25 μm to 4 μm, and for ice crystals with both smooth and rough surfaces. We chose the parameterization for crystals with rough surface as it is more representative of ice crystals in natural snowpacks. Fu's parameterization was developed based on the asymmetry factor of hexagonal prisms, but it reproduced the asymmetry factor of other nonspherical ice crystals including bullet rosettes, aggregates with rough surfaces, and fractals, and its results agree with observations made by *Garrett et al.,* (2001). Thus, in this work, we adopt Fu's parameterization to calculate the asymmetry factor of nonspherical ice crystals in general. The results obtained in this paper are expected to be applicable to a large variety of nonspherical crystal shapes

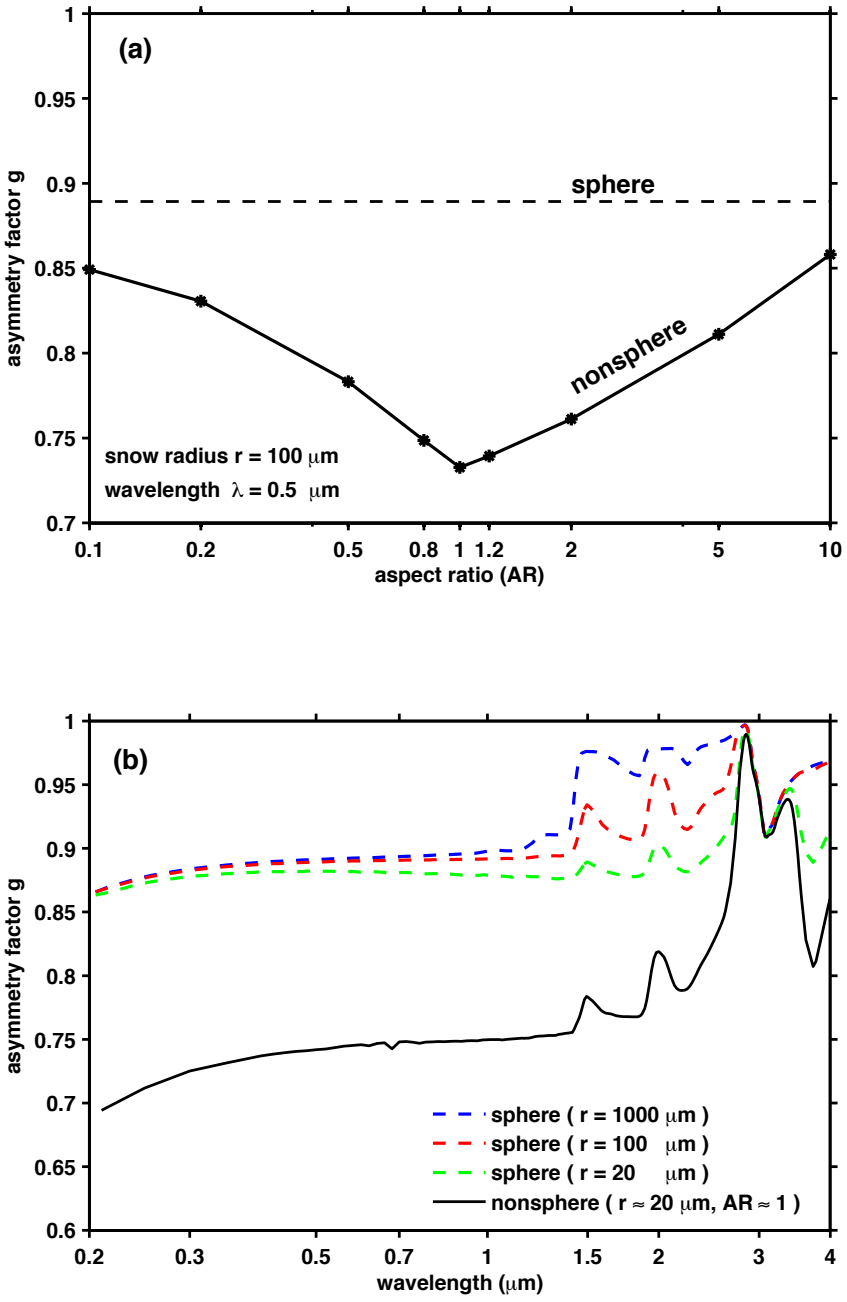

Figure 3.1. (a) Asymmetry factor g of a nonspherical ice crystal as a function of the aspect ratio (diameter/length) at wavelength λ = 0.5 μm. The values of g are calculated using the parameterization given by Fu (2007), for ice crystals with rough surface. The asymmetry factor of a spherical ice crystal (dashed line, g ≈ 0.89) is plotted as a reference. The effective radius of all ice crystals is 100 μm. (b) Asymmetry factor g as a function of wavelength. The values of g for spheres are computed using complex indices of refraction as given by Warren and Brandt (2008), for ice crystal radii r = 1000, 100 and 20 μm. The values of g for nonspheres are given by Fu (1996), for ice with effective radius r ≈ 20 μm and aspect ratio ~ 1 (Fu's ice crystal size spectra 5, with rough surface).

The calculated g of nonspherical ice crystals at wavelength λ = 0.5 μm is shown in Figure 3.1a. As was shown in Figure 2a of *Fu* (2007), and similarly in Figure 7 of *Neshyba et al.,* (2003), the asymmetry factor of a nonspherical ice particle decreases as AR increases from 0.1 to 1, then increases as AR increases from 1 to 10, with minimum $g \sim 0.74$. For comparison, g = 0.89 at λ = 0.5 μm for a spherical ice crystal (*Wiscombe and Warren*, 1980). Note that $g \sim 0.74$ is close to that suggested for firn based on observations (*Dadic et al.,* 2013), as well as that used by the MODIS cloud optical depth retrieval (*Holz et al.,* 2015), and that derived from in-situ aircraft observations in ice clouds (*Garrett et al.,* 2001).

The variation of g with wavelength is shown in Figure 3.1b for spherical ice crystals and for nonspherical ice crystals (data from *Fu,* 1996, based on the geometric ray tracing given by *Yang and Liou,* 1995). At visible wavelengths, the absorption of light by ice is so weak that the asymmetry factor is mainly determined by the shape of ice crystals, with little dependence on size. Spherical ice crystals with different effective radii have similar g, and the g of nonspherical ice crystals ($0.1 < AR < 1$) is much smaller than that of spherical ice crystals with the same area-to-mass ratio. For $\lambda > 1.4$ μm, the asymmetry factor depends on both particle shape and size. At these wavelengths, the absorption by ice becomes critical and a larger snow grain has a larger asymmetry factor. This is because the light intercepted by the larger grain is more likely to be absorbed, so the asymmetry factor is more dominated by the forward diffracted light (see Equation 2.2 *of Fu* 2007). Within the very strong absorption band around λ = 3 μm, ice particles with different sizes and shapes all have $g \sim 1$. Since 80% of the solar energy is at $\lambda <$ 1.4 μm where ice is weakly absorptive, the big discrepancy of g between spherical and nonspherical ice crystals is especially crucial in determining the albedo of a snowpack. *Jin et al.*

(2008) show a similar dependence of the asymmetry factor on wavelength, for grains with various shapes.

For BC, we use the same specifications as *Dang et al*. (2015). The density of BC is 1.8 g cm^{-3}, with lognormal size distribution of geometric width 1.3 and mass mean diameter 0.13 μm (*Clarke et al.,* 1987). The complex refractive index of BC is m = 1.95 – 0.79i, independent of wavelength. We assume that the BC particles are spheres (so we use Mie theory to calculate their single-scattering properties) and that they are externally mixed with the ice crystals. The single-scattering properties of the mixture are therefore a combination of single-scattering properties of BC and ice crystals (*Dang et al*., 2015). The absorption will be enhanced if the BC are internally mixed with ice crystals (*Flanner et al.,* 2012; *Liou et al.,* 2014).

3.2.2 Radiative transfer calculation

Given single-scattering properties of snow, the spectral albedo of a snowpack is calculated using the delta-Eddington approximation (*Joseph et al.,* 1976; *Wiscombe and Warren,* 1980). The spectral albedo is then used to calculate the broadband albedo (λ = 0.2 - 4 μm), using the incident solar spectrum measured at the sea surface in the Arctic Ocean during summer under clear sky by *Grenfell and Perovich* (2008). Considering a snow density of 300 kg m^{-3}, we perform these calculations for snowpacks of several thicknesses (2, 5, 30, 100 and 99999 cm; the latter, for this value of density, can be considered as "optically semi-infinite" for any grain size). We consider snow consisting of spherical snow grains and nonspherical snow grains of different AR, containing BC mass fractions varying from 0 (pure snow) to 1 (pure BC), and for four solar zenith angles (SZA): 0°, 30°, 49.5°, and 75°. We assume the underlying ground is black (i.e. the albedo is 0).

Because the asymmetry factor of nonspherical ice crystals is roughly symmetric about AR = 1 (Figure 3.1a), we show the results only for AR ≥ 1. For AR < 1, the results are the same as the case of AR > 1 that has the same asymmetry factor. Moreover, we will show the results for SZA = 49.5° unless otherwise stated, since the cosine of this angle (0.65) is close to that of the insolation-weighted solar zenith cosine for the sunlit hemisphere of Earth.

3.3. Results

3.3.1 Spectral Albedo

The spectral albedo (α_λ) of opaque deep snow is shown in Figure 3.2 for both spherical grains and nonspherical grains with effective radii of 100 μm (new snow) and 1000 μm (old snow). Recall from Figure 3.1 that the asymmetry factor of nonspherical grains is smaller than that of spherical grains, so the light is less likely to be scattered forward and more likely to emerge out of the snowpack after fewer reflection and refraction events. If the absorption of light by opaque snow is very weak, the incident photons will eventually emerge out of the snowpack in both cases, so that at visible and ultraviolet wavelengths, the albedo of nonspherical snow and spherical snow are similar and close to 1 (top panel of Figure 3.2). At near-IR wavelengths, where the snowpack is moderately absorptive, the photons traveling shorter distances in the snowpack are less likely to be absorbed; therefore the albedo of nonspherical grains is larger than that of spherical grains.

The situation is different if the snow contains BC. For BC amounts up to 10^4 ng/g, higher BC concentration results in a larger albedo difference between nonspherical and spherical snow in the visible, while in the near-IR, the albedo difference is almost independent of BC concentration, since ice dominates the light absorption at these wavelengths (bottom panels of Figure 3.2). After weighting the albedo difference by the incident solar spectrum, we

find that for pure snow only 10% of the albedo difference is due to the visible band ($\lambda < 0.7$ μm); as the BC concentration increases to 100 ng/g and 1000 ng/g, this fraction increases to 25% and 55%, respectively. The rest of the albedo difference is associated with the near-IR contribution. For shallow snow, the spectral albedo will also depend on the snow thickness and the albedo of the underlying surface, as will be shown later.

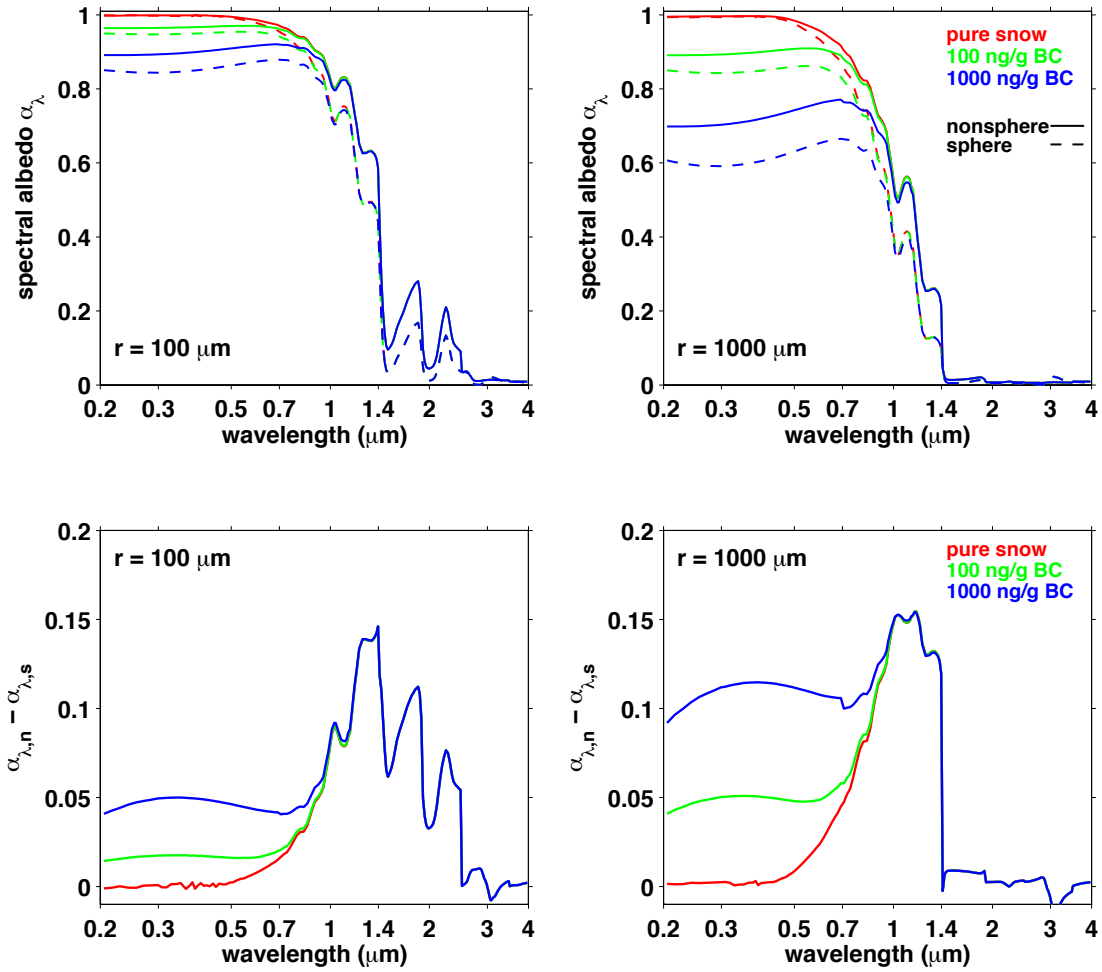

Figure 3.2. Top: spectral albedo (α_λ) of opaque snow consisting of spherical grains and nonspherical grains, for different BC contents, and for snow grain radii of 100 μm and 1000 μm. Bottom: increase of spectral albedo if snow grains were nonspherical. The aspect ratio of the nonspherical snow grains is 1. Subscripts 'n' and 's' denote snow consisting of 'nonspheres' and 'spheres'; likewise in other figures.

3.3.2 Broadband Albedo

(a) Deep snow

For pure deep snow, the broadband albedo (α) of nonspherical grains is always larger than that of spherical grains (Figure 3.3), as the asymmetry factor of nonspherical grains is smaller. The enhancement of snow albedo increases as the snow grain size increases: the coarse-grained snow is more sensitive to the change of asymmetry factor. For each grain size, an equidimensional nonspherical grain (AR = 1, lowest asymmetry factor) shows the largest albedo increase. For snow with grain radii of 100 μm and 1000 μm, the albedo of equidimensional snow is higher by 0.032 and 0.050, respectively.

For both nonspherical and spherical snow grains, the albedo reduction caused by adding BC ($\Delta\alpha$) is shown in Figure 3.4. The reduction is smaller if the snowpack consists of nonspherical grains. For new snow (r = 100 μm) containing 100 ng/g BC, the albedo reduction is about 0.019 for spherical grains and 0.012 for nonspherical equidimensional grains, so that the difference in albedo reduction is 0.007 (Figure 3.4b). For old nonspherical (r = 1000 μm) equidimensional snow grains containing the same BC mass, the reduction is about 0.038 for spherical versus 0.056 for nonspherical grains, so that the difference in albedo reduction is 0.018 (Figure 3.4b). The difference in albedo reduction increases as BC mass increases until a maximum is reached, then starts to drop, and becomes insensitive to nonsphericity at large BC amounts as the albedo of snowpack approaches that of pure BC (Figure 9a in *Dang et al*. 2015). Therefore, the impact of nonsphericity may be different for different regions. For example, the typical BC mass fractions observed in snow are of the order of 10^{-8} in the Arctic (*Doherty et al.,* 2010) and North America (*Dang et al.,* 2013), and 10^{-7} in China (*Wang et al.,* 2013). In clean

regions like the Arctic, and most of North America, the BC concentration is low enough that the albedo reduction caused by BC is similar regardless of snow grain shapes. In highly polluted regions like China, the albedo reduction caused by BC is smaller if the snow grain shapes are nonspherical.

The impact of nonsphericity on snow albedo and albedo reduction caused by BC also depends on the SZA (Figure 3.5). For snow containing small amounts of BC, if we impose nonsphericity, the albedo enhancement (Figure 3.5a) and differences in the albedo reduction caused by BC (Figure 3.5b) increase as SZA decreases. This behavior is inverted at BC concentration > ~10^{-5}, but such high BC concentrations are rarely observed (*Bond et al.* 2013).

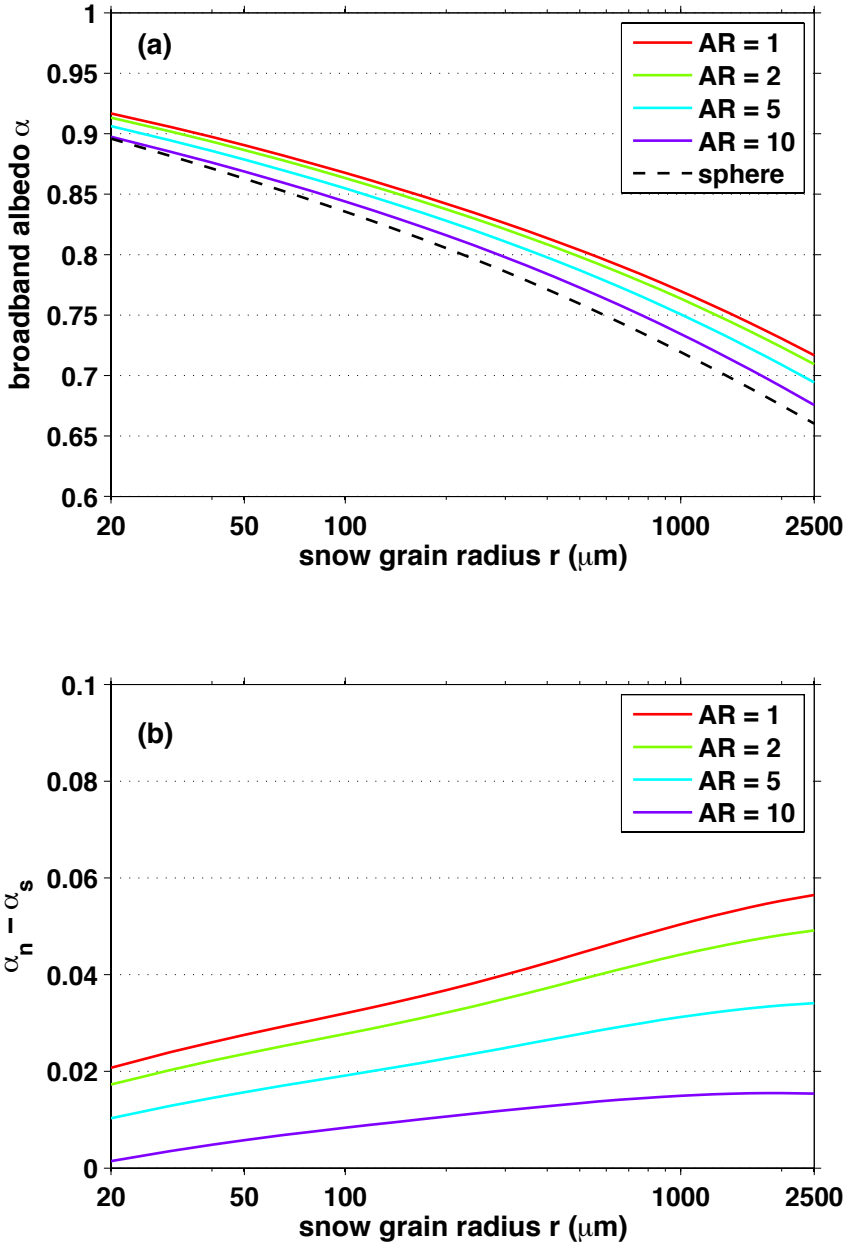

Figure 3.3. (a) Broadband albedo (α) of pure snow as a function of snow grain radius. Solid curves show nonspherical ice crystals with aspect ratios AR = 1, 2, 5, and 10. The dashed curve is for a snowpack with spherical snow grains. (b) Increase of pure-snow albedo caused by nonsphericity.

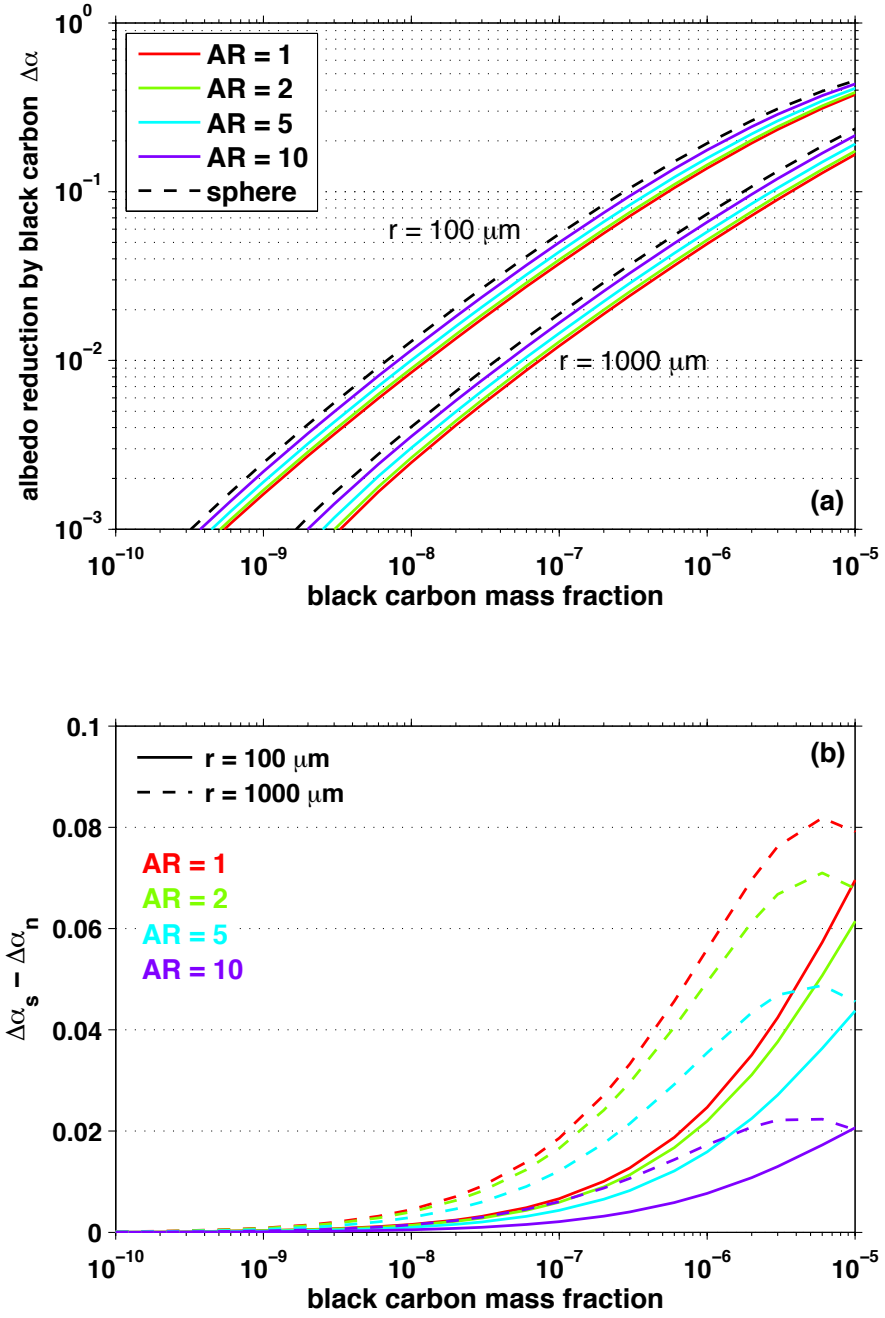

Figure 3.4. (a) Reduction of broadband albedo caused by BC (Δα), as a function of BC mass fraction. Δα for snowpacks of nonspherical or spherical snow grains is calculated relative to the pure snowpack with nonspherical or spherical snow grains, respectively. (b) The reduction of Δα if the snow grains were nonspherical.

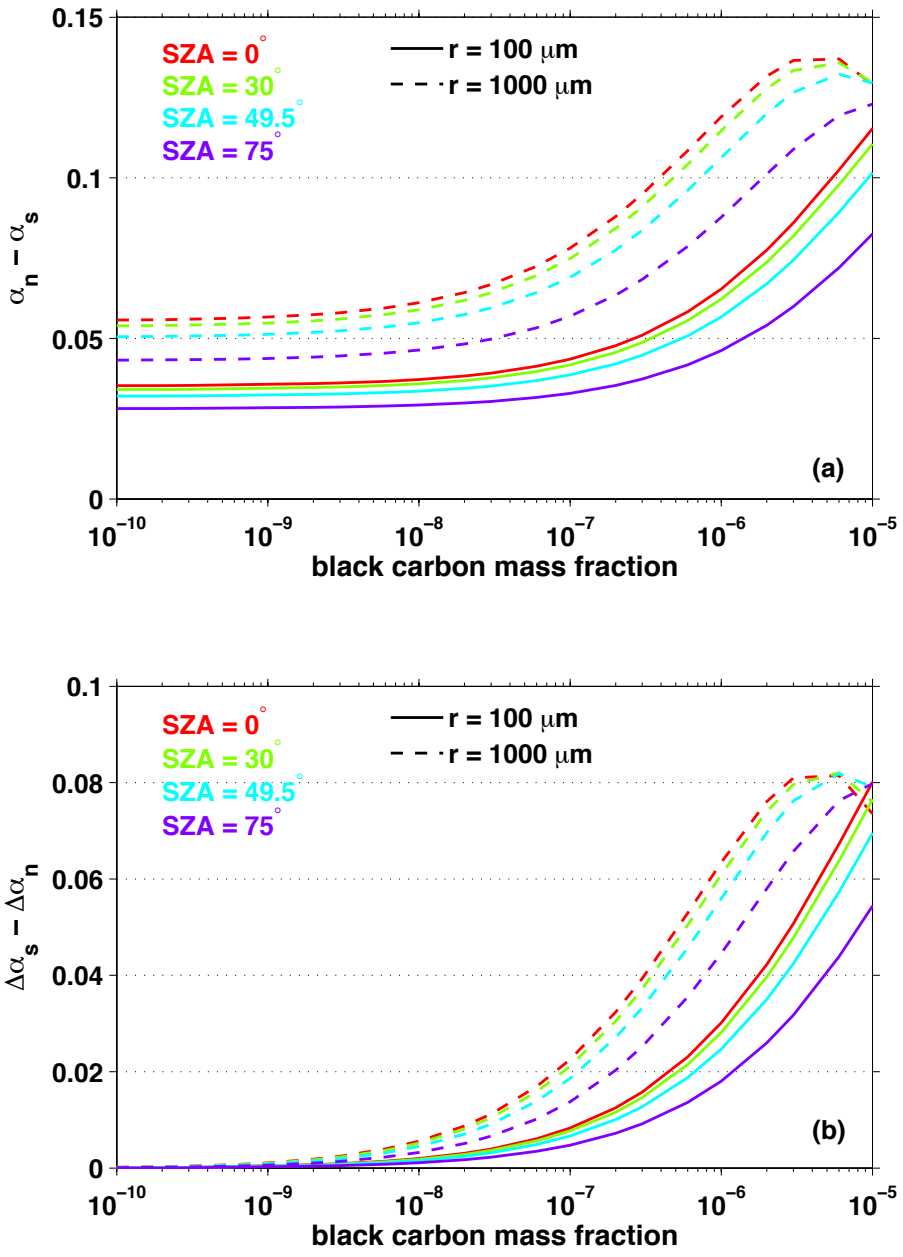

Figure 3.5. For different solar zenith angles (SZA) and BC mass fractions, the figure shows (a) the increase of broadband albedo (α), and (b) the change in albedo reduction caused by BC (Δα), if the snow grains were nonspherical. The aspect ratio of the nonspherical grains is 1.

(b) Shallow snow

The broadband albedo of shallow snowpacks is shown in Figure 3.6. The topmost curves are the overlap of three curves for new snow with different snow thicknesses (semi-infinite, 1 m and 0.3 cm), which illustrate that new snowpacks thicker than 3 cm are effectively semi-infinite. For old snow (r = 1000 μm), light penetrates deeper *(Wiscombe and Warren 1980),* and the albedo shows greater differences for different snow thicknesses. The albedo decreases as the snow thickness decreases, because light has a greater chance to penetrate through the snowpack and be absorbed by the underlying black surface. For snowpacks of the same thickness, the albedo is always higher at AR = 1 compared to other nonspherical cases. As we reduce the snow thickness, the albedo reduction is also smaller at AR = 1. Thus for shallow snowpacks of any thickness, a higher asymmetry factor yields a lower albedo.

The albedo of shallow snow containing BC is shown in Figure 3.7. Increasing mass fractions of BC cause even thin snowpacks to become opaque, until the albedo becomes independent of snow depth.

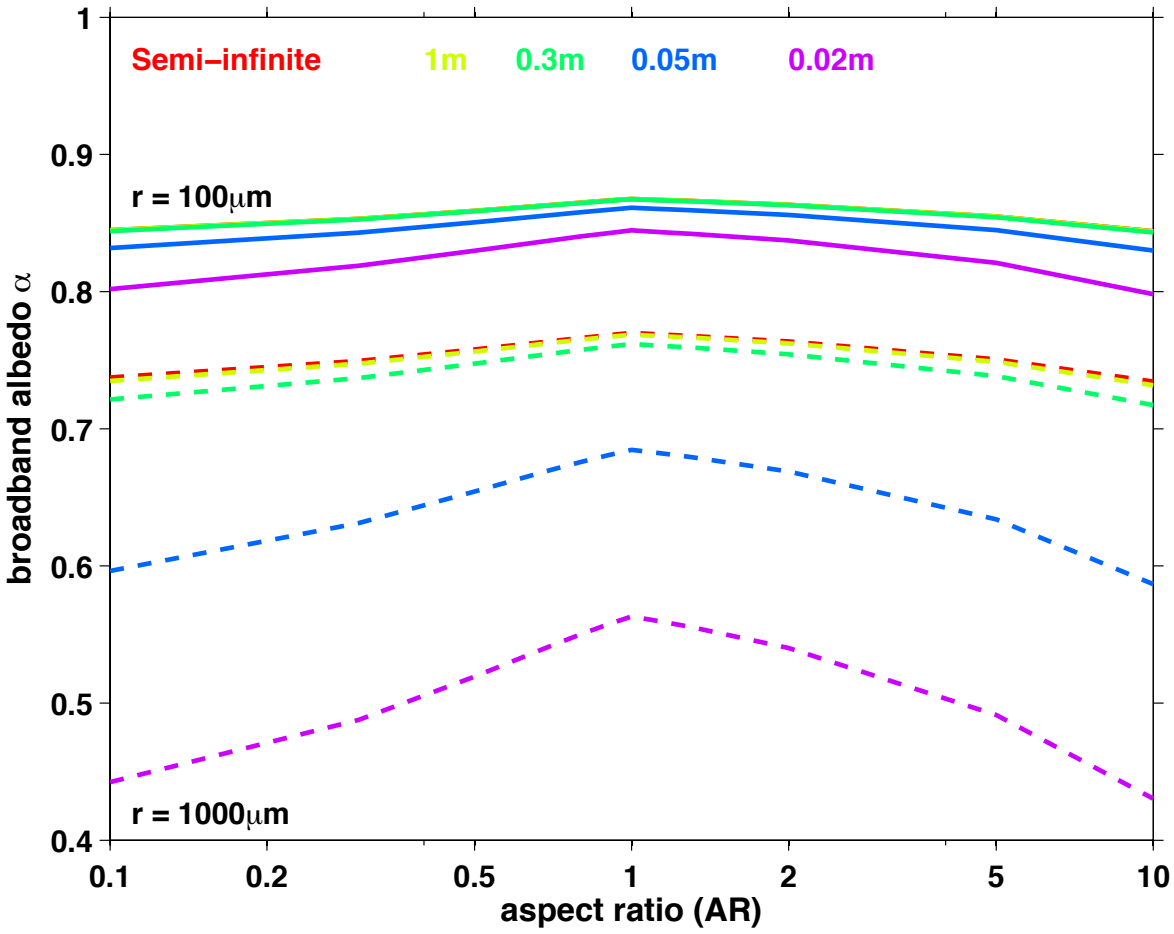

Figure 3.6. Broadband albedo (α) of pure nonspherical snow with different snow thicknesses, for snow grain radii of 100 μm (solid) and 1000 μm (dashed), as a function of ice crystal aspect ratio. The underlying surface is black (i.e. underlying surface albedo is zero). Snow density is 300 kg/m^3.

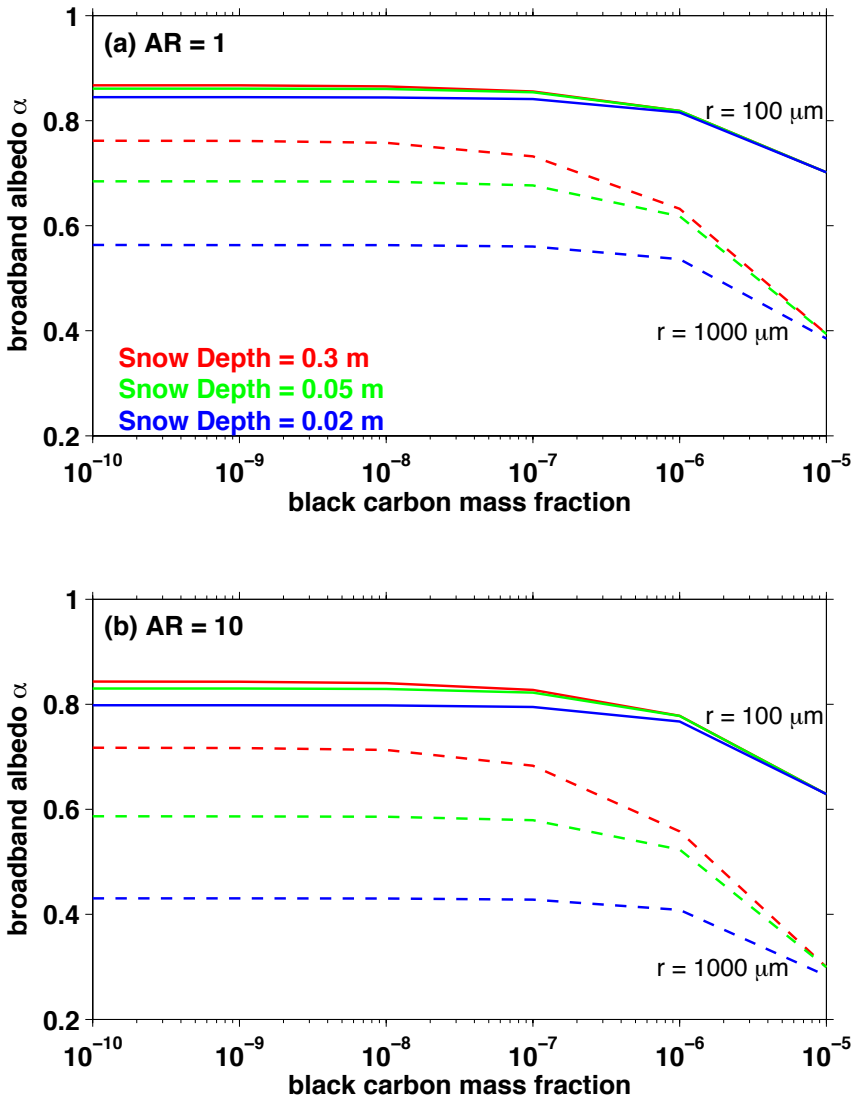

Figure 3.7. Broadband albedo (α) of thin snow containing BC, for snow grain radii 100 μm and 1000 μm, as a function of BC mass fraction. Top and bottom panels show results for snow grains with aspect ratio of 1 and 10 respectively, assuming the underlying surface is black (i.e. underlying surface albedo is zero). Snow density is 300 kg/m^3.

3.4. Comparison to measurements of spectral albedo

Given the significant effect of nonsphericity on albedo, we need to ask why radiative transfer models for snowpacks of spherical snow grains were able to match field measurements of spectral albedo with high accuracy (Figure 4 of *Grenfell et al.*, 1994; Figure 5 of *Brandt et al.*, 2011). The answer is that the grain radius r was a free parameter in the modeling. For a semi-infinite pure snowpack, the albedo is insensitive to g at visible and near-ultraviolet wavelengths because ice is essentially non-absorptive. At wavelengths where ice absorbs, the asymmetry factor g works together with the single-scattering coalbedo $(1-\varpi)$ to determine the albedo, and $(1-\varpi)$ is proportional to r (e.g., Equation 14 of *Warren et al.*, 2006). The grain radius was not measured independently in those field experiments; it was inferred by matching the model to the measurements. For example, as demonstrated in Figure 3.8, given a measured snow albedo of 0.59 at wavelength λ = 1.3 μm, modeling pure snow as composed of nonspherical grains with AR=1, a model would yield $r \approx 144$ μm versus $r \approx 60$ μm if the grains are modeled as spherical, corresponding to a scaling factor of 2.4. This scaling factor for grain radius would be different from 2.4 if the nonspherical grains have an aspect ratio different from AR = 1 (Figure 3.1).

For each aspect ratio and snow grain radius, we computed the scaling factor for 6 cases: thick and thin snowpacks (semi-infinite and 2cm), each containing 0 ng/g, 100 ng/g or 1000 ng/g of BC. The mean and standard deviation of the scaling factor for all six cases are shown in Figure 3.9a, for AR = 1, 2, 5, and 10, as a function of snow grain radius. At any given AR, the scaling factor is almost constant for $r > 200$ μm, regardless of snow depth and BC concentration. For $r < 200$ μm, the scaling factor increases with grain radius, and the variation with depth and BC is relatively larger but still negligible.

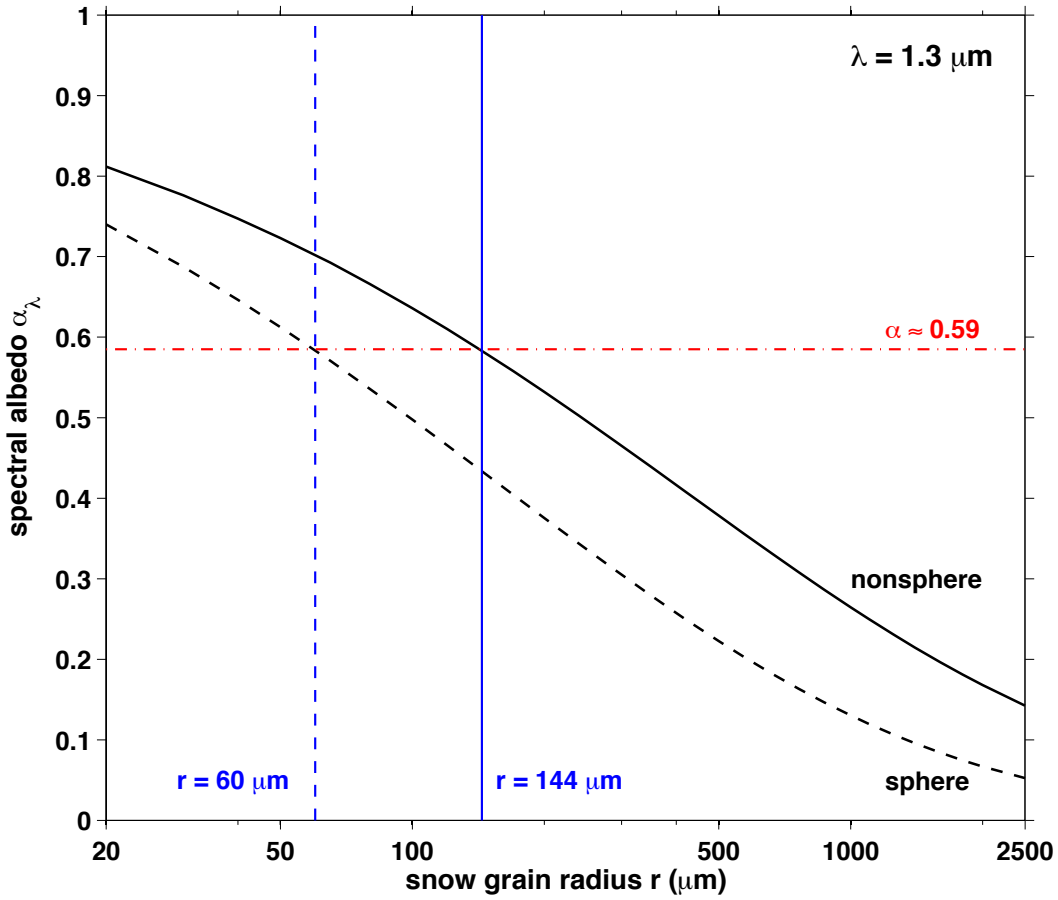

Figure 3.8. Spectral albedo (α_λ, λ = 1.3 μm) of semi-infinite snowpack with nonspherical (AR = 1) and spherical snow grains. A measured albedo of 0.59 would cause effective radius to be inferred as r = 60 μm or 144 μm depending on whether the grains are assumed to be spherical or not.

These results suggest that snow radii inferred from measurements of snow albedo can be scaled to obtain the effective radius of nonspherical grains (example shown in Figure 3.8). Conversely, if the specific surface area is measured in a snowpack (e.g. via methane absorption) and converted to effective radius via equation 1, this radius would need to be divided by the same scaling factor before computing snow albedo by means of Mie theory and

radiative transfer. For example, at any AR, if we use the mean scaling factor for r = 200 μm (Figure 3.9b) to scale the snow grain radii, and then calculate the snow albedo assuming spherical snow grains, the error in computed albedo is within ± 0.004 for a semi-infinite snowpack, or ± 0.006 for a 2-cm snowpack (supplementary Figure 1, Appendix B), when compared to the albedo of snowpacks composed of nonspherical snow grains with non-scaled radius. If we take into account the dependence of the scaling factor on grain radius (Figure 9a), this error is further reduced to ± 0.001 for all 6 cases (supplementary Figure 2, Appendix B). Of course, if the radiative transfer calculation has already employed the single-scattering properties of nonspherical ice crystals (e.g. *Jin et al.,* 2008*; Ottaviani et al.,* 2015), such an adjustment to the snow grain radius is unnecessary.

The mean scaling factor (Figure 3.9a) is fitted to a polynomial function of snow grain radius for each of 9 aspect ratios (supplementary Figure 3, Appendix B). The functions and coefficients are given in the supplementary Table 1 (Appendix B). Again, we remind the reader that the use and interpretation of a scaling factor for snow grain radius depends on the research focus. The scaling procedure has been tested only for albedo, not other radiative quantities. For example, it would not work to compute bidirectional reflectance, which has a much greater dependence on grain shape (*Xie et al.,* 2006).

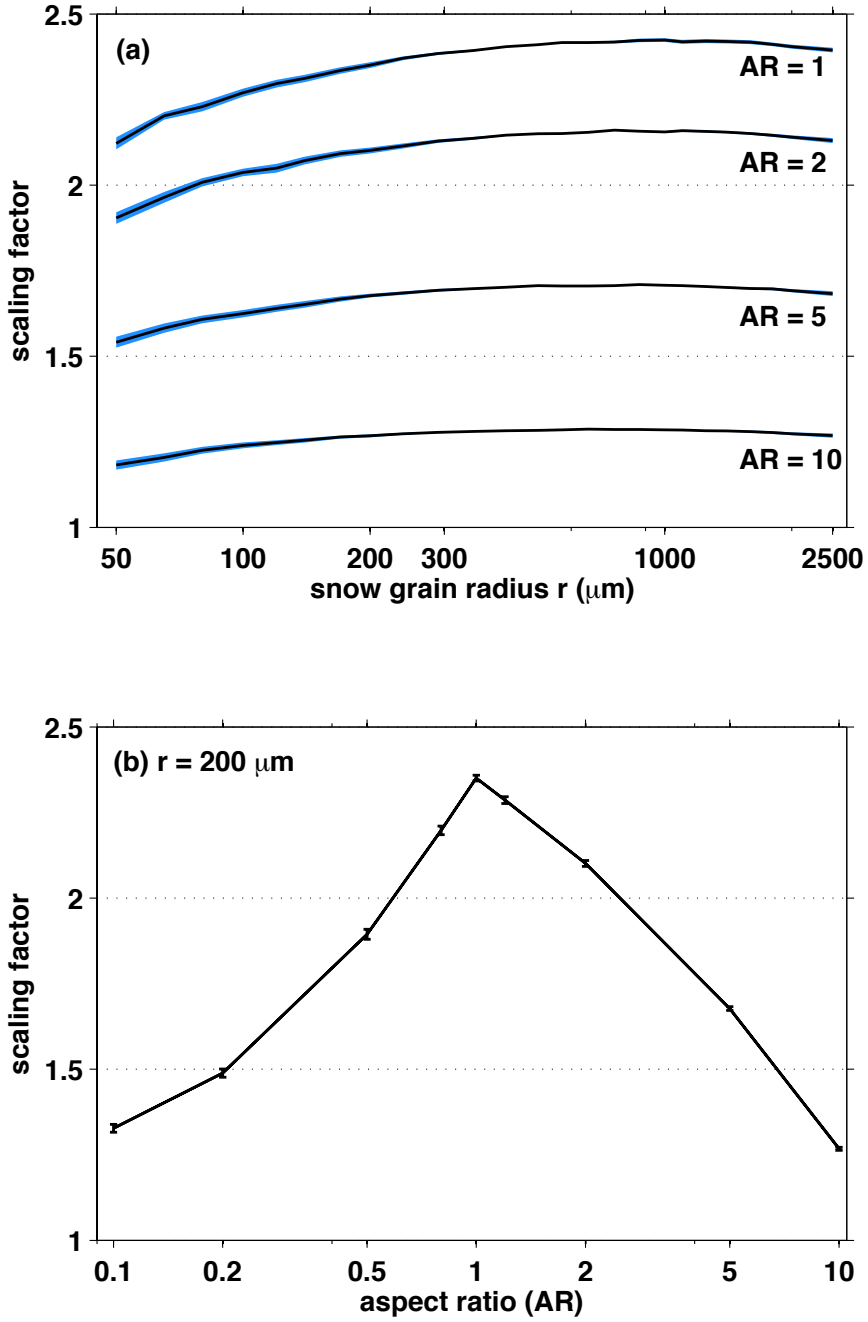

Figure 3.9. Scaling factors for different grain radii and aspect ratios, so that the spectral albedo computed by a model of spheres can match the spectrum of a snowpack of nonspherical grains. (a) Mean scaling factor of 6 cases for each AR (varying snow depth and BC content); blue shading shows ± one standard deviation. (b) Mean and standard deviation of scaling factor for snow grains with radius 200 μm.

3.5. Discussion and conclusions

In this work, we have calculated the albedo of snow for various snow grain sizes, snow depths, BC mass fractions, and for a range of aspect ratios of snow grains.

The asymmetry factor of snow grains is sensitive to the grain shape. At $\lambda = 0.5$ μm, g = 0.89 for spherical snow grains; while for nonspherical snow grains, it is a function of the particle aspect ratio, with the lowest value $g \sim 0.74$ at AR = 1. Though the sphere and equidimensional nonsphere both have AR = 1, their asymmetry factors are very different. For all aspect ratios between 0.1 and 10, the asymmetry factor of a nonspherical ice particle is always smaller than or equal to that of a sphere. Compared with the albedo of spherical grains, a snowpack of equidimensional nonspheres has higher albedo for all snow depths and BC mass fractions. For pure deep snow, the increases of snow albedo are 0.032 and 0.050 for new snow and old snow. For snow containing 100 ng/g BC, the increase of snow albedo is 0.039 for new snow and 0.069 for old snow. A smaller asymmetry factor results in a smaller albedo reduction caused by BC; 100 ng/g of BC can reduce the albedo of spherical new snow by 0.019, but only by 0.012 in the case of nonspherical snow. For larger grain sizes this difference is larger. The computed effect of BC may therefore be overestimated when using spherical grains in radiative transfer models, unless the grain size in the model is chosen to match the measurements of albedo.

In terms of climatological impacts, an increase of snow albedo due to nonsphericity will reduce the energy absorbed by snowpack. For a typical daily average solar irradiance of 400 W/m^2 in the Arctic late spring and early summer, an enhancement of broadband albedo of 0.01 will reduce the energy by 4 W/m^2 locally. This forcing will be different for different latitudes and times. Imposing an albedo reduction (for example, due to BC) for snow and ice

by 0.015 in the Arctic and 0.030 in the midlatitude northern hemisphere caused a hemispheric-average climate forcing of 0.3 W/m^2 (*Hansen and Nazarenko, 2004*). These amounts of albedo reduction would be smaller if we consider the nonsphericity of snow grains, unless these models chose the grain size to match the albedo measurements.

Radiative transfer models for snowpacks of spherical snow grains were able to match field measurements of spectral albedo to high accuracy by varying the snow grain radius in the model. In the same situation, snowpacks of nonspherical grains would imply smaller specific surface (larger effective radius) by a factor of up to 2.4.

As snow ages, the snow grains become more rounded and are often connected more or less to each other. The definition of a snow "grain" is therefore ambiguous, but the specific surface area (and therefore the corresponding "effective radius") is not ambiguous, because the specific surface area is just the area-to-mass ratio in bulk snow, and has a 1:1 relation to effective radius (equation 3.1). In climate models, it is hard if not impossible to predict the natural snow crystal shape for different snow age and meteorological conditions, let alone to assign different asymmetry factors to different snowpacks based on snow grain shape. To bridge this gap, more measurements on phase function of natural/artificial snowpack are needed. Such measurements (e.g. *Räisänen et al.,* 2015; *Ottaviani et al.,* 2015) are useful to evaluate the asymmetry factor used in current radiative transfer models, and also for their implications to the snow grain shape.

Acknowledgements

This research was supported by NSF grant AGS-11-18460. Q. Fu was supported by NASA grant NNX13AN49G.

Chapter 4

Measurements of light-absorbing particles in snow across the Arctic, North America, and China: effects on surface albedo

Cheng Dang[1], Stephen G. Warren[1], Qiang Fu[1], Sarah J. Doherty[1,2], and Matthew Sturm[3]

[1]Department of Atmospheric Sciences, University of Washington, Seattle, WA, USA.

[2]Joint Institute for the Study of Atmosphere and Ocean (JISAO), University of Washington, Seattle, WA, USA.

[3]Geophysical Institute, University of Alaska Fairbanks, Fairbanks, AK, USA.

In preparation for Journal of Geophysical Research: Atmospheres

4.0 Abstract

Large-area surveys on black carbon (BC) and other light-absorbing particles (LAPs) in snow have been carried out in the Arctic, China, and North America. Using the observational data

and a radiative transfer model, we compute the snow albedo and the albedo reduction induced by BC and all LAPs in snow, and quantify the impact of different variables (e.g. snow depth, cloud cover, vertical profiles of BC) on the albedo reduction induced by BC.

For new snow (effective grain radius of 100 μm) in the end of snow season (i.e. February and March for North Hemisphere middle and high latitudes respectively), the regional-averaged albedo reductions caused by all LAPs in the Arctic, North America, and China are 0.009, 0.013, and 0.082, respectively, of which the albedo reductions caused by BC alone are 0.005, 0.005, and 0.033, corresponding to a positive radiative forcing of 0.06, 0.3, and 3 Wm^{-2}. The BC-induced albedo reduction would be larger if snowpacks were all optically thick or did not contain non-BC LAPs (organic carbon and mineral dust). If snowpacks were optically thick, the albedo reduction would be 20-50% larger in the Arctic and North America. If the snowpacks did not contain non-BC LAPs, the albedo reduction by BC would increase by 33%, 29% and 72% in the Arctic, North America, and China. At 22 sites in subarctic Canada, the frequency distribution of snow depth was also measured; the impact of snow-depth distribution on albedo reduction by BC is negligible at these sites. The vertical profile of BC is important for calculating albedo reduction induced by BC in snow: a one-layer model with column-averaged BC concentration is inaccurate, but the albedo reduction derived from a two-layer model (top layer of 5 cm) agrees much better with that derived from the multi-layer model. By increasing or decreasing the observed BC concentration and snow depth by several factors, the relative and absolute changes in BC-in-snow albedo reduction are estimated. The same set of calculations are done for old melting snow (grain radius of 1000 μm); the albedo reductions are much greater than for fine-grained snow. Based on these results, we offer suggestions for future observations and model simulations of LAPs in snow.

4.1. Introduction

Over the past decade, our group and collaborators have carried out multiple large-area snow surveys in the mid-latitudes and high-latitudes of the Northern Hemisphere, specifically in the Arctic (*Doherty et al.,* 2010), Northern China (*Huang et al.,* 2011*; Wang et al.,* 2013), and North America *(Doherty et al.,* 2014; *Dang and Hegg,* 2014). The objective was to quantify the concentrations of light-absorbing particles (LAPs) in snow across these regions.

LAPs, by definition, absorb solar radiation. In contrast to sulfate aerosols, which cool the atmosphere and surface by reflecting incoming solar radiation or increasing cloud reflectivity (*Charlson et al.,* 1992), LAPs in the atmosphere absorb solar radiation and heat the absorbing aerosol layer. Depending on the vertical profile of LAPs, the imposed heating may evaporate clouds, enhance or suppress vertical motions, and change the climate dynamics (*Koch and Del Genio,* 2010). These LAPs can be removed from the atmosphere by dry and/or wet deposition (*Bond and Bergstrom,* 2006). After LAPs are deposited on bright surfaces like snow, they reduce the albedo (*Warren and Wiscombe,* 1980).

One of the major LAPs in snow is black carbon (BC). BC is a unique carbonaceous aerosol that absorbs strongly across the ultraviolet (UV) and visible wavelength bands (*Bond et al.,* 2013); a small amount of BC can reduce snow albedo significantly because ice itself is almost non-absorbing at these wavelengths (*Warren and Wiscombe,* 1980). BC results from incomplete combustion; its dominant emitters vary by location. Globally, about 60% of BC is emitted from energy-related combustion and the rest from biomass burning (*Bond et al.,* 2013). A large fraction of BC is emitted from anthropogenic sources and it has a high mass-absorption coefficient. Because of this, BC is recognized as an important forcer for regional and global climate. The impact of BC on snow was first highlighted by *Warren and Wiscombe* (1980; 1985),

and it was later incorporated into climate models by *Hansen and Nazarenko* (2004), who estimated the radiative forcing in the Northern Hemisphere. In a recent assessment, the globally-averaged BC-in-snow effective forcing (i.e. including rapid adjustments) is estimated to be 0.1 W/m^2 (*Bond et al.,* 2013).

Besides BC, there are other types of light-absorbing particles in snow, most notably organic carbon (OC) and mineral dust (MD) (*Moosmüller et al.,* 2009; *Bond et al.,* 2004; *Kirchstetter et al.,* 2004). At the regional scale, especially in areas downwind of desert and semiarid regions, MD can dominate the light-absorption by LAPs, for example, in Colorado (*Painter et al.,* 2007), Inner Mongolia (*Wang et al.,* 2013), and Japan (*Aoki et al.,* 2006). So-called brown carbon (BrC), here referred to as OC, is co-emitted with BC from combustion sources; some OC are also generated from soil (humic-like substances, *Dang and Hegg,* 2014), plants, and other natural non-combustion sources. The contribution of OC to snow-albedo reduction is smaller but also significant; In this work, we will refer to OC and MD as non-BC LAPs collectively.

Given the potentially significant impact of LAPs on snow albedo, many model simulations have been done to estimate the climate forcing induced by BC in snow, and some on the impact of non-BC LAPs. These modeling works either (1) prescribe fixed snow-albedo reductions across large areas in different regions (*Hansen and Nazarenko,* 2004) or (2) simulate the BC deposition in snow and calculate their induced albedo reductions (*Jacobson et al.,* 2004; *Flanner et al.,* 2007; 2009; *Zhao et al.,* 2014; *Namazi et al.* 2015). However, the complex nature of LAPs (diverse emission sources, chemical species, and transport scales) add difficulty and uncertainty to model simulations of LAP concentrations (*Moosmüller et al.,* 2009; *Bond et al.,*

2013). The aforementioned field campaigns are thus useful observational datasets on light-absorbing particles in snow across these areas.

During the field campaigns, the snow samples were collected, processed, and measured using the same techniques; the major outputs are snow depth, BC concentration, and fractional absorption by non-BC LAPs. Vertical profiles of LAPs were obtained at most of these sites. These data are publicly available for scientific studies (http://www.atmos.washington.edu/articles/BC_LAP_Snow_FieldData/). So far, the major application has been model evaluations.

In the Arctic, compared with the results from *Doherty et al.* (2010), the modeled BC in snow by *Koch et al.* (2009) is generally lower by a factor of 0.3-1; the modeled BC mixing ratio by *Flanner et al.* (2009) was lower in some locations and higher in others, differing from the observations by factors of 0.6 to 3.4. These results, as well as the results of other measurement/model comparisons in the Arctic are summarized in Table 21 of *Bond et al.* (2013). In China, comparing with the observations (*Wang et al.,* 2013), *Zhao et al*. (2014) found that WRF-Chem (Weather Research and Forecasting model coupled with Chemistry) underestimates the surface-layer BC in the clean regions but significantly overestimates it in polluted regions. In North America, *Zhang et al.* (2015) pointed out that CAM5 (Community Atmosphere Model) has a significant low-bias in the predicted mixing ratio of BC in snow. *Namazi et al.* (2015) simulated the BC-in snow mixing ratio using CanAm (Canadian Atmospheric Global Climate Model), concluding that the model agrees with observations within an order of magnitude across the Northern Hemisphere. Almost all these validations focused on BC, some on MD, and only one on OC.

In general, the modeled BC agrees with observations within an order of magnitude. Constrained by the temporal and spatial resolutions of model simulations, most of these comparisons suffer from mismatches in time and/or locations, complicating interpretation of these comparisons (*Qian et al.,* 2015). Depending on the research purpose, the impact of such uncertainty on modeling results can be either major or minor. For model simulations aiming for a better evaluation of radiative forcing induced by LAPs in snow, comparison with the measured BC concentration is just the first step. For a given BC concentration the simulated BC-induced radiative forcing might also be affected by other factors and processes.

First, the direct albedo reduction caused by LAPs in snow is influenced by factors other than LAP concentration, such as snow depth, snow grain size and shape, and cloud cover (*Warren and Wiscombe,* 1980; *Aoki et al.,* 2011; *Dang et al.,* 2015; 2016). Incorrect simulation of these factors can yield errors in snow albedo similar to or greater than the albedo reduction caused by LAPs. Model validation should include these factors as well. Second, the impact of these factors on the direct LAP-in-snow albedo reduction varies depending on the LAP concentration. For example, 10 ng/g BC can reduce the broadband albedo of new snow and old snow (snow grain radius of 100 and 1000 microns) by 0.004 and 0.01 respectively; the difference in albedo reduction between these snow types and BC concentration is 0.006. For the same snowpack, but containing 100 ng/g BC, the difference in albedo reduction between old and new snow would be much larger, 0.04 (*Dang et al.,* 2015). Thus, a given bias in BC mixing ratio does not scale by a fixed amount to a bias in albedo reduction. The bias/uncertainty in these factors will produce bias/uncertainties in the direct albedo reduction caused by BC and therefore the direct forcing induced by BC.

Besides the direct forcing, a large fraction of LAP-in-snow forcing results from feedback processes involving both snow metamorphism and atmosphere-snow interactions (*Flanner et al.,* 2007; *Bond et al.,* 2013). For example, as snow starts to melt, LAPs tend to accumulate at the surface: this further enhances albedo reduction, accelerating snowmelt - a positive feedback process (*Doherty et al.,* 2013). Such feedback processes cannot be quantified by current observational data, but they are triggered by the direct albedo reduction caused by LAPs in snow; thus it is crucial to have an accurate estimate of the initial direct albedo reduction in order to calculate both LAP-in-snow direct radiative forcing and adjusted radiative forcing via feedbacks.

In this work, we use observational data from field campaigns to derive the direct albedo reduction caused by LAPs in snow with a focus on BC, quantifying the impact of various factors on albedo reduction. The results will also provide insight on to what factors should be considered when testing modeled direct forcing by LAPs in snow, and what processes must be included in models for accurate calculations of radiative forcing.

4.2. Data and Methods

4.2.1 Field observations

4.2.1.1. Large-area field campaigns on LAPs in snow

As stated in the introduction, our group and collaborators have carried out several large-area field campaigns in the Arctic, China, and North America. The Arctic survey expanded the first survey carried out by Clarke and Noone in 1983-1984 (*Clarke and Noone,* 1985), and reported the concentration of LAPs in snow from fieldwork done in 1998 and the years 2005-2009 across a much larger region in the Arctic including the Arctic Ocean, Greenland,

subarctic Canada, and Siberia. (*Doherty et al.,* 2010). Later in January and February of 2010, a similar large-area survey was conduced to study the snow in Northeastern China *(Huang et al.,* 2011; *Wang et al.,* 2013*).* This was the first large-area survey on LAPs in snow conducted in the mid-latitude Northern Hemisphere. The same research team then carried out a similar field campaign two years later to sample snow in Northwestern China (*Ye et al.,* 2012). In the winter of 2013, the first large-area field campaign on LAPs in snow in North America was conducted across 13 states in the US and 3 provinces in Canada. In the winter of 2014, long-term observations at three fixed sampling locations in Idaho (*Doherty et al.,* 2016) were also added. In this work, we will focus only on the large-area surveys reported by the following three papers: *Doherty et al.,* 2010, *Wang et al.,* 2013*,* and *Doherty et al.,* 2014, for the Artic, China, and North America respectively.

The snow samples were mostly collected in late winter or early spring when the snowpack was near its maximum depth, before the snow started to melt. Sampling locations were far from major roads and populated areas to avoid local contamination. The snowpacks at these sampling sites can usually represent the snow in surrounding areas. At each sampling site a snowpit was dug and two vertical profiles obtained: snow samples were collected for multiple layers depending on the snow stratigraphy. The collected snow samples were then melted and passed through filters. Filters loaded with particles from the snow were measured using a spectrophotometer to estimate the concentration of BC and non-BC LAPs in the snow. The detailed procedures on snow collection and filtration can be found in *Doherty et al.,* (2010), and the description of photometer and optical methods can be found in *Grenfell et al.,* (2011). In this work, we will mainly use the following data profiles acquired from these field expeditions:

(a) Snow depth [cm].

(b) Snow density [kg/m3] profile.

(c) C_{LAP} [ng/g] profile: equivalent amount of BC if all light absorption by particles in snow were due to BC.

(d) C_{BC} [ng/g] profile: estimated concentration of BC in snow.

(e) C_{NBC} [ng/g] profile: equivalent amount of BC that would be needed to explain the absorption by non-BC LAPs. $C_{NBC} = C_{LAP} - C_{BC}$.

Using this optical technique, absorption by LAPs and non-BC LAPs are converted into the equivalent mass of BC that would be needed to produce the same amount of absorption (*Grenfell et al.,* 2011). Therefore, although we do not know the concentration and optical properties of non-BC LAPs, we can still derive their impact on snow albedo as long as we know the optical properties of BC. This allows us to calculate snow albedo reductions due to both BC and non-BC constituents, as described in section 4.2.3.1.

The snow depth and BC concentration in the top 5 cm snow layer at all sampling sites are shown in Figure 4.1. In the Arctic and North America, snow is deeper and contains lower concentrations of BC, while in China, the snow is shallower and contains larger concentrations of BC. In Figure 4.2 we show the regional variations of these two quantities for the three regions indicated by dashed lines in Figure 4.2. For the Arctic, North America and China, the mean snow depths are 38, 26, and 14 cm, respectively, and the mean BC concentrations of surface layer are 27, 29, and 756 ng/g respectively. The range of BC mixing ratios in China is large.

2.1.2 Snow depth distribution in sub-arctic Canada

In Figure 4.1, 22 snow sampling sites in sub-arctic Canada are grouped and boxed by a solid line. Snow samples at these sites were collected during April of 2007 as part of a snow survey (*Sturm et al.,* 2008). In addition to collecting snow samples at a given location, they also measured the snow-depth distribution in the surrounding area. At each sampling location, up to 600 distributed snow depths were reported (see Appendix B of *Sturm et al.,* 2008). We do not have snow-depth distributions in other regions, so we will use this unique dataset to illustrate the impact of depth distribution on snow albedo, following the methods described in section 4.2.3.2.

4.2.2 Albedo calculation

4.2.2.1. Single-scattering properties of ice and BC

The single-scattering properties of ice and BC are calculated using Mie theory with optical constants of ice from *Warren and Brandt* (2008) and optical constants of BC from *Bond and Bergstrom* (2006). We assume the snow grains are spherical with radii of either 100 μm or 1000 μm, which correspond to the typical effective grain radii of new snow and old melting snow, respectively (*Wiscombe and Warren,* 1980). The effects of snow grain shape on snow albedo including the albedo reduction by BC have been examined by *Dang et al.* (2016). They found that these effects can be mimicked by using a smaller grain of spherical shape. For snowpacks containing BC, we assume that BC particles and ice particles are externally mixed, i.e. the single-scattering properties of snowpacks are the area-weighted sum of the single-scattering properties of BC and ice separately (*Dang et al.,* 2015).

4.2.2.2. Spectral albedo

The single-scattering quantities of snow are put into a radiative transfer model to calculate the spectral albedo, $\alpha\lambda$, of snowpacks using the discrete ordinates method (DISORT, *Stamnes et al.,* 1988) for wavelengths of 0.2 to 4 μm. For all calculations, we use a solar zenith angle of 49.5° with a cosine of 0.65. This is the effective solar zenith cosine for diffuse radiation under a cloud; it is close to the insolation-weighted solar zenith cosine for the sunlit hemisphere (0.66); and it may also allow us to estimate the albedo of other solar zenith angles by altering the effective snow grain radius (*Marshall,* 1989), as discussed by *Dang et al.* (2015).

For an optically thin snowpack, the albedo of the underlying ground is also important because the ground can absorb light that penetrates through the snowpack. The albedo of the underlying ground depends on the location and sampling time. As shown in Figure 4.3, in the mid-latitude regions we sampled, the underlying ground for most snow-sampling locations is short grass. In subarctic Canada and Russia, the underlying ground is usually tundra or damp soil. In Greenland and on the Arctic Ocean, what is beneath snow is ice sheet and sea ice respectively. Based on the location of the snow sampling sites we use the spectral albedo of different surface types, as shown in Figure 4.4. These data were measured by different groups (*Liang et al.,* 2002; *Brandt et al.,* 2005; *Bøggild et al.,* 2010) and then extrapolated to 0.3 to 4 μm for computational use. For each snow sampling site, we use the appropriate ground albedo for the radiative transfer calculation: China and North America (grassland), subarctic and arctic Canada and Russia (damp soil), and Arctic Ocean (1st year sea ice); for Greenland, there is no need to specify the underlying surface because the snow depth on the ice sheet is effectively semi-infinite.

Snow grain size was also estimated visually with a magnifying glass in many of the snow pits. However, we do not use those grain sizes in our calculations because our aim is not to compute the albedo at the exact moment of sampling. The grain sizes we find at the surface are the result of temperature and time since snowfall and can be altered by wind, so we do not take them to be representative of that location over a month or season. Instead, we perform albedo computations for two idealized snow grain sizes representing fine-grained new snow and coarse-grained old melting snow, which effectively are bounding limits. Thus although the snow was sampled before melting began (snow grain size likely closer to 100 μm), we also compute what the albedo will be at that location when the snow is melting later in the spring (snow grain size likely closer to 1000 μm).

4.2.2.3. Broadband albedo

The spectral albedo, αλ, of snowpacks is integrated over the solar spectrum (λ = 0.3 to 4 μm) and weighted by the incoming solar irradiance S(λ) to calculate broadband albedo α.

$$\alpha = \frac{\int \alpha_\lambda S(\lambda) d\lambda}{\int S(\lambda) d\lambda} \tag{E4.1}$$

For snow sampling sites in the Arctic, we use the incoming solar spectra measured at the Arctic sea surface by *Grenfell and Perovich* (2008). For snow sampling sites in China and North America, we use the same downwelling solar irradiance spectra in mid-latitude used by *Wang et al.* (2013). Solar spectra for both clear sky and cloudy sky are available, which allow us to calculate the albedo of snowpacks for both clear sky and cloudy sky cases. The all-sky albedo is the weighted average of clear-sky albedo and cloudy-sky albedo, depending on the cloud fraction (CF, %, as shown in Figure 4.5):

$$\alpha_{all\ sky} = SF * \alpha_{cloudy\ sky} + (1 - SF) * \alpha_{clear\ sky} \quad \text{(E4.2)}$$

In mid-latitudes, depending on the specific location, snow starts to melt between mid-February and mid-March, so to calculate the all-sky albedo of snowpacks in this region, we apply cloud fraction of February for new snow (r = 100 μm) and of March for old-melting snow (r = 1000 μm). At higher latitudes, snow starts to melt later; we therefore use the cloud fraction of March for new snow (r = 100 μm) and of April for old-melting snow (r = 1000 μm) to calculate the all-sky albedo of snowpacks in this region. If not noted otherwise, the albedos given in this paper are all-sky broadband albedo calculated using the cloud fraction shown in Figure 4.5.

4.2.2.4 BC-in-snow radiative forcing

Direct radiative forcing by BC in snow is estimated by multiplying the derived albedo reduction by the downward shortwave flux at surface. As shown in Figure 4.5, both solar flux and cloud fraction are acquired from the CERES (Clouds and the Earth"s Radiant Energy System, *Wielicki et al.,* 1996) product "CERES SYN1deg" (https://ceres.larc.nasa.gov/products.php?product=SYN1deg). The downloaded 3-hour data are first averaged over 10 years from 2005 to 2014, then averaged over three separate regions defined in Figure 4.1. As was done for the calculation of all-sky albedo, we use fluxes of different months for mid-latitudes and high-latitudes as well.

4.2.3 Computation scenarios

Combining observational datasets with a radiative transfer model enables us to calculate snow albedos for different scenarios to (1) quantify the albedo reduction by light-absorbing particles and to (2) explore the impact of different factors on derived albedo reduction by BC.

4.2.3.1 LAPs

Using observed snow depth and snow density profile, we can calculate the albedo of snowpacks containing different types of LAPs, specifically for the following four scenarios:

a) Pure: snow does not contain any LAPs;

b) BC: snow contains only BC, with concentration C_{BC};

c) nonBC: snow contains only non-BC LAPs (here we use snow containing the "equivalent" BC, with concentration C_{NBC});

d) LAPs: snow contains both BC and non-BC LAPs (we use the concentration C_{LAP}; the albedo calculated in this scenario reflects the total LAP composition of the sampled snowpack).

By taking the differences in snow albedo between pure snow and snow containing different LAPs, we can derive the albedo reduction by different types of LAPs. The results are discussed in Section 4.3.1.

4.2.3.2 Vertical profiles

In the field, snow samples were collected from layers from the top to the bottom of snowpack, so we have vertically-resolved concentrations of BC and non-BC LAPs. The number of layers varies depending on snow depth and stratigraphy; the number of layers sampled was typically 5; the maximum was 24, in Greenland. In this work, we therefore use

a multi-layer radiative transfer model to compute the albedo of snowpacks with no restraint to the number of layers. However, this may not be an option for climate models. To examine the impact of vertical profiles on snow albedo and albedo reduction by BC, we compute the snow albedo for the following four scenarios:

a) Multi-layer: multi-layer snowpacks. Snow density and concentration of LAPs are vertically resolved based on field observations. The albedo from in this scenario is used as the reference calculation for the sampled snowpacks (given the specified grain size).

b) One-layer (column-mean BC): one-layer snowpack. Snow density and concentrations of LAPs are the vertically weighted average of the entire snowpack, based on the profiles from field observations.

c) One-layer (top 5-cm mean BC): one-layer snowpack. Snow density and concentrations of LAPs are the values measured in the top 5-cm of snowpacks, based on the profiles from field observations. For this case, the column-integrated BC concentration is different from observations.

d) Two-layer: two-layer snowpack. The top layer is 5 cm and the sub-surface layer is the entire snow column below the top 5 cm. Snow density and concentrations of LAPs in these two layers are the vertically-weighted average of samples from the top 5 cm and lower layers, respectively.

The results are discussed in Section 4.3.2.

4.2.3.3 Sensitivity tests on BC concentration and snow depth

As discussed in the introduction, model-simulated BC concentrations agree with observations only to within a factor of 10. In addition, model simulation of snow depth is

also subject to large uncertainty. For a given snow grain radius, the albedo reduction by BC is mostly determined by the amount of BC and the snow depth (if snow is thin). Therefore, it is important to evaluate the uncertainty/bias in BC-in-snow albedo reduction caused by the uncertainty/bias in both BC concentration and snow depth. For these sensitivity tests, we decrease/increase the observed BC concentration and snow depth by dividing/multiplying by factors of 2, 5, and 10, and evaluate the changes in computed BC-in-snow albedo reduction. For the adjusted snow depth that is shallower than what is observed, we only consider the top snow layers within the adjusted snow depth. For example, if the sample snowpack is 20 cm deep, the adjusted snow depth is 4 cm if we divide the original depth by a factor of 5; in this case, we remove the bottom 16 cm of snow and calculate the snow albedo as if snow were only 4 cm deep. For the adjusted snow depth that is deeper than what is observed, we extend the bottom layer to match the target depth, with same black carbon concentration. To evaluate the maximum potential impact of BC-in-snow, we also included one more case by setting the snow depth to 100 m (optically deep snow). The albedo calculated in this scenario will illustrate the change in BC on snow albedo if all sampling snowpacks were optically semi-infinite. For the sensitivity tests, the snow-column integrated black carbon mass differs from the observed values. The results are discussed in Section 4.3.3.

4.2.3.4 Snow depth distribution

Using field data described in 2.1.2, we will show the impact of snow-depth distribution on snow albedo and BC-in-snow albedo reduction. At each sampling site, albedo and albedo reduction by BC is calculated both for the mean snow depth and for a distribution of snow depths from the field measurements in subarctic Canada. In our calculation, the

concentration of light-absorbing particles and snow density are the same for each of the numerous depth-measurements made at the site. The resulting difference in snow albedo or albedo reduction by BC is therefore only due to depth distribution. These results are discussed in Section 4.3.4.

In the result section, we will derive and discuss the following quantities:

a) α: all-sky broadband albedo of snowpacks.

b) $\Delta\alpha$: reduction of α induced by different LAPs in snow.

c) $\delta\alpha$ and $\delta\Delta\alpha$: change in α or $\Delta\alpha$ if snow conditions, LAPs concentrations, or model setup change.

4.3. Results

4.3.1 Snow albedo and albedo reduction induced by BC

Albedos of snowpacks containing different types of LAPs are shown in Figure 4.6. The regional means are given in Table 4.1. The regional variation of snow albedo in China is much larger than that in the Arctic and North America. The climate model simulations for snow albedo in China therefore should use a finer geographical resolution.

Albedo reduction by BC, non-BC LAPs, and total LAPs are shown in Figure 4.7. For new snow containing BC only, the albedo reduction caused by BC is 0.006, 0.007, and 0.057 in the Arctic, North America, and China respectively. For snow containing non-BC LAPs only, the albedo reduction caused by non-BC LAPs is slightly smaller than the albedo reduction caused by BC but of the same order of magnitude. The albedo reduction caused by all LAPs are 0.009, 0.013, and 0.082 in the Arctic, North America and China. These

values are smaller than the sum of albedo reductions caused by BC and non-BC LAPs separately. This is because the penetration depth of light decreases as the concentration of LAPs increases, so albedo reduction does not increase linearly with the addition of LAPs..

There are significant amounts of non-BC LAPs emitted from natural sources (e.g. desert dust), and these are present in snow regardless of human activities, in some locations in high concentrations. Thus, natural snowpacks are not pure, and baseline calculations of the albedo of non-polluted snow for radiative forcing calculations must account for this. To evaluate the impact of anthropogenic BC on snow albedo, or to quantify the radiative forcing induced by BC, we need to study the impact of BC on snowpacks that already contain natural, non-BC LAPs. If snow already contains the observed amounts of non-BC LAPs, the albedo reduction caused by BC is 0.005, 0.005, 0.033 in the Arctic, North America, and China; these albedo reductions would increase by at least 20% if the snow did not contain non-BC LAPs. The impacts of LAPs on snow albedo in different scenarios are much larger for old melting snow (r = 1000 μm); this is because shortwave radiation penetrates deeper in coarse-grained snow and encounters more of the LAPs. These regional averaged data are illustrated in Figure 4.7 and also listed in Table 4.1.

The BC-in-snow albedo reduction and direct radiative forcing are derived and shown in Figure 4.8 (for new snow only) and in Figure 4.9. Note that this forcing does not include any feedbacks, e.g. to snow grain size or snowmelt, so will be smaller than if they did include these feedbacks, as in some previous forcing calculations (e.g. *Flanner et al.,* 2009; *Bond et al.,* 2013). In the Arctic and North America, the albedo reductions caused by BC are similar: 0.005 and 0.009 for new snow and old snow, respectively, in both regions. Despite the similar albedo reduction, the radiative forcing by BC in snow in North America is much

larger because the solar insolation is much larger at mid-latitudes than at high latitudes (Figure 4.5). The albedo reduction caused by BC in China is considerably larger than in the other two regions: 0.03 and 0.06 for new snow and old snow. For new snow, the direct radiative forcing by BC is 0.05, 0.3, and 3 Wm^{-2} in the Arctic, North America, and China respectively. For old snow, the direct forcing is much larger: 0.5, 0.9, and 8 Wm^{-2}, respectively. This radiative forcing includes all BC measured in the snowpack, but it is unclear whether all BC is emitted from anthropogenic sources.

4.3.2 Impact of vertical profiles on albedo reduction by BC

Figure 4.10 shows the derived BC-in-snow albedo reduction from radiative transfer calculations using the different vertical profiles described in section 4.2.3.2. The results of one-layer and two-layer models are compared against the results of the multi-layer model. From the top panels of Figure 4.10, we can see that albedo reductions derived from the one-layer model with column-mean BC are not accurate. Depending on the concentration of BC in the top layers of snowpacks, this one-layer model either overestimates or underestimates the albedo reduction by BC. Since most light scattering and absorbing processes occur in the surface layer of snowpacks, if we apply the BC concentration of the surface layer (top 5 cm) to the entire snow column, this one-layer model agrees rather well with the multi-layer model (middle panels of Figure 4.10). If we use a two-layer model that accounts for BC in the lower layer, the error in albedo reduction is further reduced, especially for the Arctic and North America (bottom panels of Figure 4.10). Given these different vertical profiles of snowpack, the resulting albedo reductions in the Arctic are similar. In China, the concentrations of LAPs are very high, so light does not penetrate as deeply; the relative impact of BC profiles on derived albedo reduction is therefore smaller. In North America,

the albedo reduction is more sensitive to the profiles of BC concentrations. Overall, a correct concentration of LAPs in the top 5 cm is crucial for determining albedo reductions for all three regions.

4.3.3 Sensitivity tests

As discussed in Section 4.3.1, the albedo reduction caused by BC is smaller if the baseline snowpack contains non-BC LAPs than if the baseline snowpack is clean. There are other factors that also influence BC-in-snow albedo reduction. In Figure 4.11, we show the relative and absolute changes in albedo reduction for different snow conditions, cloud cover, and snow depths, and for a range of BC concentrations. Data shown in this figure are summarized in Table 4.2. The percentages discussed in this section are relative changes of albedo reduction induced by BC (grey-shaded column in Table 4.2).

We first consider the case of new snow with observed BC concentrations. If the snowpack is optically thick and it does not contains non-BC LAPs in addition to the BC (x-label case "deep, BC", BC is short for "BC only"), the albedo reduction by BC increases in all three regions by a factor of 1-2 for new snow (and by a factor of 2-6 for old melting snow) relative to the case where observed snow depth is used. Similarly, the albedo reduction by BC also increases if snow depth is optically thick (x-label case "deep") or if the snow depth is as-observed but does not contain non-BC LAPs (x-label case "BC only"). In the Arctic and North America, if the snow were optically thick, the albedo reduction induced by BC would increase by 20-50%. If non-BC LAPs were not present in the snowpack, the albedo reduction induced by BC would increase by ~30% in the Arctic and North America, and by 70% in China. The relative change is larger for old snow than for new snow (lower panels in Figure 4.11).

The spectral solar irradiance under cloudy sky is richer in visible wavelengths because clouds filter out the near-IR wavelengths. The broadband albedo reduction caused by BC is therefore larger under cloudy sky (x-label case "cloudy") than under clear sky (x-label case "clear"). However, compared with the impact of accounting for non-BC LAPs and snow depth, the impact of accounting for cloud cover on albedo reduction is much smaller, ~10%.

As shown in Figure 4.11 panel (a), a low-bias in BC concentration will lead to a proportional decrease in albedo reduction induced by BC, for example, if the BC concentration is reduced by a factor of 10, the albedo reduction induced by BC will be reduced by approximately a factor of 10 in China, North America, and the Arctic. In contrast, the albedo reduction induced by BC does not increase linearly with the increase of BC concentration. Compared to North America and the Arctic, the relative increase in albedo reduction is smaller in China for the same relative increase in BC concentration, because snow in China already contains large amounts of BC. In contrast to the impact of BC concentration, biases in snow depth will not yield proportional biases in albedo reduction, especially in China where even a thin layer of snow is optically thick due to high BC concentrations. For new snow, if the snow depth is decreased by a factor of 10, the albedo reduction induced by BC is only decreased by a factor of 4, 5, and 2 for the Arctic, North America, and China respectively; if the snow depth is increased by a factor of 10, the albedo reduction induced by BC is increased by only a factor of 1.1 and 1.3 for the Arctic and North America, and almost no increase in China. For old snow, the change in albedo reduction is more sensitive to the change of snow depth because the optical depth of old melting snow is smaller for the same snow thickness.

If the albedo calculation does not include non-BC LAPs, as illustrated in Figure 4.11 panel (b), the change in albedo reduction induced by BC is disproportional to the changes of BC concentration, because the removal of non-BC LAPs increases the BC-in-snow albedo reduction even if there is no increase of BC concentrations (Figure 4.11, case "BC only"). An increase of snow depth or BC concentration yields a much larger change in the albedo reduction, and the regional differences are smaller. It is important to note that even if we reduce the snow depth for China to 50% of the observed values, the derived albedo reduction by BC still increases by 40% for new snow and 6% for old snow relative to the case where the snowpack contains non-BC LAPs. This is because the concentrations of non-BC LAPs in snow are so high in China that the removal of non-BC LAPs greatly increases albedo reduction by BC, which compensates for the drop of albedo reduction due to shallower snowpacks.

4.3.4 Snow depth distribution

For the 22 sites in subarctic Canada, the mean and distributed snow depths are shown in the top panel of Figure 4.12. The mean snow depths are in the range 20 to 50 cm for all but one site. If snow albedos were calculated using site-mean snow depth, we could overestimate both snow albedo and albedo reduction by BC, as shown in the bottom panel of Figure 4.12. The mean albedos of snowpacks with distributed depths are smaller by 0.0005 and 0.0040 for new snow and old snow; the mean albedo reduction is also smaller by $5*10^{-5}$ and 0.0002 for new snow and old snow. However, these changes are much smaller than the albedo reduction by BC in the Arctic region: 0.0045 for new snow and 0.0087 for old snow. We conclude that for mean snow depths > 20 cm, it is adequate for radiative computations to use the mean snow depths without consideration of the local depth-distribution.

4.4. Discussions and Summary

In this paper, we derived the direct albedo reduction induced by BC and non-BC LAPs in snow based on large-area field observations. We also investigated the impact of different snow conditions, LAP concentrations, and model setups on derived BC-in-snow albedo reductions. Comparisons of these quantities across three sampling regions are also highlighted.

Depending on the snow grain size, the direct albedo reduction caused by BC in the Arctic, North America, and China is 0.005, 0.005, 0.33 for new snow, and 0.01, 0.01, 0.06 for old snow. These values can be used for future model simulations to constrain the direct albedo reduction induced by BC. Correspondingly in the Arctic, North America, and China, the direct forcings by BC are 0.06, 0.3, 3 Wm^{-2} for new snow and 0.5, 0.9, 8 Wm^{-2} for old snow during the winter-spring transition. These forcings do not account for rapid adjustments (feedbacks). It is important to note that the direct radiative forcing induced by BC will be amplified through triggered feedback processes that involve both the snow and atmosphere (Figure 29, *Bond et al.,* 2013). These feedbacks are overwhelmingly positive, so the total effective radiative forcing induced by BC will be larger than the direct forcing estimated in this work.

To estimate the radiative forcing induced by BC in snow, it is important for model simulations to include non-BC LAPs as well. We find that non-BC LAPs are responsible for at least 50% of LAP-in-snow albedo reductions in our study regions (Table 4.1). The presence of non-BC LAPs in snow also reduces the amount of albedo reduction induced by BC. Simulations without non-BC LAPs in snow will therefore overestimate the albedo

reduction by BC, especially in China (Figure 4.11, Table 4.2). However, because some of the non-BC LAPs are emitted from anthropogenic sources, it is unclear whether the total direct forcing by anthropogenic LAPs-in-snow is overestimated.

Another important factor that models should consider is snow depth. As shown in Figure 4.11, albedo reduction by BC increases by a factor of 1 to 7 if the snow is ten times deeper than that measured; correspondingly, the impact of BC is smaller if snow depth is smaller than we measured at these sites. For regions with shallower snowpack, accurate representation of snow-covered fraction and snow depth distribution are probably more important in calculations of regional forcing. In this work, we showed that the impact of snow-depth distribution on snow albedo and albedo reduction by BC at 22 sites in subarctic Canada was small. However, in this region, the snow is deeper. The impact of depth distribution is expected to be larger in mid-latitude regions where snow is shallower.

As stated in the introduction, most studies testing modeled radiative forcing by BC in snow have focused on the simulated BC concentration in the surface snow layer. Those studies have shown that modeled BC concentrations can differ from observed concentrations by up to an order of magnitude. This error in BC concentration could yield a large error in derived albedo reduction by BC due to two reasons. First, the albedo reduction by BC is almost linear in BC concentration for the typical BC amounts we find (Figure 4.11). For example, doubling the amount of BC in snow would double the BC-in-snow albedo reduction for new snow in all three regions; such a change in BC-in-snow albedo reduction is larger if model simulations do not consider non-BC LAPs. Second, even if the modeled BC concentrations in the top layer agree with observations, the computed albedo reduction

could be erroneous. At almost all sampling sites, the top layer (5 cm) is not optically thick enough to hide the impact of the lower snowpack or the ground below (Figure 4.10).

Based on this work, our suggestions for future field observations and model testing regarding BC-in-snow albedo reduction are summarized as follows:

a) In addition to measuring BC, field observations on LAPs-in-snow should also measure non-BC LAPs (i.e. OC and MD). Ideally, both the mass and absorption properties of these constituents would be measured.

b) More measurements on snow depth distributions are needed, for both mid-latitudes and the Arctic.

c) For long-term observations of LAPs-in-snow at fixed locations, if it is not feasible to repeatedly sample the entire snowpack in layers (e.g. according to the snow stratigraphy) at a minimum the surface snow (top 5 cm) and the bulk snow below should each be sampled.

d) It is important for radiative transfer models to include non-BC LAPs in snow.

e) Testing for accurate model simulations of snow depth (as well as snow depth distributions, if the snow is thin) are crucial to model estimates of forcing by BC/LAPs in snow.

f) If radiative transfer calculations assume a homogenous snowpack, mean concentrations of BC in the surface snow layer (5 cm) should be used as the proxy data to evaluate the model performance on BC-induced direct albedo reduction and forcing, rather than the mean concentrations of BC in the entire snow column.

Acknowledgements

We thank Richard Brandt for providing the single-scattering properties of snow grains and black carbon particles from Mie calculation. This work was supported by NSF grant AGS-11-18460.

Figure 4.1. Snow depth and black carbon concentration (top 5 cm) at sampling locations. Sites are grouped into three major regions by dashed lines: North America (Doherty et al., 2014), Arctic (Doherty et al., 2010), and China (Wang et al., 2013). Sampling sites in subarctic Canada with additional snow depth data are enclosed with black solid lines (Sturm et al., 2008). White dots show sites where BC concentration was indeterminate because of high dust content.

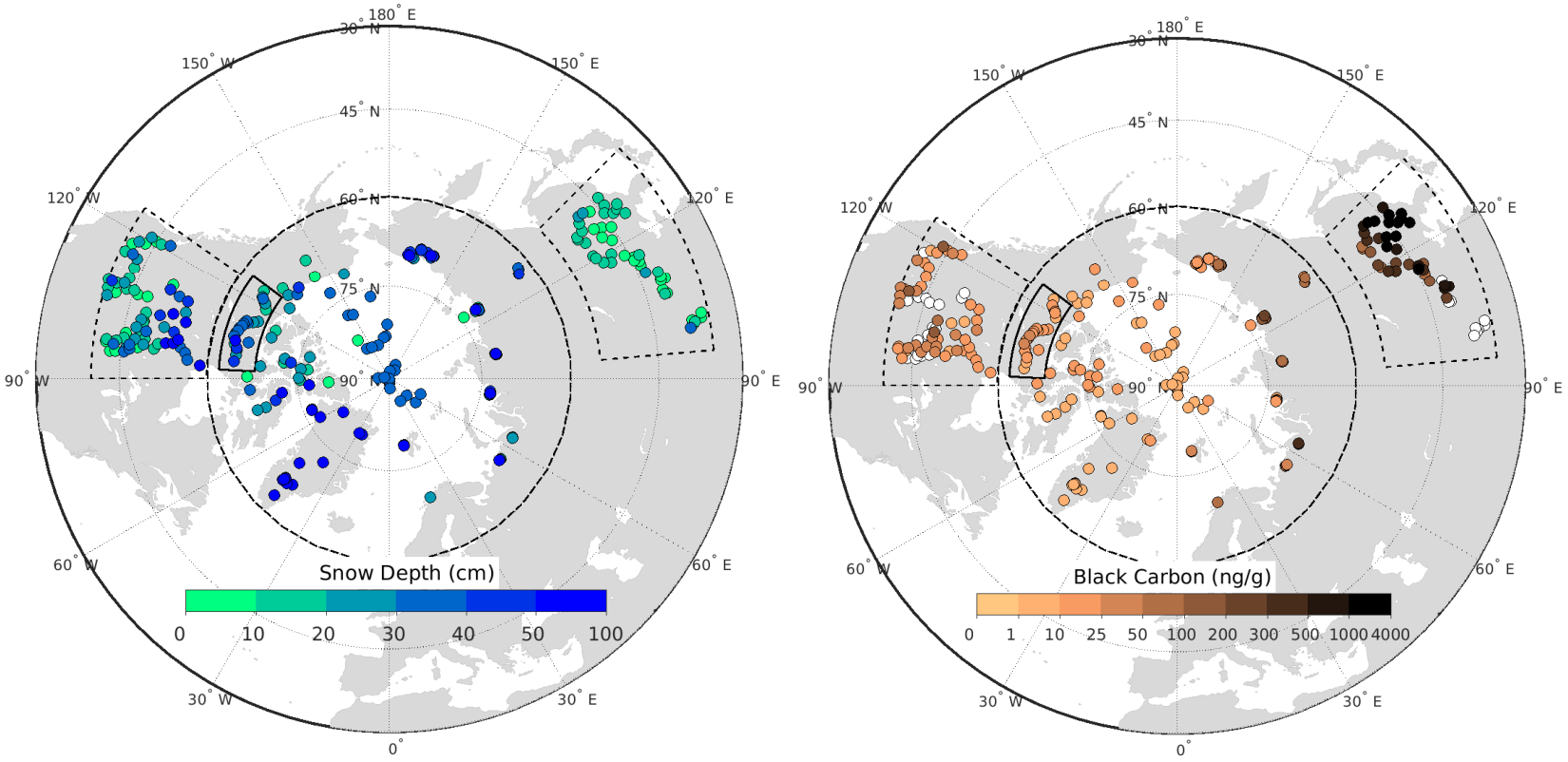

Figure 4.2. Snow depth and black carbon concentration (top 5 cm) in three regions: mean (red dots), median (black bar), 25th and 75th percentiles (box), and maximum/minimum values within ± 1.5 interquartile range: range between 25th and 75th percentiles (whiskers). Box-whisker plots in later figures also follow this convention.

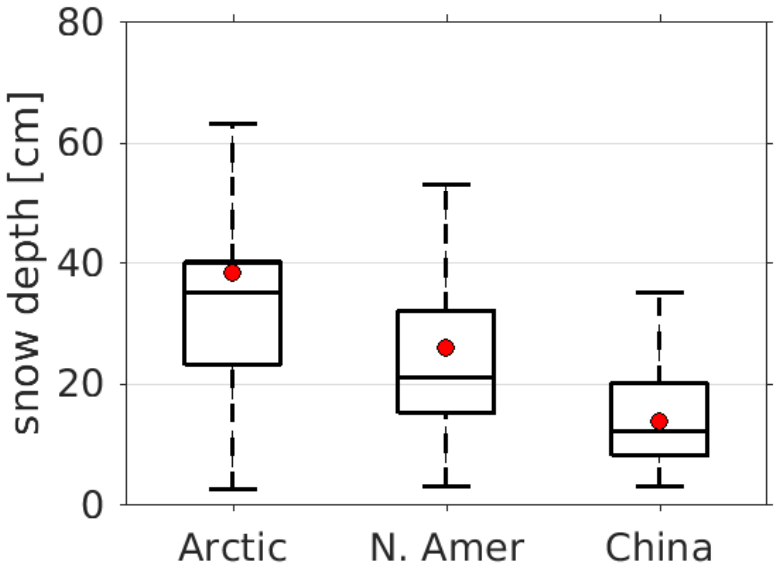

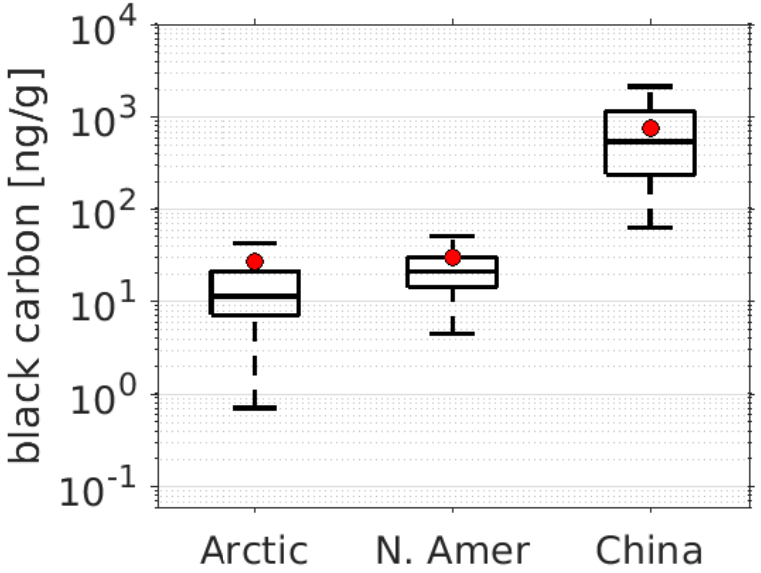

Figure 4.3. Surface types at snow-sampling locations
(NOAHv3.3 vegetation dataset, http://ldas.gsfc.nasa.gov/gldas/GLDASvegetation.php).

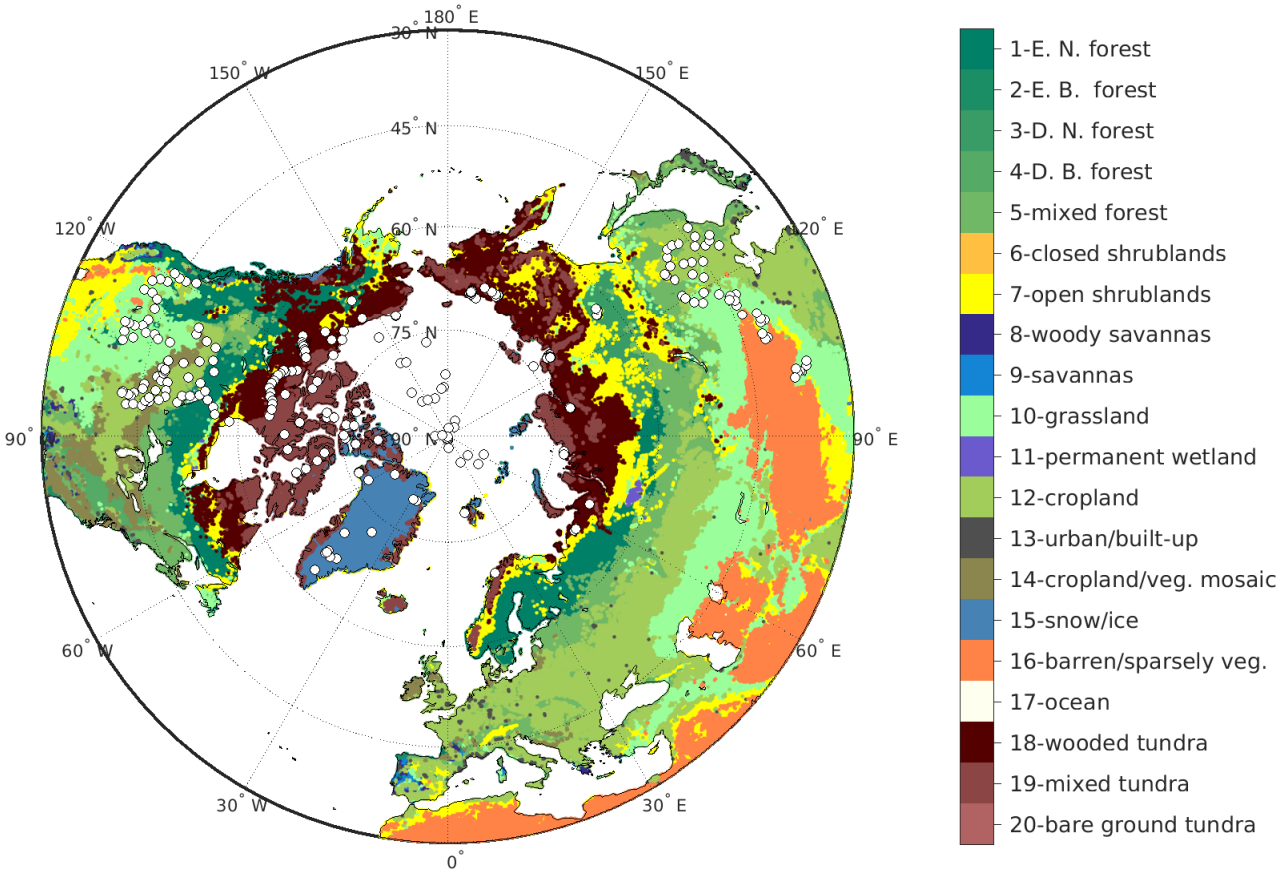

Figure 4.4. Spectral albedo of grassland, soil, and sea ice. Albedo of grassland was measured in Maryland (Figure 3, Liang et al., 2002); albedo of damp soil was measured on bare ground tundra of northeast Greenland (Figure 6, Bøggild et al., 2010); albedo of first-year sea ice was measured on the Antarctic Ocean (Figure 1, Brandt et al., 2005). The extrapolations of measured albedo (plus marks) to shorter and longer wavelengths (0.3 – 4 μm) are illustrated by the solid lines.

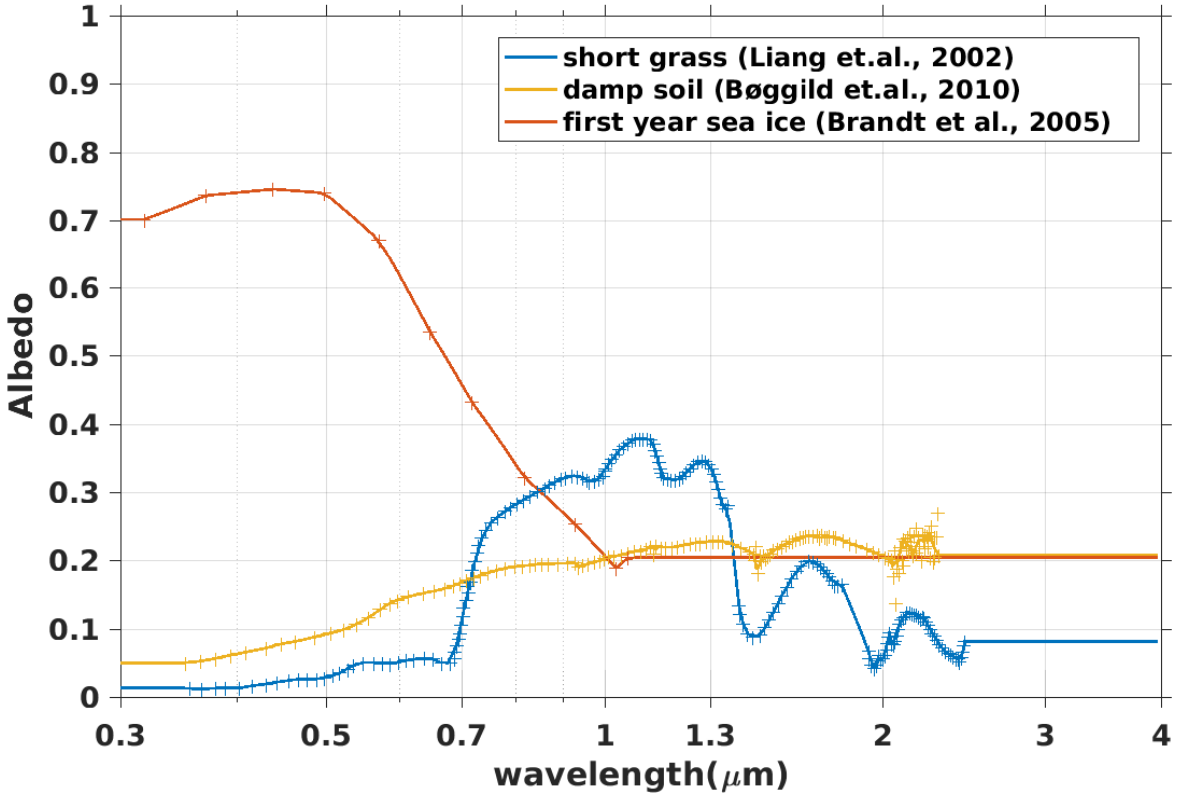

Figure 4.5. Monthly-mean downward surface shortwave flux (top 2 panels, clear sky and all sky) and total cloud fraction (bottom panel, sum of low, middle and high clouds during day time) in three sampling regions. The flux and cloud cover data are obtained from CERES (https://ceres.larc.nasa.gov/products.php?product=SYN1deg).

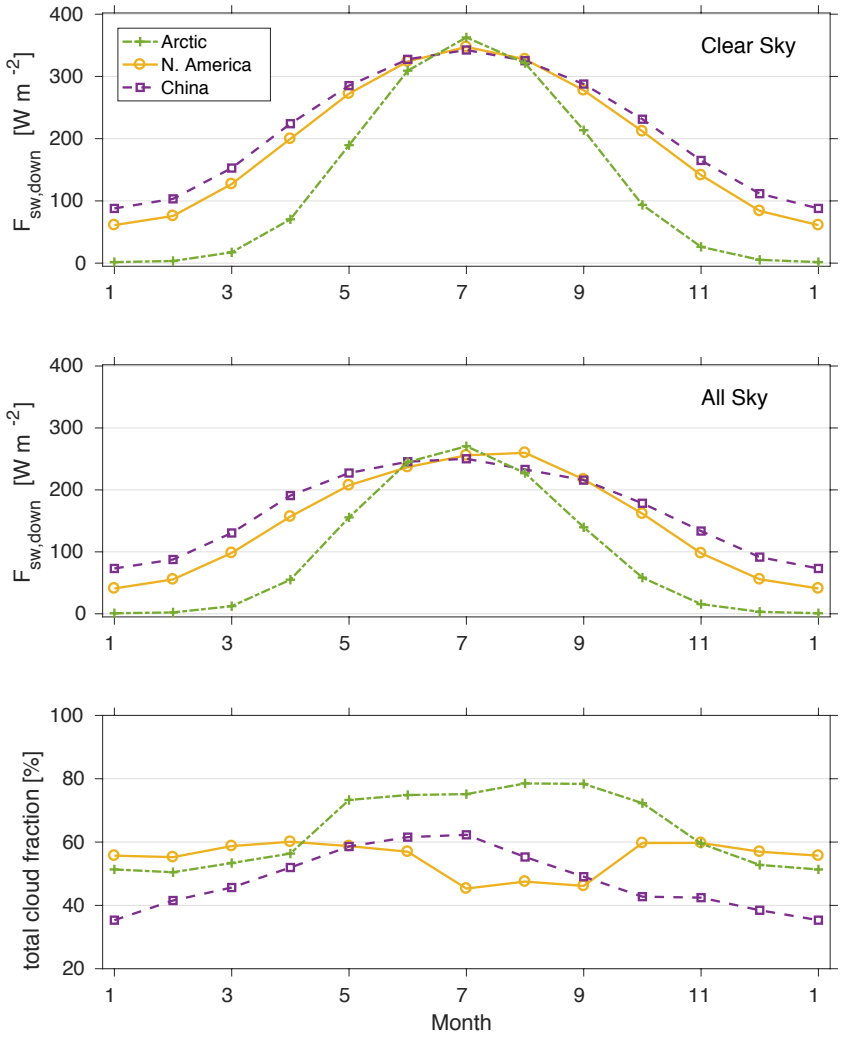

Figure 4.6. All-sky broadband albedo of snow derived from observed mixing ratios of LAPs for three regions. In each region, albedo is calculated for new snow (r = 100 μm) and old-melting snow (r = 1000 μm), for the four LAP scenarios described in Section 4.2.3.1: (1) pure: snow does not contain any LAPs; (2) nonBC: snow contains non-BC LAPs only; (3) BC: snow contains BC only; (3) LAPs: snow contains both BC and non-BC LAPs.

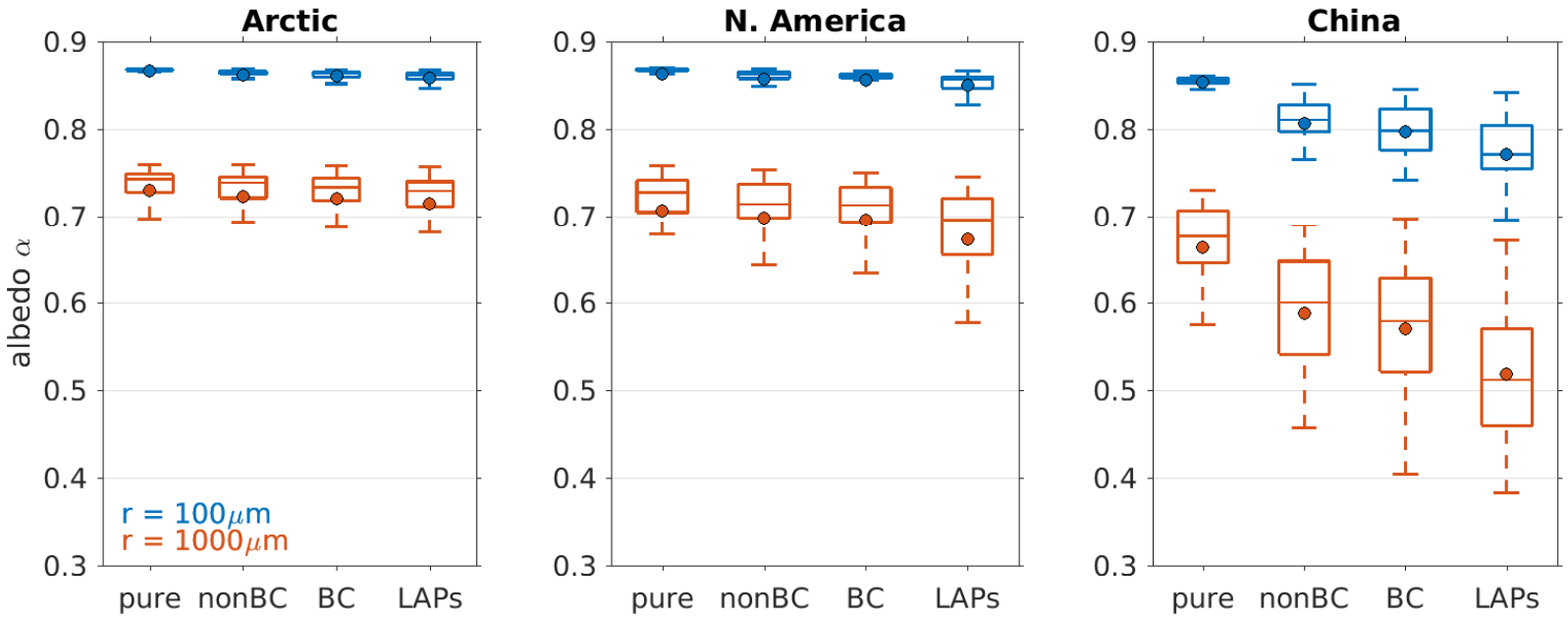

Figure 4.7. Regionally-averaged broadband albedo reduction (all-sky) induced by different LAPs for new snow (color-filled bars) and for old-melting snow (extended white bars). Black, yellow, and brown bars denote the albedo reductions by BC only, non-BC LAPs only, and by all LAPs (BC + non-BC LAPs) when compared with the albedo of pure snow. Grey bars give the sum of albedo reductions caused by BC and non-BC separately, for comparison to the albedo reduction when all LAPs are present in the snow together (3. LAPs).

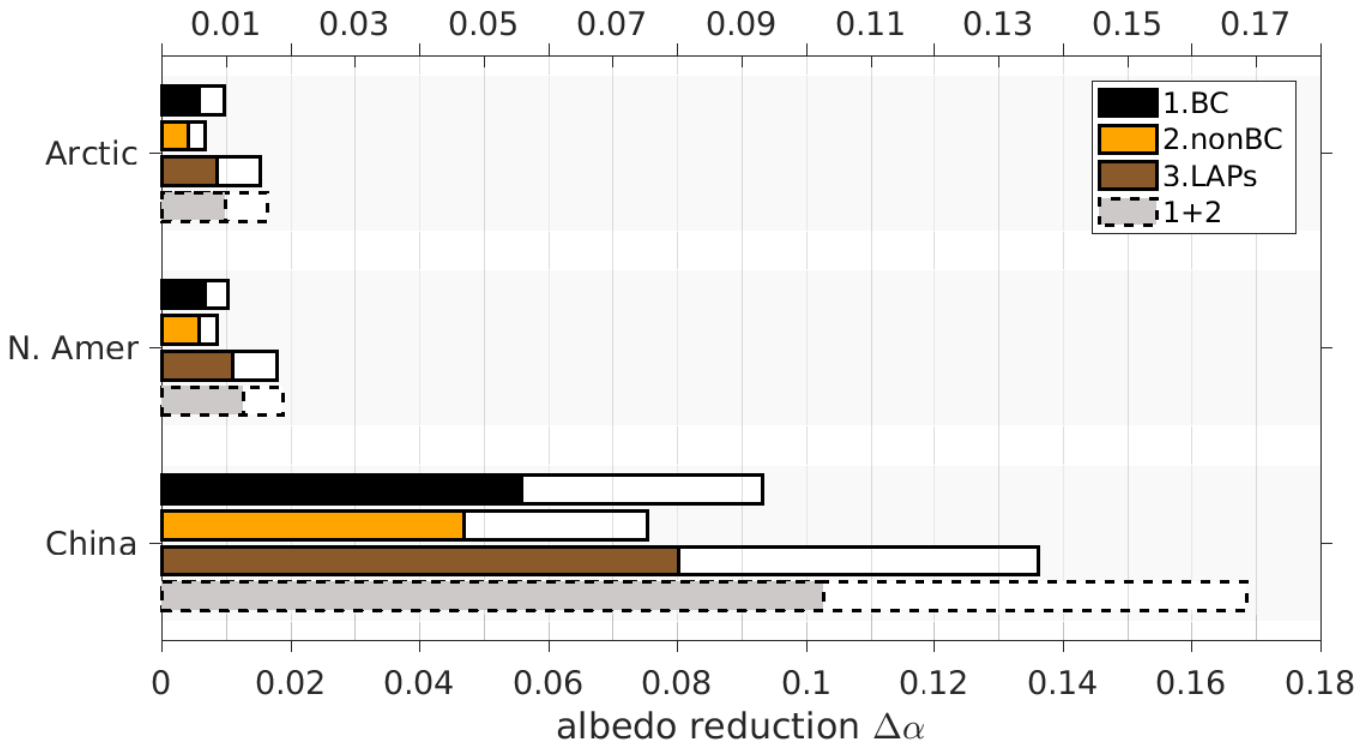

Figure 4.8. All-sky direct albedo reduction and the resulting radiative forcing resulting from BC in snow (new snow, r = 100 μm) for February (North America and China) and March (the Arctic). White dots show sites with indeterminate BC concentrations, and therefore no estimation of albedo reduction and radiative forcing are made for those sites.

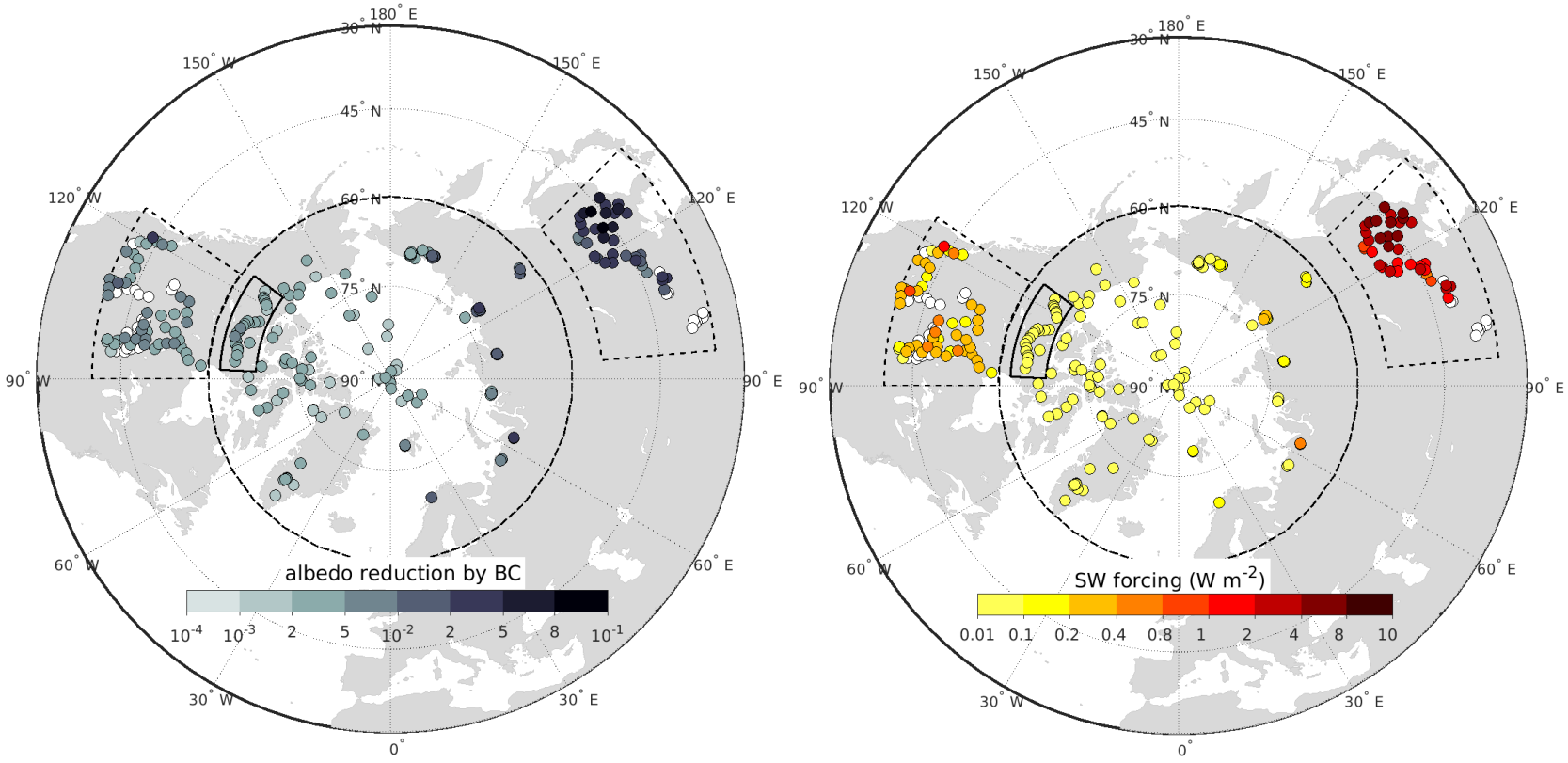

Figure 4.9. All-sky direct albedo reduction and radiative forcing induced by BC in snow in three regions. For new snow (r = 100 μm), cloud cover and shortwave flux of February and March are used for mid-latitudes and high-latitudes respectively, while for old snow (r = 1000 μm), values of March and April are used for mid-latitudes and high latitudes respectively.

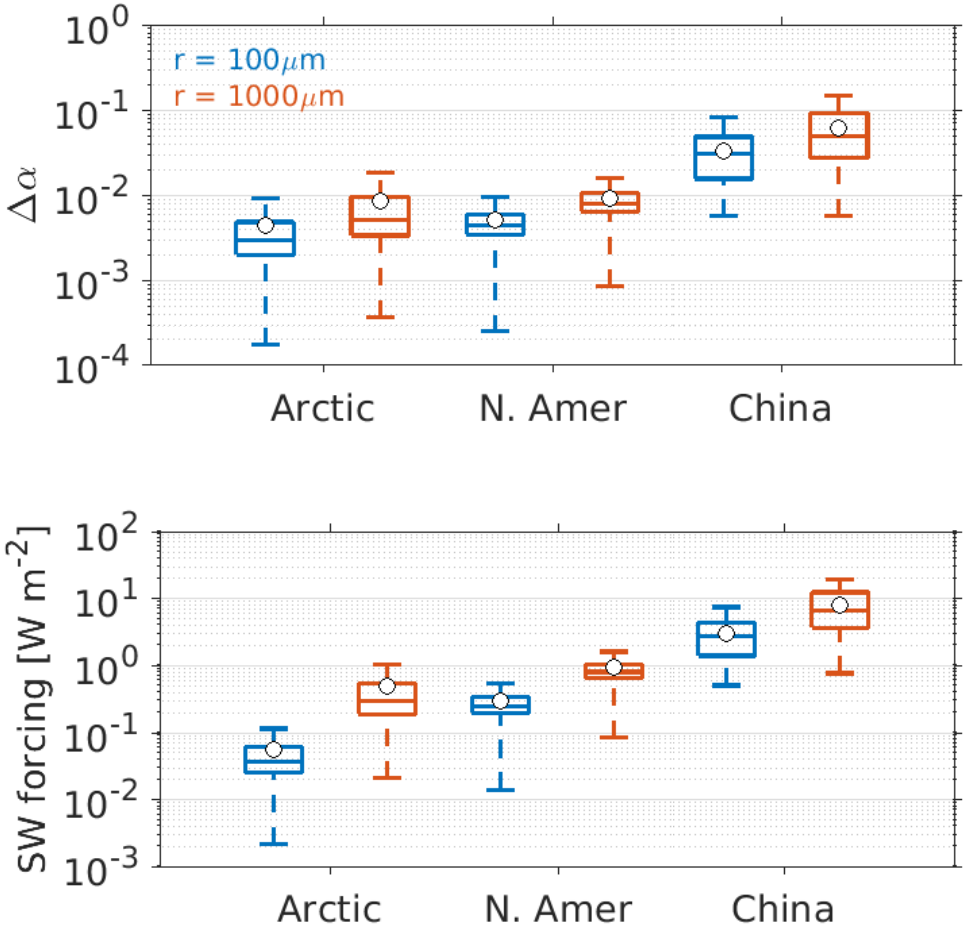

Figure 4.10. Comparison of direct albedo reduction (all-sky) induced by BC calculated with three vertical resolutions: multi-layer, one-layer, and two-layer snowpacks as described in section 4.2.3.2, for new snow (r = 100 μm) and old snow (r = 1000 μm). Numbers shown in the bottom right of each figure are the percentage errors and standard deviations of calculated albedo reduction if the vertical profiles of BC concentration were changed.

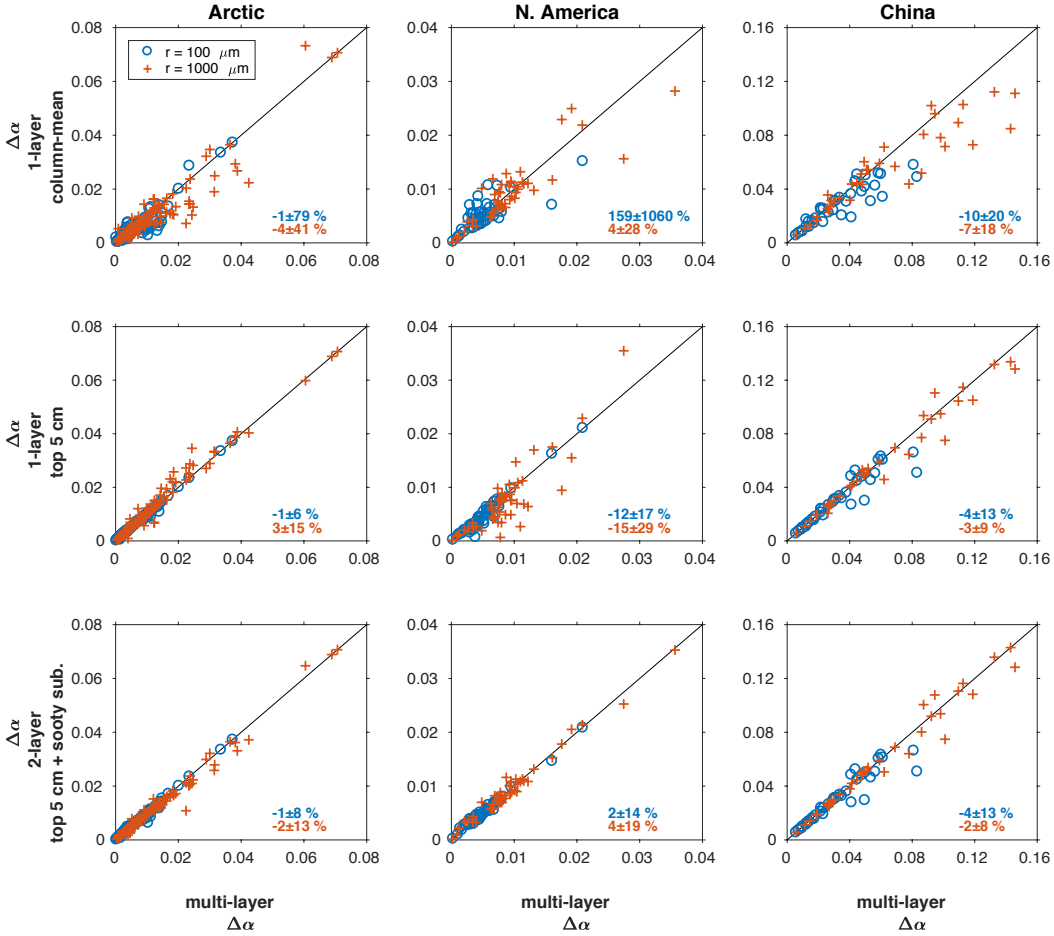

Figure 4.11. Relative change (left axis, $\delta\Delta\alpha/\Delta\alpha$) and absolute change ($\delta\Delta\alpha$, scale bars on right) in albedo reductions induced by BC (all-sky) for multiplicative factors applied to snow depths, cloud cover, and concentrations of BC and non-BC LAPs, for new snow (r = 100 μm) and old snow (r = 1000 μm). These changes are referenced to the albedo reduction derived from observed data $\Delta\alpha$ (snowpacks containing both BC and non-BC LAPs with observed snow depth, multi-layer model). For each case labeled on the x-axis, one or more conditions are altered. From left to right, in the left-most panel they are (1) "deep, BC", increasing snow depth to optically thick and removing non-BC LAPs; (2) "deep", optically thick snow; (3) "BC only", removing non-BC LAPs such that snow contains only BC; (4) "clear", clear sky; (5) "cloudy", cloudy sky. In the center and right panels, the BC concentration and snow depth are changed by factors 0.1, 0.2, 0.5, 2, 5, and 10 for models that (a) include non-BC LAPs or (b) do not include non-BC LAPs.

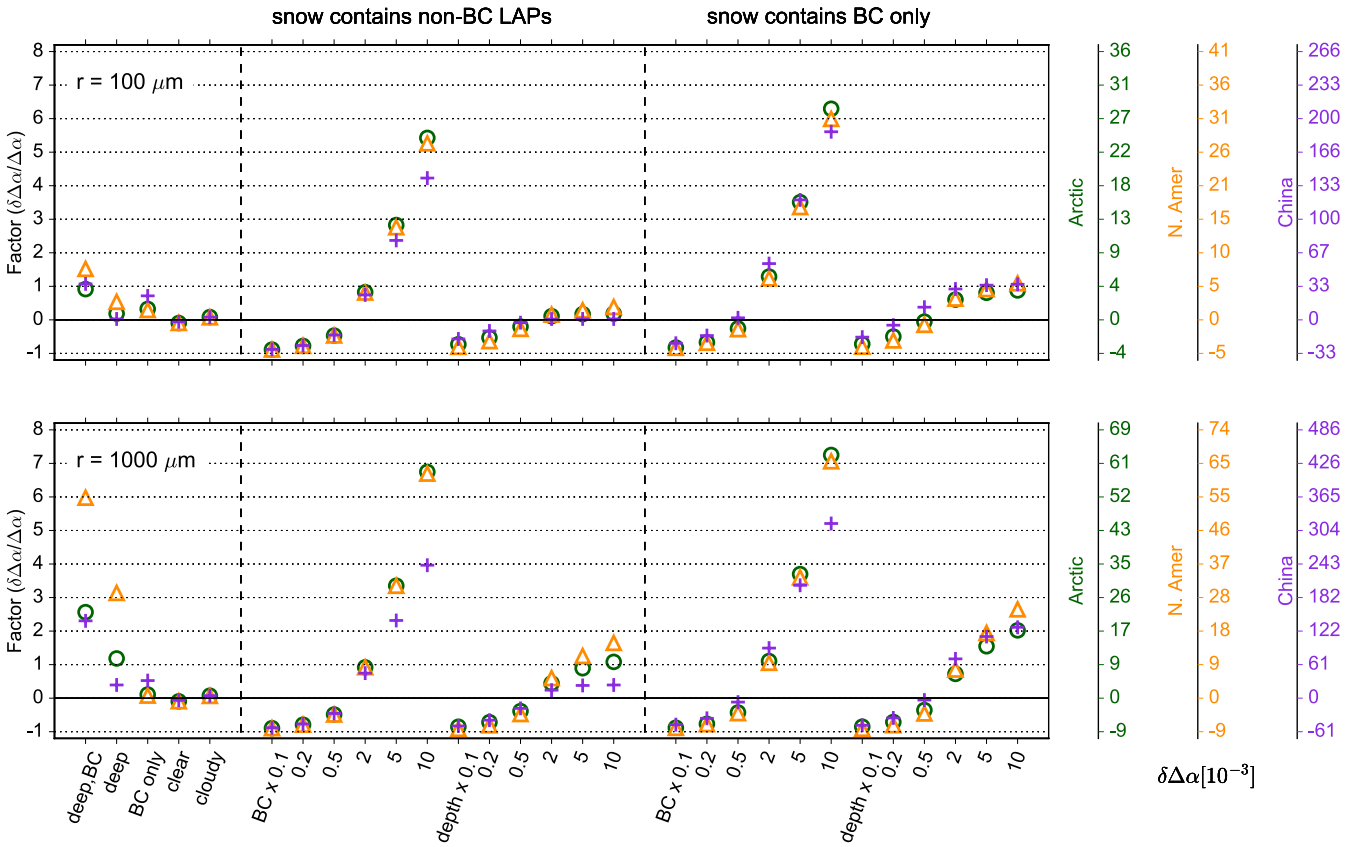

Figure 4.12. Top: snow depth distribution measured at 22 sites in subarctic Canada (region outlined by black box in Figure 4.1). Bottom panel: differences in snow albedo (α) and albedo reduction induced by BC (Δα) between values derived from a snowpack with mean depth and mean values derived from snowpacks with distributed depths. Values in parentheses are site-averaged data.

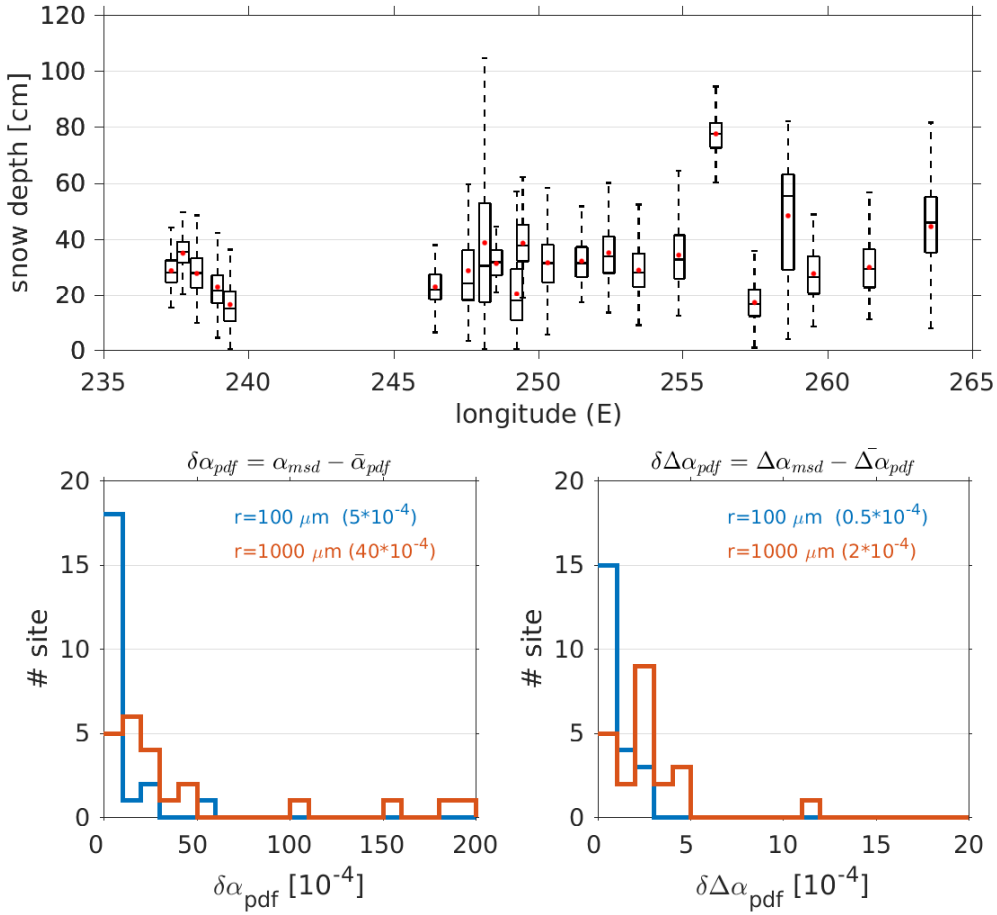

Table 4.1. Regional averages from observation and radiative transfer calculations. The snow albedo and albedo reduction are all-sky case calculated based on the monthly-averaged cloud fraction in different regions.

		Arctic		North America		China	
Snow depth	[cm]	38		26		14	
Black carbon BC (top 5 cm)	[ng/g]	27		29		756	
Black carbon BC (sub-surface)	[ng/g]	21		30		476	
		r = 100 μm (March)	r = 1000 μm (April)	r = 100 μm (February)	r = 1000 μm (March)	r = 100 μm (February)	r = 1000 μm (March)
Snow albedo		0.8662	0.7294	0.8619	0.6940	0.8531	0.6645
Albedo reduction by BC	[10^{-4}]	45	87	52	92	333	608
Albedo reduction by all LAPs	[10^{-4}]	86	153	126	211	823	1457
Cloud cover area	[%]	53	56	55	59	42	46
Downward shortwave flux F_{sw}	[W m^{-2}]	12	55	56	98	88	130
Shortwave forcing by BC	[W m^{-2}]	0.055	0.477	0.286	0.908	2.913	7.932

Table 4.2. Relative change ($\delta\Delta\alpha/\Delta\alpha$, grey shading), and absolute change ($\delta\Delta\alpha$, 10^{-4}) in albedo reductions induced by BC (all-sky, regional mean) if snow depths, cloud cover, or concentrations of BC and non-BC LAPs change, for new snow (r = 100 μm) and old snow (r = 1000 μm). Data are also plotted in Figure 4.10 for illustration.

		Arctic				North America				China			
		r = 100 μm (March)		r = 1000 μm (April)		r = 100 μm (February)		r = 1000 μm (March)		r = 100 μm (February)		r = 1000 μm (March)	
	Deep snow, BC only	28	0.92	124	2.56	41	1.52	186	5.98	303	1.07	996	2.31
	Deep snow	4	0.19	51	1.18	7	0.54	82	3.14	6	0.03	140	0.39
	BC only	13	0.33	10	0.11	16	0.29	9	0.08	225	0.72	323	0.52
	Clear sky	-4	-0.09	-8	-0.09	-5	-0.09	-9	-0.09	-19	-0.06	-38	-0.06
	Cloudy sky	4	0.08	6	0.07	4	0.08	6	0.07	26	0.08	45	0.07
Snow containing both BC and non-BC LAPs	BC * 0.1	-40	-0.89	-77	-0.9	-46	-0.89	-83	-0.9	-290	-0.88	-531	-0.88
	0.2	-35	-0.78	-68	-0.79	-40	-0.78	-73	-0.79	-251	-0.76	-459	-0.77
	0.5	-21	-0.47	-41	-0.49	-24	-0.47	-45	-0.49	-146	-0.45	-266	-0.46
	2	35	0.82	74	0.92	41	0.81	83	0.92	232	0.74	407	0.75
	5	116	2.83	254	3.35	135	2.76	292	3.35	715	2.37	1169	2.32
	10	216	5.43	484	6.75	252	5.26	564	6.69	1238	4.23	1866	3.96
	SD * 0.1	-31	-0.73	-73	-0.85	-40	-0.81	-83	-0.92	-171	-0.57	-485	-0.83
	0.2	-21	-0.53	-60	-0.72	-30	-0.64	-72	-0.81	-91	-0.33	-366	-0.66

	0.5	-7	-0.20	-30	-0.39	-12	-0.27	-41	-0.47	-21	-0.08	-150	-0.3
	2	3	0.11	27	0.44	5	0.16	42	0.6	5	0.02	96	0.24
	5	4	0.17	45	0.89	6	0.29	72	1.26	6	0.03	137	0.38
	10	4	0.18	49	1.08	7	0.38	78	1.65	6	0.03	140	0.39
Snow containing BC only	BC * 0.1	-37	-0.83	-76	-0.88	-43	-0.84	-81	-0.89	-226	-0.70	-470	-0.79
	0.2	-30	-0.67	-65	-0.77	-35	-0.68	-71	-0.78	-149	-0.47	-348	-0.6
	0.5	-12	-0.26	-35	-0.43	-13	-0.28	-40	-0.45	21	0.06	-50	-0.12
	2	52	1.29	89	1.11	63	1.23	99	1.05	515	1.68	845	1.49
	5	138	3.51	279	3.7	167	3.36	322	3.6	1066	3.58	1745	3.37
	10	242	6.29	517	7.25	290	5.99	606	7.06	1629	5.61	2519	5.21
	depth * 0.1	-30	-0.72	-73	-0.85	-40	-0.80	-83	-0.92	-148	-0.52	-473	-0.81
	0.2	-19	-0.50	-59	-0.71	-29	-0.61	-72	-0.81	-22	-0.16	-322	-0.59
	0.5	0	-0.05	-27	-0.36	-5	-0.15	-38	-0.46	139	0.38	13	0.06
	2	21	0.60	51	0.72	30	0.63	71	0.85	273	0.92	615	1.17
	5	26	0.81	93	1.55	37	0.92	138	1.94	296	1.03	864	1.84
	10	27	0.88	111	2.02	39	1.09	164	2.65	301	1.06	947	2.11

Chapter 5

SUMMARY

Snow is important for Earth's energy budget primarily because the albedo is greatly increased if the surface is covered by a layer of snow; an accurate calculation of snow albedo is therefore crucial for studying climate and snow hydrology. This dissertation introduces a new parameterization for snow albedo and albedo reduction induced by light-absorbing particles (black carbon and mineral dust), examines the effect of snow grain shape on snow albedo, and presents the impact of light-absorbing particles on snow albedo across North America, China, and the Arctic based on field observations and optical measurements.

The broadband albedo of pure deep snow is parameterized as quadratic functions of effective snow grain radius. The albedo reductions induced by black carbon and mineral dust are parameterized using a quadratic or cubic polynomial in the mixing ratio of black carbon or dust, whose coefficients are themselves quadratic in snow grain radius. This new parameterization can be applied to snowpacks with effective grain radii ranging from 5 – 2500 μm that contains black carbon or dust with mass fractions ranging from 0 (pure snow) to 10^{-5}. The snow grain radius and black carbon mass fraction are also combined into a single predictor to generate a much simpler parameterization for effective snow grain radius $r \geq 50$ μm. The albedo reduction induced by mineral dust is similar to that induced by a smaller concentration of black carbon. The effect of mineral dust on snow albedo can be represented by using an "equivalent" BC mixing ratio equal to the dust mixing ratio divided by a scaling factor of approximately 200.

For the same area-to-mass ratio, snowpacks consisting of non-spherical grains have higher albedo compared with snowpacks consisting of spherical grains, while the albedo

reduction induced by black carbon is smaller in the non-spherical case. These differences result from the smaller asymmetry factor of non-spherical snow grains compared with spherical snow grains. The albedo of snowpacks consisting of non-spherical grains can be mimicked by snowpacks consisting of spherical grains with smaller area-to-mass ratio by factors up to 2.4. For climate studies, the albedo reduction by light-absorbing particles might be over-estimated, unless the area-to-mass ratios of snowpacks used for radiative transfer calculation were retrieved from the snow albedo measurement and following the same assumption of snow grain shape.

In North America, China, and the Arctic, the mass mixing ratio of both black carbon and non-BC light-absorbing particles in snow are high enough to reduce the snow albedo. In China, the albedo reduction induced by BC is an order of magnitude higher than that in North America and the Arctic, due to the high mass mixing ratio of black carbon in snow. In all three regions, the presence of non-BC light absorbing particles reduces the impact of black carbon on snow albedo as the albedo reduction increases non-linearly with particle concentration when the concentration is high. The albedo reduction induced by black carbon can be estimated using a single-layer model with the black carbon concentration of the top 5 cm. More observations on light-absorbing particles in snow, snow depth, and snow depth distributions are needed for a better quantification of the impact of light-absorbing particles in snow.

BIBILIOGRAPHY

Ackerman, T.P., and O.B. Toon (1981), Absorption of visible radiation in atmosphere containing mixtures of absorbing and nonabsorbing particles, *Appl. Opt.*, *20*, 3661-3668.

Alfaro, S. C., S. Lafon, L. Rajot, P. Formenti, A. Gaudichet, and M. Maille (2004), Iron oxides and light absorption by pure desert dust: An experimental study, *J. Geophys. Res.*, *109*, D08208, doi:10.1029/2003JD004374.

Aoki, T., H. Motoyoshi, Y. Kodama, T. J. Yasunari, K. Sugiura, and H. Kobayashi (2006), Atmospheric aerosol deposition on snow surfaces and its effect on albedo, *SOLA*, *2,* 13-16.

Aoki, T., K. Kuchiki, M. Niwano, Y. Kodama, M. Hosaka, and T. Tanaka (2011), Physically based snow albedo model for calculating broadband albedos and the solar heating profile in snowpack for general circulation models, *J. Geophys. Res.,* 116, D11114, doi:10.1029/2010JD015507.

Aoki, T., T. Aoki, M. Fukabori, A. Hachikubo, Y. Tachibana, and F. Nishio (2000), Effects of snow physical parameters on spectral albedo and bidirectional reflectance of snow surface, *J. Geophys. Res.*, 105, 10,219–10,236, doi:10.1029/1999JD901122.

Balkanski, Y., M. Schulz, T. Claquin, and S. Guibert (2007), Reevaluation of mineral aerosol radiative forcings suggests a better agreement with satellite and AERONET data. *Atmos. Chem. Phys., 7,* 81-95.

Baum, B. A., P. Yang, A. J. Heymsfield, C. G. Schmitt, Y. Xie, A. Bansemer, Y. Hu, and Z. Zhang (2011), Improvements in shortwave bulk scattering and absorption models for the remote sensing of ice clouds. *Journal of Applied Meteorology and Climatology 5*0, no. 5:1037-1056.

Baumgardner, D., R. Subramanian, C. Twohy, J. Stith, and G. Kok (2008), Scavenging of black carbon by ice crystals over the northern Pacific, *Geophys. Res. Lett. 35*, L22815, doi:10.1029/2008GL035764.

Beine, H., C. Anastasio, G. Esposito, K. Patten, E. Wilkening, F. Domine, D. Voisin, M. Barret, S. Houdier, and S. Hall (2011), Soluble, light-absorbing species in snow at

Barrow, Alaska*, J. Geophys. Res., 116*, D00R05, doi:10.1029/2011JD016181.

Biomass-burning Experiment, *J. Geophys. Res., 113,* D00C03

Bøggild, C.E., R.E. Brandt, K.J. Brown, and S.G. Warren (2010), The ablation zone in northeast Greenland: Ice types, albedos, and impurities, *J. Glaciol., 56,* 101-113.

Bond, T. C., and R. W. Bergstrom (2006), Light absorption by carbonaceous particles: An investigative review. *Aerosol Science and Technology, 40*(1), 27-67.

Bond, T. C., D. G. Streets, K. F. Yarber, S. M. Nelson, J.-H. Woo, and Z. Klimont (2004), A technology-based global inventory of black and organic carbon emissions from combustion, *J. Geophys. Res., 109*, D14203, doi:10.1029/2003JD003697.

Bond, T. C., S. J. Doherty, D. W. Fahey, P. M. Forster, T. Berntsen, B. J. DeAngelo, M. G. Flanner, S. Ghan, B. Kärcher, D. Koch, S. Kinne, Y. Kondo, P. K. Quinn, M. C. Sarofim, M. G. Schultz, M. Schulz, C. Venkataraman, H. Zhang, S. Zhang, N. Bellouin, S. K. Guttikunda, P. K. Hopke, M. Z. Jacobson, J. W. Kaiser, Z. Klimont, U. Lohmann, J. P. Schwarz, D. Shindell, T. Storelvmo, S. G. Warren, and C. S. Zender (2013), Bounding the role of black carbon in the climate system: A scientific assessment. *J. Geophys. Res. Atmos., 118*, 1-173, doi:10.1002/jgrd.50171.

Bond, T.C. (2001), Spectral dependence of visible light absorption by carbonaceous particles emitted from coal combustion. *Geophysical Research Letters*, *28*(21), pp.4075-4078.

Brandt, R.E., S.G. Warren, A.P. Worby, and T.C. Grenfell (2005), Surface albedo of the Antarctic sea ice zone, *Journal of Climate, 18*(17), 3606-3622.

Brandt, R.E., S.G. Warren, and A.D. Clarke (2011), A controlled snowmaking experiment testing the relation between black carbon content and reduction of snow albedo, *J. Geophys. Res.*, *116*, D08109, doi:10.1029/2010JD015330.

Carmagnola, C. M., F. Domine, M. Dumont, P. Wright, B. Strellis, M. Bergin, J. Dibb, G. Picard, Q. Libois, L. Arnaudand, and S. Morin (2013), Snow spectral albedo at Summit, Greenland: measurements and numerical simulations based on physical and chemical properties of the snowpack, *The Cryosphere*, *7*, 1139-1160, doi:10.5194/tc-7-1139-2013.

Charlson, R.J., S.E. Schwartz, J.M. Hales, R.D. Cess, J.A. Coakley, Jr., J.E. Hansen, and D.J. Hoffman (1992), Climate forcing by anthropogenic aerosols. *Science, 255*, 423-430, doi:10.1126/science.255.5043.423.

Claquin, T., M. Schulz, and Y.J. Balkanski (1999), Modeling the mineralogy of atmospheric dust sources, *J. Geophys. Res., 104*, 22243-22256.

Clarke, A.D., and K.J. Noone (1985), Soot in the Arctic snowpack: A cause for perturbations in radiative transfer, *Atmos. Environ.*, *19*, 2045-2053.

Clarke, A.D., K.J. Noone, J. Heintzenberg, S.G. Warren, and D.S. Covert (1987), Aerosol light absorption measurement techniques: analysis and intercomparisons, *Atmos. Environ., 21*, 1455-1465.

Clarke, A.D., Y. Shinozuka, V.N. Kapustin, S. Howell, B. Huebert, S. Doherty, T. Anderson, D. Covert, J. Anderson, X. Hua, K.G. Moore II, C. McNaughton, G. Carmichael, and R. Weber (2004), Size distributions and mixtures of dust and black carbon aerosol in Asian outflow: Physiochemistry and optical properties, *J. Geophys. Res., 109*, D15S09, doi:10.1029/2003JD004378.

Dadic, R., P.C. Mullen, M. Schneebeli, R.E. Brandt, and S.G. Warren (2013), Effects of bubbles, cracks, and volcanic tephra on the spectral albedo of bare ice near the Transantarctic Mountains: Implications for sea glaciers on Snowball Earth. *J. Geophys. Res.*, 118, doi:10.1002/jgrf.20098.

Dang, C., and D. A. Hegg (2014), Quantifying light absorption by organic carbon in Western North American snow by serial chemical extractions, *J. Geophys. Res. Atmos., 119*, 10,247–10,261, doi:10.1002/2014JD022156.

Dang, C., R. E. Brandt, and S. G. Warren (2015), Parameterizations for narrowband and broadband albedo of pure snow, and snow containing mineral dust and black carbon. *J. Geophys. Res.,* 120, doi:10.1002/2014JD022646.

Davidson, C.I., S. Santhanam, R.C. Fortmann, and P.O. Marvin (1985), Atmospheric transport and deposition of trace elements onto the Greenland ice sheet. *Atmospheric Environment,19*(12), pp.2065-2081.

Doherty, S. J., C. Dang, D. A. Hegg, R. Zhang, and S. G. Warren (2014), Black carbon and other light-absorbing particles in snow of central North America, *J. Geophys. Res. Atmos., 119*, 12,807–12,831, doi:10.1002/2014JD022350.

Doherty, S. J., D. A. Hegg, J. E. Johnson, P. K. Quinn, J. P. Schwarz, C. Dang, and S. G. Warren (2016), Causes of variability in light absorption by particles in snow at sites in Idaho and Utah. *J. Geophys. Res. Atmos., 121*, 9: 4751-4768,

DOI:10.1002/2015jd024375.

Doherty, S. J., S. G. Warren, T. C. Grenfell, A. D. Clarke, and R. Brandt (2010), Light-absorbing impurities in Arctic snow, *Atmos. Chem. Phys., 10 (23)*, 11647-11680, doi:10.5294/acp-10-11647-2010.

Doherty, S.J., C. Dang, D.A. Hegg, R. Zhang, and S.G. Warren (2014), Black carbon and other light-absorbing particles in snow of central North America. *J. Geophys. Res., 119,* 12807-12831, doi:10.1002/2014JD022350.

Doherty, S.J., P.K. Quinn, A. Jefferson, C.M. Carrico, T.L. Anderson, and D. Hegg (2005), A comparison and summary of aerosol optical properties as observed in situ from aircraft, ship, and land during ACE-Asia, *J. Geophys. Res., 110,* D04201,

doi:10.1029/2004JD004964.

Doherty, S.J., T.C. Grenfell, S. Forsström, D.L. Hegg, R.E. Brandt, and S.G. Warren (2013), Observed vertical redistribution of black carbon and other insoluble light-absorbing particles in melting snow, *J. Geophys. Res.*, 118, doi:10.1002/jgrd.50235.

Dubovik, O., B. Holben, T.F. Eck, A. Smirnov, Y.J. Kaufman, M.D. King, D. Tanré, and I. Slutsker (2002), Variability of absorption and optical properties of key aerosol types observed in worldwide locations, *J. Atmos. Sci., 59*, 590-608.

Flanner, M. G., and C. S. Zender (2006), Linking snowpack microphysics and albedo evolution. *J. Geophys. Res.*, *111*, D12208, doi:10.1029/2005JD006834

Flanner, M. G., C. S. Zender, J. T. Randerson, and P. J. Rasch (2007), Present day climate forcing and response from black carbon in snow, *J. Geophys. Res.,* 112, D11202, doi:10.1029/2006JD008003.

Flanner, M.G., C.S. Zender, P.G. Hess, N.M. Mahowald, T.H. Painter, V. Ramanathan, and P.J. Rasch (2009), Springtime warming and reduced snow cover from carbonaceous particles, *Atmos. Chem. Phys.*, *9*, 2481-2497.

Flanner, M.G., C.S. Zender, P.G. Hess, N.M. Mahowald, T.H. Painter, V. Ramanathan, and P.J. Rasch (2009), Springtime warming and reduced snow cover from carbonaceous particles, *Atmos. Chem. Phys., 9,* 2481-2497.

Flanner, M.G., X. Liu, C. Zhou, J.E. Penner, and C. Jiao (2012), Enhanced solar energy absorption by internally-mixed black carbon in snow grains, *Atmos. Chem. Phys., 12,* 4699-4721.

Formenti, P., J.L. Rajot, K. Desboeufs, S. Caquineau, S. Chevaillier, S. Nava, A. Gaudichet, E. Journet, S. Triqute, S. Alfaro, M. Chiari, J. Haywood, H. Coe, and E. Highwood (2008), Regional variability of the composition of mineral dust from western Africa: Results from the AMMA SOP0/DABEX and DODO field campaigns, *J. Geophys. Res., 113*, D00C13, doi:10.1029/2008JD009903.

Formenti, P., L. Schütz, Y. Balkanski, K. Desboeufs, M. Ebert, K. Kandler, A. Petzold, D. Scheuvens, S. Weinbruch, and D. Zhang (2011), Recent progress in understanding physical and chemical properties of African and Asian mineral dust, *Atmos. Chem. Phys., 11,* 8231-8256.

Forsström, S., J. Ström, C.A. Pedersen, E. Isaksson, and S. Gerland (2009), Elemental carbon distribution in Svalbard snow, *J. Geophys. Res.*, *114*, D19112, doi:10.1029/2008JD011480.

Francis, P. N., A. Jones, R. W. Saunders, K. P. Shine, A. Slingo, and Z. Sun (1994), An observational and theoretical study of the radiative properties of cirrus: Some results from ICE'89. *Quart. J. Roy. Meteor. Soc.*, 120, 809–848.

Fu, Q. (1996), An accurate parameterization of the solar radiative properties of cirrus clouds for climate models. *J. Climate*, 9, 2058-2082.

Fu, Q. (2007), A new parameterization of an asymmetry factor of cirrus clouds for climate models. *J. Atmos. Sci.,* 64, 4144-4154.

Fu, Q., P. Yang, and W.B. Sun (1998), An accurate parameterization of the infrared radiative properties of cirrus clouds for climate models. *J. Climate*, *11*, 2223-2237.

Fu, Q., W.B. Sun, and P. Yang (1999), On modeling of scattering and absorption by nonspherical cirrus ice particles in thermal infrared wavelengths. *J. Atmos. Sci.*, 56, 2937-2947.

Fuller, K.A., W.C. Malm, and S.M. Kreidenweis (1999), Effects of mixing on extinction by carbonaceous particles, *J. Geophys. Res., 104,* 15941-15954.

Gardner, A.S., and M.J. Sharp (2010), A review of snow and ice albedo and the development of a new physically based broadband albedo parameterization, *J. Geophys. Res., 115,* F01009, doi:10.1029/2009JF001444.

Garrett, T. J., P. V. Hobbs, and H. Gerber (2001), Shortwave, single-scattering properties of arctic ice clouds. *J. Geophys. Res., 106*, 15 155–15 172.

Goudie, A.S., and N.J. Middleton (2006), *Desert Dust in the Global System*, Springer, Heidelberg.

Grannas, A. M., A. E. Jones, J. Dibb, M. Ammann, C. Anastasio, H. J. Beine, M. Bergin, J. Bottenheim, C. S. Boxe, G. Carver, G. Chen, J. H. Crawford, F. Dominé, M. M. Frey, M. I. Guzmán, D. E. Heard, D. Helmig, M. R. Hoffmann, R. E. Honrath, L. G. Huey, M. Hutterli, H. W. Jacobi, P. Klán, B. Lefer, J. McConnell, J. Plane, R. Sander, J. Savarino, P. B. Shepson, W. R. Simpson, J. R. Sodeau, R. von Glasow, R. Weller, E. W. Wolff, and T. Zhu (2007), An overview of snow photochemistry: evidence, mechanisms and impacts, *Atmos. Chem. Phys., 7*, 4329-4373, doi:10.5194/acp-7-4329-2007.

Grenfell, T. C., S. P. Neshyba, and S. G. Warren (2005), Representation of a nonspherical ice particle by a collection of independent spheres for scattering and absorption of radiation: 3. Hollow columns and plates. *J. Geophys. Res.*, 110(D17), 203, doi:10.1029/2005JD005811.

Grenfell, T.C., and D.K. Perovich (2008), Incident spectral irradiance in the Arctic Basin during the summer and fall, *J. Geophys. Res., 113*, D12117, doi:10.1029/2007JD009418.

Grenfell, T.C., and S.G. Warren (1999), Representation of a nonspherical ice particle by a collection of independent spheres for scattering and absorption of radiation, *J. Geophys. Res., 104,* 31697-31709.

Grenfell, T.C., S.G. Warren, and P.C. Mullen (1994), Reflection of solar radiation by the Antarctic snow surface at ultraviolet, visible, and near-infrared wavelengths, *J. Geophys. Res., 99,* 18669-18684.

Grenfell, T.C., S.J. Doherty, A.D. Clarke, and S.G. Warren (2011), Light absorption from particulate impurities in snow and ice determined by spectrophotometric analysis of filters. *Applied Optics, 50*, 2037-2048.

Hadley, O.L., and T.W. Kirchstetter (2012), Black carbon reduction of snow albedo, *Nature Climate Change, 2,* 437-440.

Hagler, G.S.W., M.H. Bergin, E.A. Smith, and J.E. Dibb (2007), A summer time series of particulate carbon in the air and snow at Summit, Greenland, *J. Geophys. Res., 112*, D21309, doi:10.1029/2007JD008993.

Hansen, J., and L. Nazarenko (2004), Soot climate forcing via snow and ice albedos, *Proc. Natl. Acad. Sci. USA, 101*, 423-428.

Hansen, J.E., and L.D. Travis (1974), Light scattering in planetary atmospheres, *Space Sci. Rev., 16,* 527-610.

Haywood, J., P. Francis, S. Osborne, M. Glew, N. Loeb, E. Highwood, D. Tanré, G. Myhre, P. Formenti, and E. Hirst (2003), Radiative properties and direct radiative effect of Saharan dust measured by the C-130 aircraft during SHADE: 1. Solar spectrum, *J. Geophys. Res., 108,* 8577, doi:10.1029/2002JD002687.

Hegg, D.A., S.G. Warren, T.C. Grenfell, S.J. Doherty, and A.D. Clarke (2010), Sources of light-absorbing aerosol in Arctic snow and their seasonal variation, *Atmos. Chem. Phys.*, *10*, 10923-10938 .

Holland, M.M., D.A. Bailey, B.P. Briegleb, B. Light, and E. Hunke (2012), Improved sea ice shortwave radiation physics in CCSM4: The impact of melt ponds and aerosols on Arctic sea ice, *J. Climate*, doi:10.1175/JCLI-D-11-00078.1.

Holz, R. E., S. Platnick, K. Meyer, M. Vaughan, A. Heidinger, P. Yang, G. Wind, S. Dutcher, S. Ackerman, N. Amarasinghe, F. Nagle, and C. Wang (2015), Resolving ice cloud optical thickness biases between CALIOP and MODIS using infrared retrievals, *Atmos. Chem. Phys. Discuss.*, 15, 29455-29495, doi:10.5194/acpd-15-29455-2015.

Huang, J., Q., Fu, W. Zhang, X. Wang, R. Zhang H. Ye, and S. G. Warren (2011), Dust and black carbon in seasonal snow across northern China. *Bulletin of the American Meteorological Society, 92*(2), 175-181.

Jacobson, M.Z. (2004), Climate response of fossil fuel and biofuel soot, accounting for soot's feedback to snow and sea ice albedo and emissivity, *J. Geophys. Res., 109*, doi:10.1029/2004JD004945.

Jin, Z., T. P. Charlock, P. Yang, Y. Xie, and W. Miller (2008), Snow optical properties for different particle shapes with application to snow grain size retrieval and MODIS/CERES radiance comparison over Antarctica, *Remote Sens. Environ.*, 112, 3563– 3581, doi:10.1016/j.rse.2008.04.011.

Joseph, J. H., W. J. Wiscombe, and J. A. Weinman (1976), The delta-Eddington approximation for radiative flux transfer. *J. Atmos. Sci.*, 33, 2452–2459.

Kandler, K., L. Schütz, C. Deutscher, M. Ebert, H. Hofmann, S. Jäckel, R. Jaenicke, P. Knippertz, K. Lieke, A. Massling, A. Petzold, A. Schladitz, B. Weinzierl, A. Wiedensohler, S. Zorn, and S. Weinbruch (2009), Size distribution, mass concentration, chemical and mineralogical composition and derived optical parameters of the boundary layer aerosol at Tinfou, Morocco, during SAMUM 2006, *Tellus B, 61,* 32-50.

Key, J. R., P. Yang, B. A. Baum, and S. L. Nasiri (2002), Parameterization of shortwave ice cloud optical properties for various particle habits. *Journal of Geophysical Research: Atmospheres* 107(D13), doi:10.1029/2001JD000742.

Kirchstetter, T. W., T. Novakov, and P. V. Hobbs (2004), Evidence that the spectral dependence of light absorption by aerosols is affected by organic carbon, *J. Geophys. Res., 109*, D21208, doi:10.1029/2004JD004999.

Koch, D., and A.D. Del Genio (2010), Black carbon absorption effects on cloud cover: Review and synthesis. Atmos. Chem. Phys., 10, 7685-7696, doi:10.5194/acp-10-7685-2010.

Koch, D., S. Menon, A. DelGenio, R. Ruedy, I. Alienov, and G.A. Schmidt (2009), Distinguishing aerosol impacts on climate over the past century, *J. Climate*, *22*, 2659-2677, doi:10.1175/2008JCLI2573.1.

Kok, J.F. (2011), A scaling theory for the size distribution of emitted dust aerosols suggests climate models underestimate the size of the global dust cycle, *Proc. Nat. Acad. USA, 108*, 1016-1021.

LaChapelle, E.R. (1969), *Field Guide to Snow Crystals*. University of Washington Press, Seattle.

Lafon, S., I.N. Sokolik, J.L. Rajot, S. Caquineau, and A. Gaudichet (2006), Characterization of iron oxides in mineral dust aerosols: Implications for light absorption, *J. Geophys. Res.*, 111, D21207, doi:10.1029/2005JD007016.

Lawrence, D.M., K.W. Oleson, M.G. Flanner, C.G. Fletcher, P.J. Lawrence, S. Levis, S.C. Swenson, and G.B. Bonan (2012), The CCSM4 land simulation, 1850-2005: Assessment of surface climate and new capabilities, *J. Climate*, *25*, 2240-2260, doi:10.1175/JCLI-D-11-00103.1.

Lawrence, D.M., K.W. Oleson, M.G. Flanner, P.E. Thornton, S.C. Swenson, P.J. Lawrence, X. Zeng, Z.-L. Yang, S. Levis, K. Sakaguchi, G.B. Bonan, and A.G. Slater (2011), Parameterization improvements and functional and structural advances in Version 4 of the Community Land Model, *Journal of Advances in Modeling Earth Systems, 30*, 3001, doi:10.1029/2011MS000045.

Lazaro, F.J., L. Gutiérrez, V. Barrón, and M.D. Gelado (2008), The speciation of iron in desert dust collected in Gran Canaria (Canary Islands): Combined chemical, magnetic and optical analysis, *Atmos. Environ., 42*, 8987-8996.

Liang, S., H. Fang, M. Chen, C. Walthall, C. Daughtry, J. Morisette, C. Schaaf, and A. Strahler (2002), Validating MODIS land surface reflectance and albedo products: Methods and preliminary results, Remote Sensing of Environment, 83(1-2):149-162.

Libois, Q., G. Picard, J.L. France, L. Arnaud, M. Dumont, C.M. Carmagnola, and M.D. King (2013), Influence of grain shape on light penetration in snow. *The Cryosphere, 7,* 1803-1818, doi:10.5194/tc-7-1803-2013.

Libois, Q., G. Picard, M. Dumont, L. Arnaud, C. Sergent, E. Pougatch, M. Sudul, and D. Vial (2014), Experimental determination of the absorption enhancement parameter of snow. *J. Glaciol.*, *60*, 714-724, doi:10.3189/2014JoG14J015.

Linke, C., O. Möhler, A. Veres, A. Mohacsi, Z. Bozoki, G. Szabo, and M. Schnaiter (2006), Optical properties and mineralogical composition of different Saharan mineral dust samples: a laboratory study, *Atmos. Chem. Phys., 6,* 3315-3323.

Liou, K. N., Y. Takano, C. He, P. Yang, R. L. Leung, Y. Gu, and W. L. Lee (2014), Stochastic parameterization for light absorption by internally mixed BC/dust in snow grains for application to climate models. *J. Geophys. Res.*, 119, 7616-7632, doi: 10.1002/2014JD021665.

Macke, A., J. Mueller, and E. Raschke (1996), Single scattering properties of atmospheric ice crystals. *Journal of the Atmospheric Sciences*, *53*(19), pp.2813-2825.

Maring, H., D.L. Savoie, M.A. Izaguirre, L. Custals, and J.S. Reid (2003), Mineral dust aerosol size distribution change during atmospheric transport, *J. Geophys. Res., 108*, 8592, doi:10.1029/2002JD002536.

Marshall, S., and R.J. Oglesby (1994), An improved snow hydrology for GCMs, Part 1: Snow cover fraction, albedo, grain size, and age, *Clim. Dyn., 10,* 21-37.

Marshall, S.E. (1989), A Physical Parameterization of Snow Albedo for Use in Climate Models, NCAR Cooperative Thesis 123, National Center for Atmospheric Research, Boulder, CO, 175 pp.

Marshall, S.E. (1989), *A Physical Parameterization of Snow Albedo for Use in Climate Models*, NCAR Cooperative Thesis 123, National Center for Atmospheric Research, Boulder, CO, 175 pp.

Marshall, S.E., and S.G. Warren (1987), Parameterization of snow albedo for climate models, in *Large Scale Effects of Seasonal Snow Cover, IAHS Publ. no. 166* (Eds. B.E. Goodison, R.G. Barry, and J. Dozier), International Association of Hydrological Sciences, 43-50.

Matzl, M., and M. Schneebeli (2006), Measuring specific surface area of snow by near-infrared photography, *J. Glaciol.*, *52*, 558-564.

Matzl, M., and M. Schneebeli (2010), Stereological measurement of the specific surface area of seasonal snow types: Comparison to other methods, and implications for mm-scale vertical profiling, *Cold Regions Sci. Tech., 64*, 1-8.

McClatchey, R. A., R. W. Fenn, J. F. A. Selby, F. E. Volz, and J. S. Garing (1972), *Optical properties of the atmosphere,* 3d ed., Air Force Geophysics Laboratory Rep. AFCRL-72-0497, Hanscom, MA, 108 pp.

McConnell, C.L., P. Formenti, E.J. Highwood, and M.A.J. Harrison (2010), Using aircraft measurements to determine the refractive index of Saharan dust during the DODO experiments, *Atmos. Chem. Phys., 10*, 3081-3098.

McConnell, J.R., R. Edwards, G.L. Kok, M.G. Flanner, C.S. Zender, E.S. Saltzman, J.R. Banta, D.R. Pasteris, M.M. Carter, and J.D.W. Kahl (2007), 20th century industrial black carbon emissions altered Arctic climate forcing, *Science, 317*, 1381-1384, doi: 10.1126/science.1144856.

Meland, B., P.D. Kleiber, V.H. Grassian, and M.A. Young (2011), Visible light scattering study at 470, 550, and 660 nm of components of mineral dust aerosol: Hematite and goethite, *J. Quant. Spect. Radiat. Trans., 112,* 1108-1118, doi:10.1016/j.jqsrt.2010.12.002

Ming, J., C. Xiao, H. Cachier, D. Qin, X. Qin, Zh. Li, and J. Pu (2009), Black carbon (BC) in the snow of glaciers in west China and its potential effects on albedos, *Atmospheric Research, 92*, 114-123.

Ming, J., C. Xiao, Z. Du, and X. Yang (2013), An overview of black carbon deposition in High Asia glaciers and its impacts on radiation balance, *Adv. Water Res., 55,* 80-87.

Mlawer, E.J., and S.A. Clough (1997), On the extension of rapid radiative transfer model to the shortwave region, *Proc. Sixth Amospheric Radiation Measurement (ARM) Science Team Meeting*, U.S. Department of Energy, CONF-9603149, 223–226.

Moosmüller, H., R. K. Chakrabarty, and W. P. Arnott (2009), Aerosol light absorption and its measurement: A review. *Journal of Quantitative Spectroscopy and Radiative Transfer, 110*(11), 844-878.

Mullen, P.C., and S.G. Warren (1988), Theory of the optical properties of lake ice. *J. Geophys. Res.*, 93, 8403-8414.

Müller, T., A. Schladitz, A. Massling, N. Kaaden, K. Kandler, and A. Wiedensohler (2009), Spectral absorption coefficients and imaginary parts of refractive indices of Saharan dust during SAMUM-1, *Tellus B, 61*, 79–95.

Müller, T., A. Schladitz, K. Kandler, and A. Wiedensohler (2011), Spectral particle absorption coefficients, single scattering albedos and imaginary parts of refractive indices from ground based in-situ measurements at Cape Verde Island during SAMUM-2, *Tellus B, 63*, 573-588.

Myhre, G, A. Grini, J.M. Haywood, F. Stordal, B. Chatenet, D. Tanré, J.K. Sundet, and I.S.A. Isaksen (2003), Modeling the radiative impact of mineral dust during the Saharan Dust Experiment (SHADE) campaign, *J. Geophys. Res., 10*, 8579, doi:10.1029/2002JD002566.

Namazi, M., K. von Salzen, and J. N. S. Cole (2015), Simulation of black carbon in snow and its climate impact in the Canadian Global Climate Model, *Atmos. Chem. Phys., 15*, 10887-10904, doi:10.5194/acp-15-10887-2015.

Neshyba, S.P., T.C. Grenfell, and S.G. Warren (2003), Representation of a nonspherical ice particle by a collection of independent spheres for scattering and absorption of radiation: II. Hexagonal columns and plates, *J. Geophys. Res, 108,* D15, 4448, doi:10.1029/2002JD003302.

Niwano, M., T. Aoki, K. Kuchiki, M. Hosaka, and Y. Kodama (2012), Snow metamorphism and albedo process (SMAP) model for climate studies: Model validation using

meteorological and snow impurity data measured at Sapporo, Japan, *J. Geophys. Res., 117,* F03008, doi:10.1029/2011JF002239.

Osborne, S.R., B.T. Johnson, J.M. Haywood, A.J. Baran, M.A.J. Harrison, and C.L. McConnell (2008), Physical and optical properties of mineral dust during the Dust and

Ottaviani, M., B. van Diedenhoven, and B. Cairns (2015), Photopolarimetric retrievals of snow properties, *The Cryosphere*, 9, 1933-1942, doi:10.5194/tc-9-1933-2015.

Otterman, J., and R.S. Fraser (1976), Earth-atmosphere system and surface reflectivities in arid regions from Landsat MSS data, *Remote Sens. Environ., 5***,** 247-266.

Painter, T. H., A.P. Barrett, C.C. Landry, J.C. Neff, M.P. Cassidy, C.R. Lawrence, K.E. McBride, and G.L. Farmer (2007), Impact of disturbed desert soils on duration of mountain snow cover, *Geophys. Res. Lett., 34*, L12502, doi:10.1029/2007GL030284.

Painter, T. H., S. M. Skiles, J. S. Deems, A. C. Bryant, and C. C. Landry (2012), Dust radiative forcing in snow of the Upper Colorado River Basin: 1. A 6 year record of energy balance, radiation, and dust concentrations, *Water Resour. Res.,* 48, W07521, doi:10.1029/2012WR011985.

Patterson, E. M., D. A. Gillette and B. H. Stockton (1977), Complex index of refraction between 300 and 700 nm for Saharan aerosols, *J. Geophys. Res.*, *82*, 3153-3160.

Petzold, A., K. Rasp, B. Weinzierl, M. Esselborn, T. Hamburger, A.D. Örnbrack, K. Kandler, L. Schütz, P. Knippertz, M. Fiebig, and A. Virkkula (2009), Saharan dust absorption and refractive index from aircraft-based observations during SAMUM 2006, *Tellus, 61B*, 118-130.

Qian, Y., T. J. Yasunari, S. J. Doherty, M. G. Flanner, W. K. Lau, J. Ming, H. Wang, M. Wang, S. G. Warren, and R. Zhang (2015), Light-absorbing particles in snow and ice: Measurement and modeling of climatic and hydrological impact, *Advances in Atmospheric Sciences 32,* no. 1: 64-91.

Qian, Y.,W. I. Gustafson Jr., L. R. Leung, and S. J. Ghan (2009), Effects of soot-induced snow albedo change on snowpack and hydrological cycle in western United States

based on Weather Research and Forecasting chemistry and regional climate simulations, *J. Geophys. Res., 114*, D03108, doi:10.1029/2008JD011039.

Räisänen, P., A. Kokhanovsky, G. Guyot, O. Jourdan, and T. Nousiainen (2015), Parameterization of single-scattering properties of snow. *The Cryosphere Discuss., 9,* 873-926, doi:10.5194/tcd-9-873-2015.

Reid, J.S., H. Halflidi, H. Jonsson, H.B. Maring, A. Smirnov, D.L. Savoie. S.S. Cliff, E.A. Reid, J.M. Livingston, M.M. Meier, O. Dubovik, and S.-C. Tsay (2003), Comparison of size and morphological measurements of coarse mode dust particles from Africa, *J. Geophys. Res., 108*, 8593, doi:10.1029/2002JD002485.

Reist, P.C. (1993), *Aerosol Science and Technology*. McGraw-Hill, New York.

Ricchiazzi, P., S. Yang, C. Gautier, and D. Sowle (1998), SBDART: A research and teaching software tool for plane-parallel radiative transfer in the Earth's atmosphere, *Bull. Am. Meteorol. Soc., 79*(10), 2101– 2114, doi:10.1175/1520-0477(1998)079<2101:SARATS>2.0.CO;2.

Schwartz, J.P., R.S. Gao, A.E. Perring, J.R. Spackman, and D.W. Fahey (2013), Black carbon aerosol size in snow, *Nature Scientific Reports, 3,* 1356. Doi:10.1038/srep01356.

Sherman, D.M., and T.D. Waite (1985), Electronic spectra of Fe^{3+} oxides and oxide hydroxides in the near IR to near UV, *American Mineralogist, 70,* 1262-1269.

Smith, E.A. (1986), The structure of the Arabian heat low, Part I: Surface energy budget, *Mon. Wea. Rev., 114***,** 1067-1083.

Sokolik, I., A. Andronova, and T.C. Johnson (1993), Complex refractive index of atmospheric dust aerosols, *Atmos. Environ., 27A*, 2495-2502.

Sokolik, I.N., and O.B. Toon (1999), Incorporation of mineralogical composition into models of the radiative properties of mineral aerosol from UV to IR wavelengths, *J. Geophys. Res., 104*, 9423-9444.

Solmon, F., M. Mallet, N. Elguindi, F. Giorgi, A. Zakey, and A. Konaré (2008), Dust aerosol impact on regional precipitation over western Africa, mechanisms and sensitivity to absorption properties, *Geophys. Res. Lett., 35,* doi:10.1029/2008GL035900.

Stamnes, K., S.-C. Tsay, W. Wiscombe, and K. Jayaweera (1988), Numerically stable algorithm for discrete-ordinate-method radiative transfer in multiple scattering and emitting layered media, *Appl. Opt., 27*(12), 2502– 2509.

Stephens, G. L., S.-C. Tsay, P. W. Stackhouse Jr., and P. J. Flatau (1990), The relevance of the microphysical and radiative properties of cirrus clouds to climatic feedback. *J. Atmos. Sci.*, 47, 1742–1753.

Sturm, M., C. Derksen, G. Liston, A. Silis, D. Solie, J. Holmgren, and H. Huntington (2008), *A Reconnaissance Snow Survey Across Northwest Territories and Nunavut, Canada, April 2007* (ERDC/CRREL-TR-08-3). Cold Regions Research and Engineering Laboratory (CRREL), Hanover, NH.

Sun, W.B., Q. Fu, and Z.Z Chen (1999), FDTD solution of light scattering by dielectric using PML ABC. Appl. Opt., 38, 3141-3151.

Tsay, S.C. and K. Jayaweera (1984), Physical characteristics of Arctic stratus clouds, *J. Climate Appl. Meteorol., 23*(4), 584–596.

van Diedenhoven, B., A.S. Ackerman, B. Cairns, and A.M. Fridlind (2014), A flexible parameterization for shortwave optical properties of ice crystals. *Journal of the Atmospheric Sciences*, *71*(5), pp.1763-1782.

van Diedenhoven, B., B. Cairns, I.V. Geogdzhayev, A.M. Fridlind, A.S. Ackerman, P. Yang, and B.A. Baum (2012), Remote sensing of ice crystal asymmetry parameter using multi-directional polarization measurements. Part I: Methodology and evaluation with simulated measurements. *Atmos. Meas. Tech.*, 5, 2361-2374, doi:10.5194/amt-5-2361-2012.

Wagner, R., T. Ajtai, K. Kandler, K. Lieke, C. Linke, T. Müller, M. Schnaiter, and M. Vragel (2012), Complex refractive indices of Saharan dust samples at visible and near UV wavelengths: a laboratory study, *Atmos. Chem. Phys., 12,* 2491-2512.

Wang, X., S.J. Doherty, and J. Huang (2013), Black carbon and other light-absorbing impurities in snow across northern China, *J. Geophys. Res., 118,* 1471-1492, doi:10.1029/2012JD018291.

Warren, S. G., W. J. Wiscombe (1980), A Model for the Spectral Albedo of Snow. II: Snow Containing Atmospheric Aerosols. *J. Atmos. Sci., 37*, 2734–2745.

Warren, S.G, (1982), Optical properties of snow. *Rev. Geophys. Space Phys.*, 20, 67-89.

Warren, S.G. (1984), Optical constants of ice from the ultraviolet to the microwave, *Applied Optics*, *23*, 1206-1225.

Warren, S.G. (2013), Can black carbon in snow be detected by remote sensing?, *J. Geophys. Res.,118*, 779-786, doi:10.1029/2012JD018476.

Warren, S.G., and A.D. Clarke (1990), Soot in the atmosphere and snow surface of Antarctica, *J. Geophys. Res., 95,* 1811-1816.

Warren, S.G., and R.E. Brandt (2008), Optical constants of ice from the ultraviolet to the microwave: A revised compilation. *Journal of Geophysical Research, 113*, D14220, doi:10.1029/2007JD009744.

Warren, S.G., and W.J. Wiscombe (1985), Dirty snow after nuclear war, *Nature, 313*, 467-470.

Warren, S.G., R.E. Brandt, and T.C. Grenfell (2006), Visible and near-ultraviolet absorption spectrum of ice from transmission of solar radiation into snow. *Appl. Opt., 45*, 5320-5334.

Wielicki, B.A., B.R. Barkstrom, E.F. Harrison, R.B. Lee III, G. L. Smith, and J.E. Cooper, (1996), Clouds and the Earth's Radiant Energy System (CERES): An earth observing system experiment, *Bulletin of the American Meteorological Society*, *77*(5), 853-868.

Wiscombe, W.J. (1980), Improved Mie scattering algorithms, *Appl. Opt., 19,* 1505–1509.

Wiscombe, W.J., and S.G. Warren (1980), A model for the spectral albedo of snow, I: Pure snow, *J. Atmos. Sci.*, *37*, 2712-2733.

Xie, Y., P. Yang, B. C. Gao, G. W. Kattawar, & M. I. Mishchenko (2006), Effect of ice crystal shape and effective size on snow bidirectional reflectance. *Journal of Quantitative Spectroscopy and Radiative Transfer*, *100*(1), 457-469. doi:10.1016/j.jqsrt.2005.11.056

Yang, P, and K. N. Liou (1996), Finite-difference time domain method for light scattering by small ice crystals in three-dimensional space. *JOSA A* 13, no. 10:2072-2085.

Yang, P. and Q. Fu (2009), Dependence of ice crystal optical properties on particle aspect ratio. *Journal of Quantitative Spectroscopy and Radiative Transfer, 110*(14), pp.1604-1614.

Yang, P., and K.N. Liou (1995), Light scattering by hexagonal ice crystals: Comparison of finite-difference time domain and geometric optics models. *J. Opt. Soc. Am. A.*, 12, 162-176.

Yang, P., K. N. Liou, K. Wyser, and D. Mitchell (2000), Parameterization of the scattering and absorption properties of individual ice crystals, *J. Geophys. Res., 105*, 4699-4718.

Yasunari, T.J., K.-M. Lau, S.P.P. Mahanama, P.R. Colarco, A.M. da Silva, T. Aoki, K. Aoki, N. Murao, S. Yamagata, and Y. Kodama (2014), Goddard Snow Impurity Module (GOSWIM) for the NASA GEOS-5 Earth System Model: Preliminary comparisons with observations in Sapporo, Japan, *SOLA, 10*, 50−56, doi:10.2151/sola.2014-011.

Yasunari, T.J., R.D. Koster, K.-M. Lau, T. Aoki, Y.C. Sud, T. Yamazaki, H. Motoyoshi, and Y. Kodama (2011), Influence of dust and black carbon on the snow albedo in the NASA Goddard Earth Observing System version 5 land surface model, *J. Geophys. Res., 116,* D02210, doi:10.1029/2010JD014861.

Ye, H., R. Zhang, J. Shi, J. Huang, S.G. Warren, and Q. Fu (2012), Black carbon in seasonal snow across northern Xinjiang in northwestern China, *Environ. Res. Lett.*, 7, doi:10.1088/1748-9326/7/4/044002.

Zatko, M.C., T.C. Grenfell, B. Alexander, S.J. Doherty, J.L. Thomas and X. Yang (2013), The influence of snow grain size and impurities on the vertical profiles of actinic flux and associated NOx emissions on the Antarctic and Greenland ice sheets, *Atmos. Chem. Phys.* 13, 3547-3567, doi:10.5194/acp-13-3547-2013.

Zender, C.S., H. Bian, and D. Newman (2003), Mineral dust entrainment and deposition (DEAD) model: Description and 1990s dust climatology, *J. Geophys. Res., 108,* 4416, doi:10.1029/2002JD002775.

Zhang, R., H.Wang, D. A. Hegg, Y. Qian, S. J. Doherty, C. Dang, P.-L. Ma, P. J. Rasch, and Q. Fu (2015), Quantifying sources of black carbon in Western North America using observationally based analysis and an emission tagging technique in the Community

Atmosphere Model, *Atmos. Chem. Phys., 15*, 12805-12822, doi:10.5194/acp-15-12805-2015.

Zhao, C., X. Liu, R. Leung, and S. Hagos (2011), Radiative impact of mineral dust on monsoon precipitation variability over West Africa, *Atmos. Chem. Phys., 11,* 1879-1893.

Zhao, C., Z. Hu, Y. Qian, L. Ruby Leung, J. Huang, M. Huang, J. Jin, M. G. Flanner, R. Zhang, H. Wang, H. Yan, Z. Lu, and D. G. Streets (2014), Simulating black carbon and dust and their radiative forcing in seasonal snow: a case study over North China with field campaign measurements, *Atmos. Chem. Phys., 14*, 11475-11491, doi:10.5194/acp-14-11475-2014.

Appendix A-1

Combining single-scattering quantities for ice, dust, and black carbon

Snow consists of a mixture of ice, dust, BC, and air, with size distributions of the particulate components $n_i(r_i)$, $n_j(r_j)$, and $n_k(r_k)$ respectively; units of n are particles per m^3. A single ice particle (assumed spherical) has volume $V_i = \frac{4}{3}\pi r_i^3$ and cross-section area $A_i = \pi r_i^2$; similarly for a dust particle with volume V_j and area A_j, and a BC particle with volume V_k and area A_k. If the n values are accurately scaled using scale factors f_i as defined below, then the density of snow (units kg m^{-3}) is

$$\rho_{snow} = f_{ice}\rho_{ice}\sum_i V_i n_i + f_{dust}\rho_{dust}\sum_j V_j n_j + f_{BC}\rho_{BC}\sum_k V_k n_k \,, \tag{A1}$$

where r_{ice} = 917 kg m^{-3}, r_{dust} = 2500 kg m^{-3}, and r_{BC} = 1800 kg m^{-3}.

In practice each of these three size distributions would usually have been obtained separately with arbitrary normalization, so they must be rescaled for each new set of mass fractions (C_{dust} and C_{BC}), using the scaling factors f_{ice}, f_{dust}, and f_{BC}, as given below, assuming that r_{snow} is specified.

Abbreviating Q_{ext} as simply Q, the extinction efficiencies are Q_i, Q_j, and Q_k, for ice, dust, and BC respectively. For ice the extinction cross-section area per unit volume (units m^2/m^3) is

$$\sigma_{ext}^{ice} = f_{ice}\sum_i Q_i A_i n_i \,, \tag{A2}$$

and the scattering cross-section area per unit volume is

$$\sigma_{sca}^{ice} = f_{ice}\sum_i Q_i A_i \varpi_i n_i \,. \tag{A3}$$

The single-scattering albedo for the size distribution of snow grains is

$$\varpi_{ice} = \sigma_{sca}^{ice} / \sigma_{ext}^{ice}. \tag{A4}$$

The asymmetry parameter for the size distribution is

$$g_{ice} = \frac{f_{ice}\sum_i g_i Q_i A_i \varpi_i n_i}{f_{ice}\sum_i Q_i A_i \varpi_i n_i} = \frac{f_{ice}\sum_i g_i Q_i A_i \varpi_i n_i}{\sigma_{sca}^{ice}}. \tag{A5}$$

Similar relations give the corresponding quantities for dust and BC:

$\sigma_{sca}^{dust}, \sigma_{ext}^{dust}, g_{dust}, \sigma_{sca}^{BC}, \sigma_{ext}^{BC}, g_{BC}$.

The mass-absorption cross-section, for example for dust (units m^2/kg), is

$$B_a = \frac{\sigma_{ext}^{dust} - \sigma_{sca}^{dust}}{f_{ice}\rho_{dust}\sum_j V_j n_j}. \tag{A6}$$

If Q and v are the same for all the dust particles (as they would be for a monodispersion), Eq. A6 reduces to

$$B_a = \frac{3Q(1-\varpi)}{4 r_{eff}\rho_{dust}}, \tag{A7}$$

where the "effective radius" [*Hansen and Travis*, 1974] is

$$r_{eff} = \frac{\sum_j r_j^3 n_j}{\sum_j r_j^2 n_j}. \tag{A8}$$

Eq. A7 is the same as Eq. 6 in the main paper.

For a medium consisting of a mixture of air with just one particulate component (ice, dust, or BC), equations A2-A6 are appropriate. For a multicomponent mixture the following equations apply.

Define the mass fractions of ice, dust, and BC as C_{ice}, C_{dust}, C_{BC}. Ignoring the negligible mass of air, the mass fractions of the particles add to 1:

$$C_{ice} + C_{dust} + C_{BC} = 1. \tag{A9}$$

The scaling factors for the ice, dust, and BC size distributions, needed below, are (from Eq. A1):

$$f_{ice} = \frac{C_{ice}\rho_{snow}}{\rho_{ice}\sum_i V_i n_i}. \tag{A10}$$

$$f_{dust} = \frac{C_{dust}\rho_{snow}}{\rho_{dust}\sum_j V_j n_j}; \tag{A11}$$

$$f_{BC} = \frac{C_{BC}\rho_{snow}}{\rho_{BC}\sum_k V_k n_k}; \tag{A12}$$

The extinction cross-section for the mixture is

$$\sigma_{ext} = f_{dust}\sigma_{ext}^{dust} + f_{BC}\sigma_{ext}^{BC} + f_{ice}\sigma_{ext}^{ice}. \tag{A13}$$

The optical depth of a layer of thickness Dz is

$$\tau = \sigma_{ext}\Delta z. \tag{A14}$$

The scattering cross-section is

$$\sigma_{sca} = f_{dust}\sigma_{sca}^{dust} + f_{BC}\sigma_{sca}^{BC} + f_{ice}\sigma_{sca}^{ice}. \tag{A15}$$

The single-scattering albedo is

$$\varpi = \sigma_{sca} / \sigma_{ext}. \tag{A16}$$

The asymmetry parameter is

$$g = [g_{ice}f_{ice}\sigma_{sca}^{ice} + g_{dust}f_{dust}\sigma_{sca}^{dust} + g_{BC}f_{BC}\sigma_{sca}^{BC}] / \sigma_{sca}. \tag{A17}$$

If single-scattering quantities for pure snow have been precomputed, then the ice size distribution $n_i(r_i)$ is not needed; one can instead use C_i together with previously obtained values of v_i, g_i, and Q_{ext}^{ice}. So in this case, from Q_{ext}^{ice} one would compute σ_{ext}^{ice} as

$$\sigma_{ext}^{ice} = \frac{3Q_{ext}^{ice}\rho_{snow}}{4r_{eff}\rho_{ice}} \text{ (units m}^{-1}\text{).} \quad \text{(A18)}$$

In a "pure" snowpack (no dust or BC) we would have

$$\sum_i V_i n_i = \frac{\rho_{snow}}{\rho_{ice}} \text{ (from Eq. A1)}$$

and

$$\sigma_{ext} = f_{ice}\sigma_{ext}^{ice} \text{ (from Eq. A13).}$$

Then (A10) can be replaced by $f_{ice} = C_{ice}$. Alternatively, one can replace the third term in (A13), which is $f_{ice}\sigma_{ext}^{ice}$, by $\frac{3Q_{ext}^{ice}\rho_{snow}C_{ice}}{4r_{eff}\rho_{ice}}$. Note that the product $\rho_{snow}C_{ice}$ is the density the snowpack would have if all the dust and BC were removed from it.

Appendix A-2

Supplementary materials for Chapter 2

Figure A1. Single-scattering quantities for pure snow: (a) Extinction efficiency Q_{ext}; (b) single-scattering coalbedo 1- v ; (c) asymmetry parameter g;

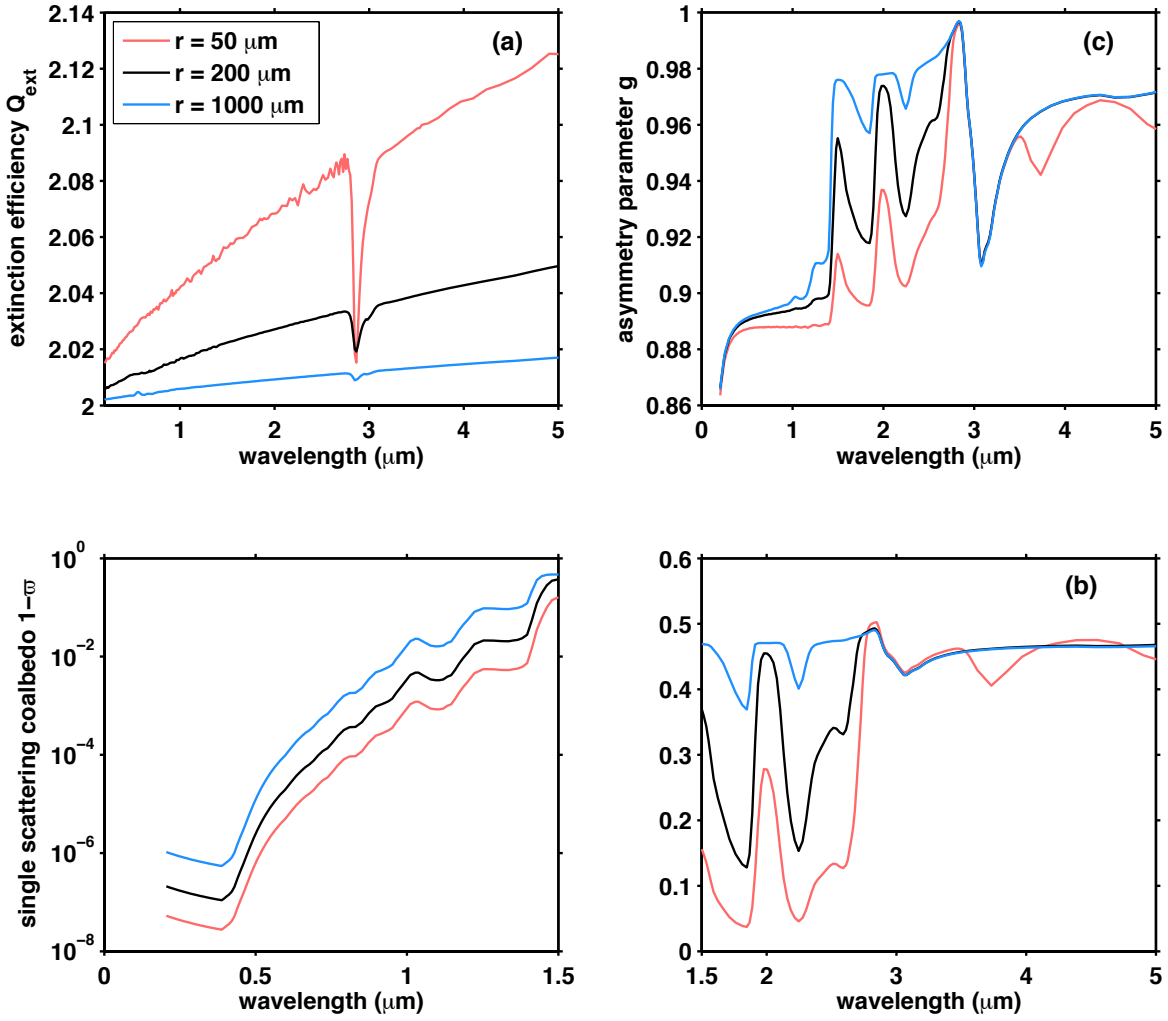

Figure A2. Error in broadband albedo reduction induced by using BC-snow albedo reduction parameterization suggested in Section 5.2. The dashed curves, solid curves, and asterisk show errors of albedo reduction in different ranges of BC mass fraction listed in Table 1. The colors code different snow grain radius ranges from 5 – 2500 μm as indicated in the right bottom corner.

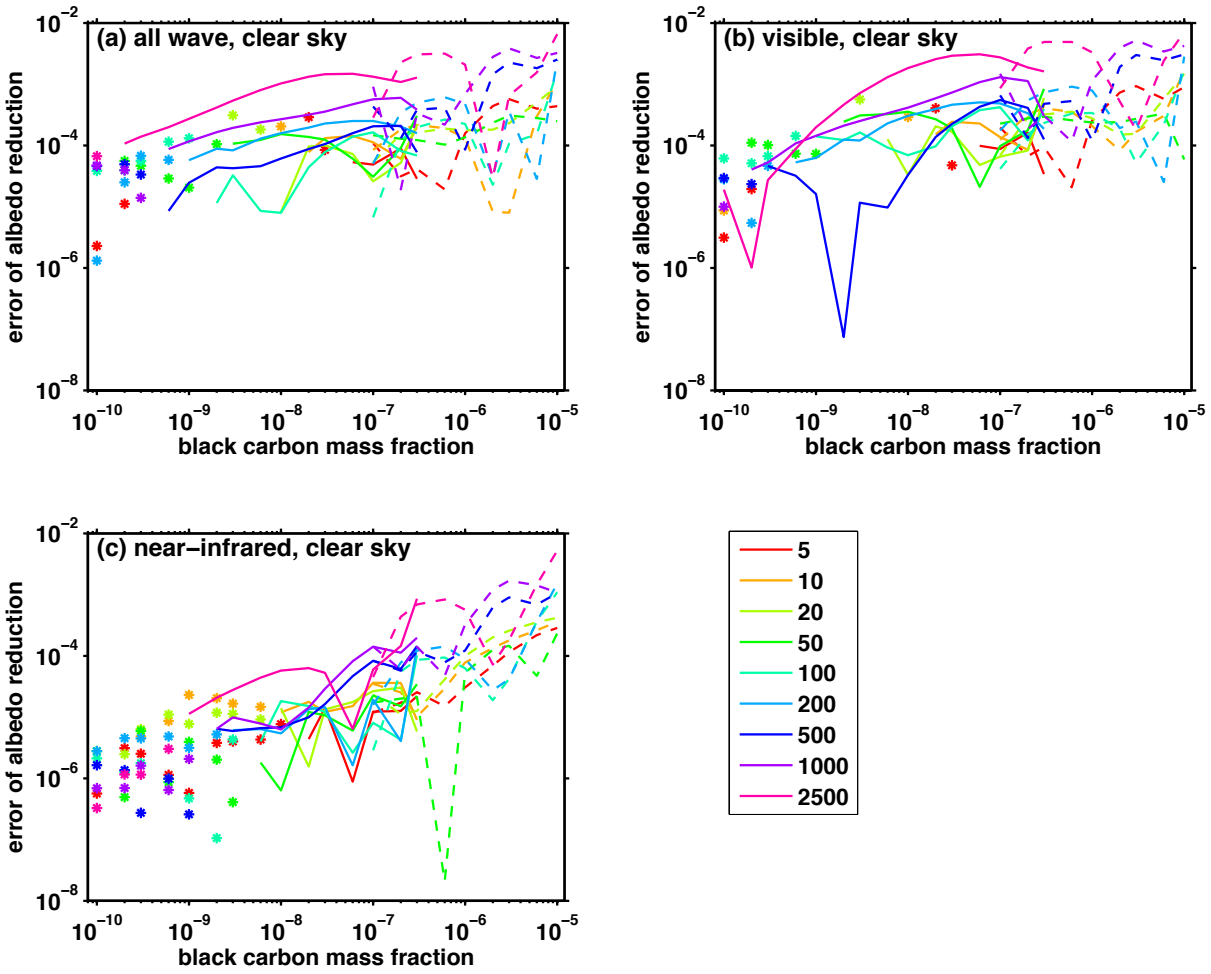

Figure A3. Evaluation of albedo reduction calculated using BC equivalent factor f (*snow contain only dust*).
Top panels: the solid curves are broadband (all wave and visible) albedo reduction calculated using DISORT for different snow grain radius and dust mass fraction; the dots are broadband albedo reduction calculated using parameterization of BC-snow albedo reduction suggested in Section 5.2 and corresponding BC equivalent mass fraction for given dust mass fraction. Bottom panel: absolute error of broadband albedo reduction induced by using parameterization and BC equivalent mass fraction.

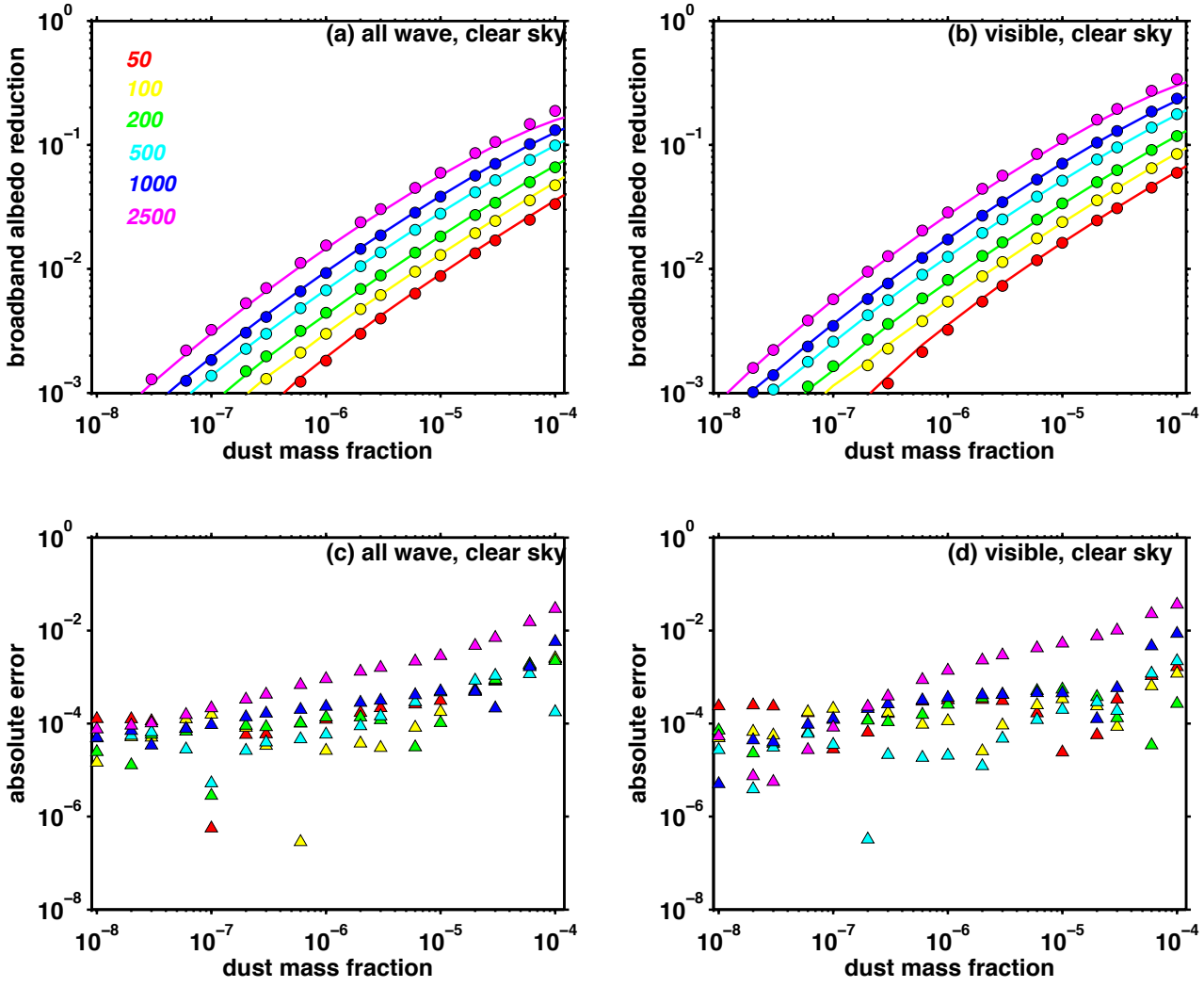

Figure A4. Evaluation of albedo reduction calculated using BC equivalent factor f (*snow contain both BC and dust, allwave band, snow grain radius r = 100 μm and 1000 μm).*
Top panels: the solid curves are allwave-broadband albedo reduction calculated using DISORT for different snow grain radius and mixture of BC and dust mass fractions; the dots are broadband albedo reduction calculated using parameterization of BC albedo reduction suggested in Section 5.2 and corresponding BC equivalent mass fraction for given amount of dust and BC mixture. Bottom panel: absolute error of broadband albedo reduction calculated using parameterization and BC equivalent mass fraction.

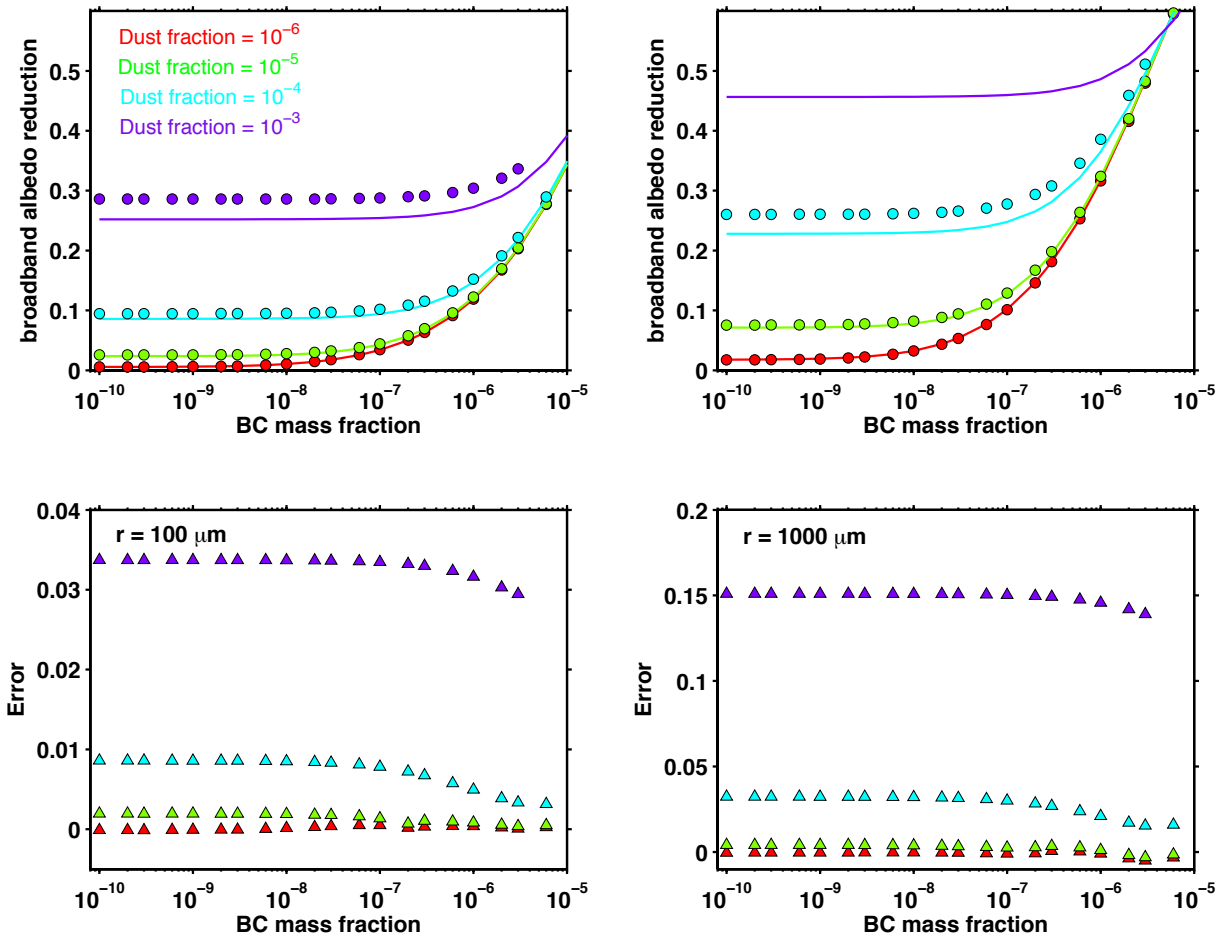

Figure A5. Evaluation of albedo reduction calculated using BC equivalent factor f (*snow contain both BC and dust, visible, snow grain radius r = 100 μm and 1000 μm).*
Top panels: the solid curves are visible-broadband albedo reduction calculated using DISORT for different snow grain radius and mixture of BC and dust mass fractions; the dots are broadband albedo reduction calculated using parameterization of BC albedo reduction suggested in Section 5.2 and corresponding BC equivalent mass fraction for given amount of dust and BC mixture. Bottom panel: absolute error of broadband albedo reduction calculated using parameterization and BC equivalent mass fraction.

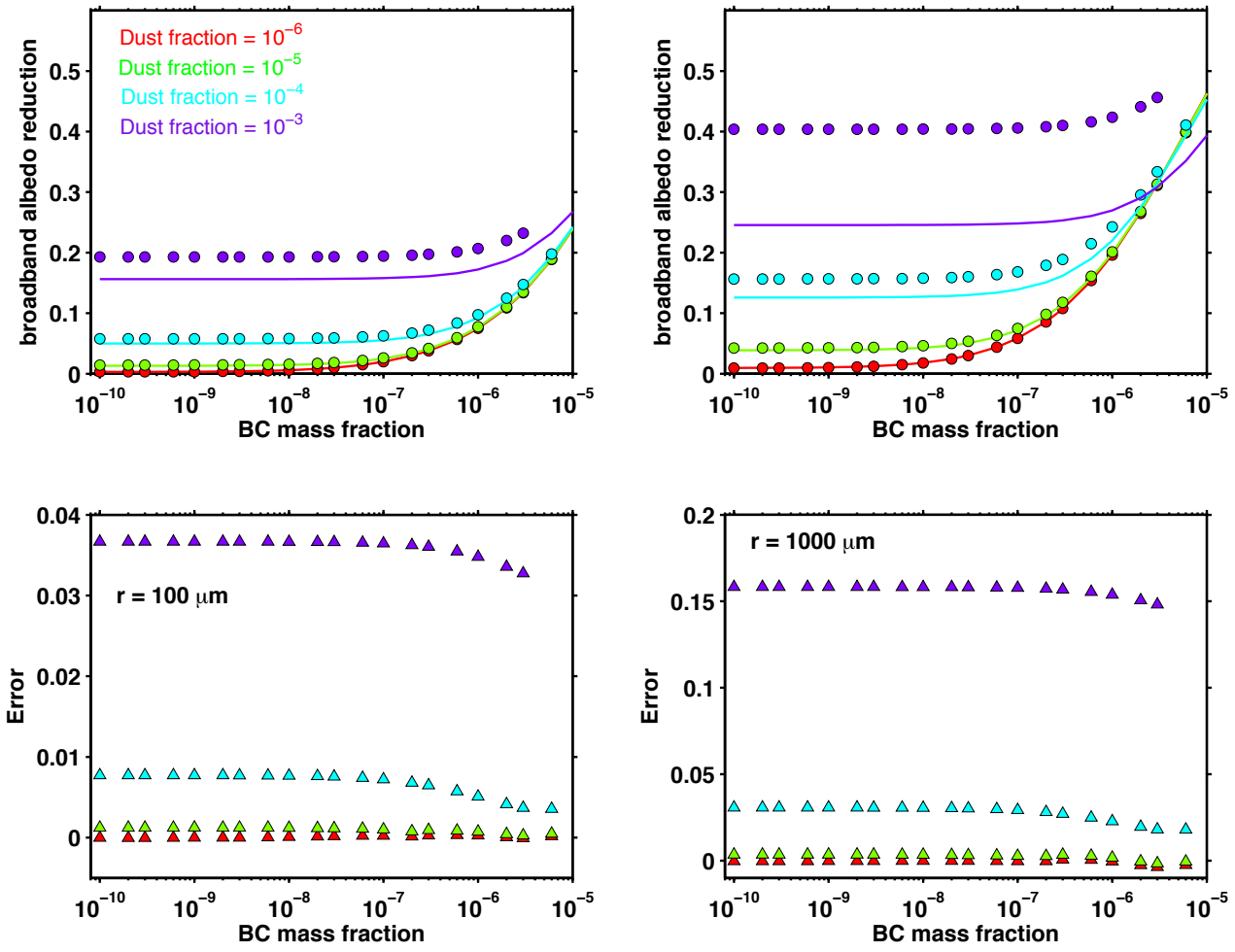

Table A1. Coefficients for Parameterization for RRTM-band albedo reduction due to BC.

Range 1 ($10^{-7} < C < 10^{-5}$)							
Clear sky (sza = 49.5°)				Overcast sky			
	$p_{row,1}$	$p_{row,2}$	$p_{row,3}$		$p_{row,1}$	$p_{row,2}$	$p_{row,3}$
RRTM2	0.0120	-0.0238	0.0014	RRTM2	0.0120	-0.0238	0.0014
	-0.0311	0.0052	-0.0671		-0.0311	0.0052	-0.0671
	-0.0296	-0.0810	0.4896		-0.0296	-0.0810	0.4896
	-0.0397	0.4641	-0.8174		-0.0397	0.4641	-0.8175
RRTM3	0.0119	-0.0252	0.0038	RRTM3	0.0119	-0.0251	0.0038
	-0.0329	0.0095	-0.0705		-0.0328	0.0095	-0.0704
	-0.0272	-0.0805	0.4940		-0.0272	-0.0807	0.4941
	-0.0384	0.4662	-0.8331		-0.0384	0.4662	-0.8329
RRTM4	0.0059	-0.0184	0.0022	RRTM4	0.0061	-0.0187	0.0024
	-0.0190	-0.0159	-0.0523		-0.0192	-0.0155	-0.0525
	-0.0360	-0.0466	0.4759		-0.0361	-0.0467	0.4759
	-0.0448	0.4953	-0.9011		-0.0445	0.4944	-0.8997
RRTM5	0.0002	-0.0113	-0.0034	RRTM5	0.0002	-0.0113	-0.0033
	-0.0157	-0.0205	-0.0529		-0.0157	-0.0205	-0.0528
	-0.0306	-0.0398	0.4775		-0.0307	-0.0399	0.4775
	-0.0877	0.6238	-1.0861		-0.0873	0.6224	-1.0842
RRTM6	-0.0024	-0.0102	-0.0094	RRTM6	-0.0023	-0.0102	-0.0092
	-0.0173	-0.0172	-0.0796		-0.0172	-0.0170	-0.0782
	-0.0297	-0.0310	0.4506		-0.0298	-0.0310	0.4530
	-0.1049	0.8327	-1.5522		-0.1072	0.8279	-1.5261

Range 2 ($C_{low} < C < 3\times10^{-7}$)							
Clear sky (sza = 49.5°)				Overcast sky			
	$p_{row,1}$	$p_{row,2}$	$p_{row,3}$		$p_{row,1}$	$p_{row,2}$	$p_{row,3}$
RRTM2	0.0061	-0.0254	0.0021	RRTM2	0.0063	-0.0254	0.0021
	-0.0416	0.0105	-0.0643		-0.0418	0.0104	-0.0643
	0.0320	-0.0526	0.4884		0.0319	-0.0526	0.4884
	-0.0329	0.4597	-0.8196		-0.0328	0.4598	-0.8197
RRTM3	0.0042	-0.0291	0.0039	RRTM3	0.0040	-0.0291	0.0038
	-0.0418	0.0146	-0.0680		-0.0416	0.0146	-0.0680
	0.0335	-0.0523	0.4931		0.0337	-0.0523	0.4932
	-0.0324	0.4618	-0.8352		-0.0326	0.4617	-0.8350
RRTM4	0.0267	0.0011	0.0046	RRTM4	0.0280	0.0017	0.0049
	-0.0387	-0.0244	-0.0508		-0.0406	-0.0254	-0.0512
	-0.0079	-0.0323	0.4756		-0.0081	-0.0326	0.4754
	-0.0564	0.4702	-0.9071		-0.0558	0.4692	-0.9059
RRTM5	0.0157	0.0031	-0.0020	RRTM5	0.0154	0.0021	-0.0022
	-0.0228	-0.0234	-0.0517		-0.0235	-0.0242	-0.0518
	0.0004	-0.0088	0.4824		0.0011	-0.0074	0.4828
	-0.0836	0.6439	-1.0814		-0.0834	0.6426	-1.0793
RRTM6	0.0094	0.0046	-0.0068	RRTM6	0.0096	0.0044	-0.0066
	-0.0054	-0.0099	-0.0787		-0.0054	-0.0094	-0.0772
	-0.0148	-0.0213	0.4514		-0.0144	-0.0201	0.4542
	-0.0209	0.9062	-1.5436		-0.0214	0.9036	-1.5171

Range 3 ($0 < C < C_{low}$)									
Clear sky (sza = 49.5°)					Overcast sky				
	j_1	j_2	j_3	t		j_1	j_2	j_3	t
RRTM2	0.1727	-1.1009	-8.2299	0.01	RRTM2	0.1727	-1.1009	-8.2299	0.01
RRTM3	0.1898	-1.1046	-8.2039	0.01	RRTM3	-0.0326	0.4617	-0.8350	0.01
RRTM4	0.1839	-0.7407	-9.1476	0.001	RRTM4	0.1839	-0.7407	-9.1476	0.001
RRTM5	0.0670	-0.5309	-8.2800	0.001	RRTM5	0.0670	-0.5309	-8.2800	0.001
RRTM6	0.0732	-0.4437	-8.5481	0.0001	RRTM6	0.0732	-0.4437	-8.5481	0.0001

Appendix B

Supplementary materials for Chapter 3

Figure B1. Error in albedo if snow albedo were calculated using mean scaling factor for grain radius 200 μm (numbers given in parenthesis).

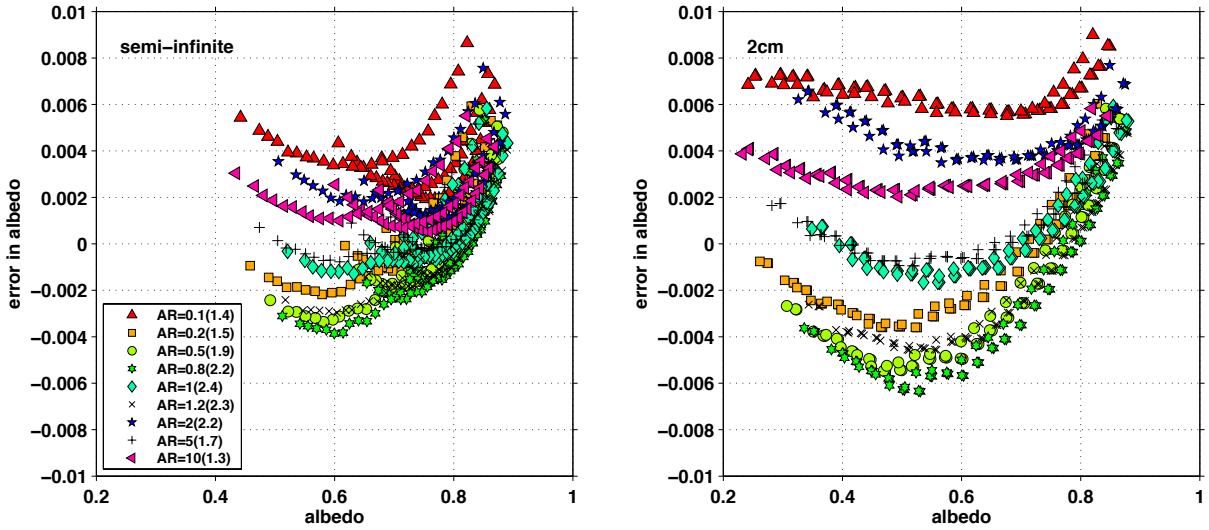

Figure B2. Error in albedo if snow albedo were calculated using the scaling factor appropriate for each individual snow radius and aspect ratio, shown as black curve in supplementary figure 3.3.

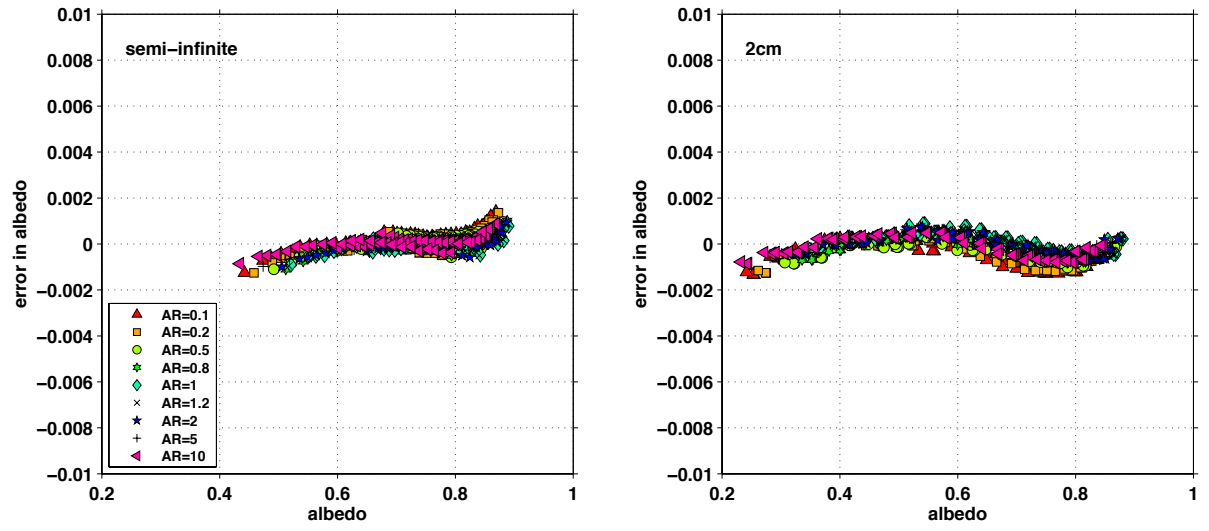

Figure B3. Scaling factor as a function of snow grain radius, for 9 aspect ratios. Each marker shows the mean scaling factor of 6 cases (varying snow depth and BC content, as described in the text). The black curves are the scaling factor calculated using the parameterization (S1).

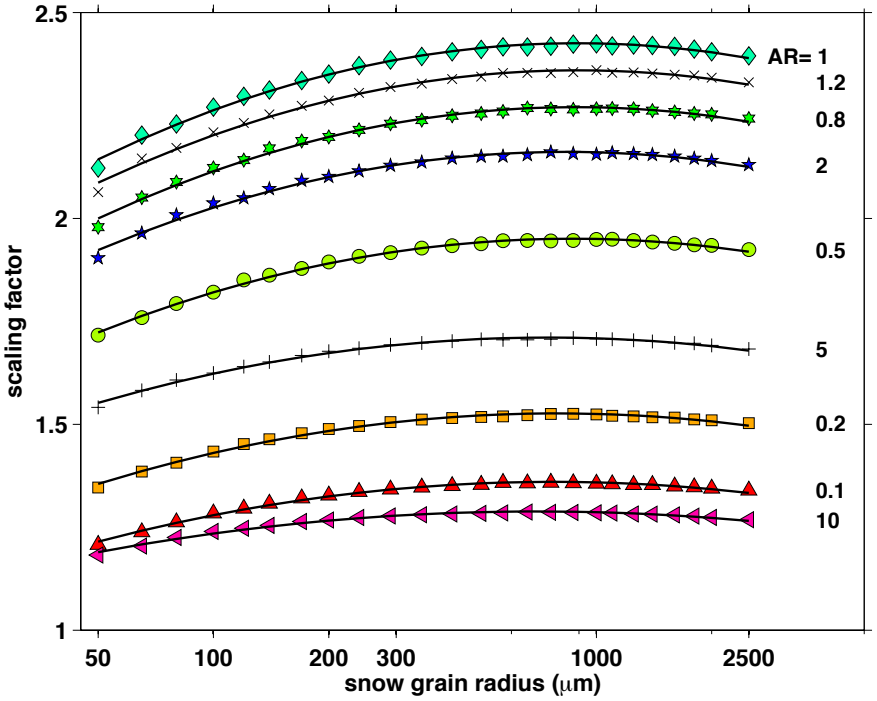

Table B1. Scaling factor f is parameterized as a function of snow grain radius and aspect ratio:

$$r_n \equiv log_{10}(r/100)$$

$$f = c_1 r_n^2 + c_2 r_n + c_3$$

The coefficients c are given in the following table:

Aspect Ratio (AR)	c_1	c_2	c_3
0.1	-0.10283	0.18238	1.2793
0.2	-0.11924	0.21407	1.4303
0.5	-0.1486	0.27832	1.8203
0.8	-0.17369	0.32885	2.1145
1	-0.18018	0.34246	2.2627
1.2	-0.17396	0.33114	2.202
2	-0.15977	0.29411	2.0262
5	-0.11506	0.20097	1.6229
10	-0.075293	0.1271	1.2346

VITA

Cheng Dang was born in Gansu Province of China and moved to Lanzhou City when she was 9 years old. In year 2007, she attended Lanzhou University, and obtained her Bachelor's Degree in Atmospheric Sciences four years later. She started graduate school at the University of Washington in the Department of Atmospheric Sciences in September 2011. In her second year at graduate school (year 2014), Cheng spent two months to travel across 13 American states and 3 Canadian Provinces to collect snow samples for the analysis of light-absorbing particles in snow. Since then, she has done both laboratory work and modeling work regarding light-absorbing particles in snow and the impact of these impurities and snow grain shape on snow albedo. Besides her interests in snow and climate, she also earned a Master's Degree from the Department of Applied Mathematics at the University of Washington at the end of year 2016. Four months later, in March of year 2017, Cheng finished her Ph.D. from the Department of Atmospheric Sciences at the University of Washington. After living in Seattle for more than five years, Cheng finds cloudy days and rainy days surprisingly pleasant.